Evolving Ice-Ocean Dynamics of the Western Arctic

Sarah R. Dewey

A dissertation
submitted in partial fulfillment of the
requirements for the degree of

Doctor of Philosophy

University of Washington
2019

Reading Committee:
James H. Morison, Chair
Susan L. Hautala
Ronald Kwok

Program Authorized to Offer Degree:
Oceanography

University of Washington

Abstract

Evolving Ice-Ocean Dynamics of the Western Arctic

Sarah R. Dewey

Chair of the Supervisory Committee:
James H. Morison
Oceanography

This dissertation examines the western Arctic Ocean and how its freshwater content and dynamics have evolved, particularly in the Beaufort Gyre circulation system north of Alaska. The recent growth of the Beaufort Sea Seasonal Ice Zone and its large freshwater content relative to the rest of the Arctic Ocean make it an ideal laboratory to understand the transformation of the air-ice-ocean physical system under a changing climate. We consider this system in part through the lens of its freshwater, bringing together in-situ and satellite observations and models to describe changes in mixed-layer salinity, ocean velocity, and surface stress.

The first part of this manuscript looks at the effect of large-scale sea ice retreat on local ocean mixed-layer freshwater content, and the second part examines changes in ocean and ice circulation speeds—and with them, resulting surface stresses—over time. These changes affect ocean freshwater content and gyre equilibration, both of which are observed to have stabilized in the last decade after a period of spin-up. The third part of this dissertation examines how ice-ocean stress coefficients behave at daily to monthly timescales, and how they too may have changed in recent decades. Together, this work provides a three-dimensional, updated description of how the Beaufort Sea surface physical system operates and transports freshwater, especially under recently diminished ice cover.

Table of Contents

List of Figures

List of Tables

Acknowledgments

In many ways the true architect of this work is Jamie Morison, who has been a source of guidance and strength for the past seven years—patient and kind while I flailed, proud and excited to celebrate each small success, and always an inspiration for what following a lifelong passion looks like. He is a giant in this field, and has had a similarly large impact on my life through his thoughtful mentoring and infectious enthusiasm.

In addition to Jamie, I owe a great debt to the members of my supervisory committee: Susan Hautala, Mark Warner, CC Bitz, and Ron Kwok. They have provided insight and feedback every step of the way, and have had a large hand in shaping this work. The Polar Science Center community members, especially the SIZRS participants, have shown me what a wonderful adventure field science can be. Roger Andersen: Thank you for teaching me and trusting me, and manning the data recording table during all those times I wanted to look out the window at the sea ice. To Mary-Louise Timmermans, you continue to be a source of support and warmth, and were the first to show me what a great mentor looks like.

I am also grateful to Cecilia Peralta-Ferriz, Melinda Webster, Hayley Dosser, Andrew Shao, Leah Johnson, and Katherine Heal for leading the way as graduate students, postdocs, PIs, confidantes, and friends. Special thanks to John Guthrie, for your kindness, sense of fun, and for ruining all future shared workspaces for me. I mean this as the deepest compliment.

To the men and women of Air Station Kodiak: Thank you for putting yourselves on the line as search and rescue personnel, and for putting up with our scientific intrusions. Partnering with you has been an incredible privilege, and our collaboration has taught me as much as the data it yields.

This work has had a number of critical financial backers, including the Office of Naval Research and NASA. I owe thanks to the Barton Family for sponsoring an ARCS Fellowship that provided me additional support during my first three years of study, and to the McDuff Family for endowing the Mary Landsteiner Scholar Award, in the spirit of which I strive to conduct myself as a researcher and community member.

I thank my School of Oceanography classmates, especially Earle Wilson and Anna McLaskey, who have daily demonstrated that the best and healthiest scientific community is imbued with the deepest humanity and caring. I am also grateful to the Complex for more than a decade of friendship and daily support.

Lastly, I thank my family. As perplexing as parts of this PhD journey might have been to them, my grandparents, aunts, uncles, in-laws, siblings, and most especially my parents were unquestioningly supportive. Thank you for teaching me to love learning and for encouraging me since day one. My husband, Liwei, has demonstrated the deepest depths of patience, integrity, affection, and enthusiasm. I love you, and I look forward to continuing to grow together.

-

Dedication

For Marty, a most extraordinary farm boy from Nebraska

Chapter 1: Introduction

In this dissertation, we use the Beaufort Sea as the setting for our investigation of the air-ice-ocean physical system under a changing climate. We consider this system in part from the dynamical perspective of freshwater, bringing together in-situ and satellite observations and models to describe changes in ocean mixed-layer salinity, velocity, and surface stress.

1.1 Background

The Arctic often serves as an indicator for broader global change. Its atmosphere and ocean have warmed in recent years relative to climatological averages, and its sea ice areal extent has been on the decline since the beginning of the satellite record. Its oceanic and atmospheric temperature increases may be amplified relative to those in lower latitudes; because Arctic Ocean water export affects global ocean circulation, these changes create feedbacks. Therefore, understanding the movement, temperature, and salinity of Arctic Ocean water is key to understanding climate change at regional and global levels.

One of the parameters crucial to this change is freshwater, or water low in salinity compared to a regional average reference value. Because of the low temperature of the Arctic Ocean, this freshwater controls the density and stratification of the water column. The ocean can freshen with added river discharge, precipitation, ice melt, or the advection of less saline water parcels from elsewhere. In the last few decades, freshwater content (FWC) has redistributed within the Arctic Ocean, increasing in the Beaufort Gyre circulation system north of Alaska before stabilizing since 2008 (Giles et al., 2012; Morison et al., 2012; Rabe et al., 2011; McPhee et al, 2009; Proshutinsky et al., 2009; Zhang et al., 2016a).

Concurrent with and perhaps contributing to this change has been an increase in seasonality of sea ice areal extent (Strong & Rigor, 2013; Peng and Meier, 2018) and an overall decline in sea ice persistence year to year (Comiso et al., 2007; Maslanik et al, 2011). An area of some of the largest seasonal sea ice decline, the Beaufort Gyre boasts the highest stored freshwater content in the Arctic Ocean (Serreze et al., 2006; Carmack et al., 2008; Kwok & Morison, 2011). Locally, this freshwater influences stratification and ice formation; were it to exit the Arctic Ocean, its effects would be farther-reaching, potentially disrupting the ocean's meridional overturning circulation and global climate (Proshutinsky and Johnson, 1997; Aagaard and Carmack, 1989; Proshutinsky et al., 2002; Jahn & Holland, 2013; Koenigk et al., 2007; Sévellec et al., 2017).

These physical changes motivate study of the Arctic Ocean by multiple stakeholders. Worldwide shipping interests are keen to move assets swiftly via ice-diminished polar seas rather than through equatorial canals. Given this trend, the military has an operational interest in the Arctic, including for search and rescue purposes. Many other communities are interested in Arctic change, for reasons ranging from energy extraction to subsistence hunting. The evolving sea ice cover and changing freshwater dynamics of the Arctic Ocean have many human dimensions, and yet the polar regions remain challenging to observe.

Therefore, a key component of this dissertation work has been the use of airborne measurements and satellite remote sensing to quantify ocean change over periods and areas of otherwise restricted access. Supported by the Office of Naval Research and in partnership with U.S. Coast Guard Air Station Kodiak, the Seasonal Ice Zone Reconnaissance Surveys (SIZRS) program described in Chapter 2 takes advantage of monthly Arctic Domain Awareness C-130 flights to collect hydrographic and atmospheric data along repeat sections. The use of aircraft has

created access to the ice-covered ocean at locations and in times when ship-based observation would be impossible. In a field where observation has traditionally been costly and relied on ice camps and icebreaking ships, the ongoing use of these aerial platforms as well as enhanced satellite remote sensing capabilities represents a crucial advance.

To address the pertinent geophysical facets of western Arctic Ocean regional change, this dissertation:

- Quantifies freshwater exchange between sea ice and the surface ocean in the seasonal ice zone (SIZ)
- Evaluates the role of sea ice motion and changing ocean velocity in large-scale freshwater dynamics and local ice-ocean momentum transfer
- Explores the role of satellite remote sensing and airborne hydrographic tools for addressing questions of climate in the high latitudes

1.2 Chapter Summaries:

Chapter 2: *Local, vertical processes: the mixed layer and its FWC.*

The first part of this thesis discusses local, vertical mechanisms for freshwater accumulation in the Beaufort Gyre SIZ. We argue that during summer, freshwater enters the surface ocean from sea ice melt, causing salinity to align with the meridional ice edge position. In addition, we use a one-dimensional model to show that this process can be considered as a one-dimensional vertical mixing process. Given the literature's attention to horizontal freshwater accumulation in the

region, this vertical result is somewhat novel. By establishing the relationship of gyre shape to the monthly Arctic Oscillation index (AO; Thompson & Wallace, 1998) at two-month timescales, this chapter sets the stage for the second part of the thesis, which discusses large-scale, primarily horizontal, mechanical controls on freshwater accumulation. A major outcome of this chapter is that local one-dimensional processes influence the upper ocean coherently across the Beaufort Sea, even as the background gyre in which they occur is moving actively. Sea ice controls these vertical processes, as both salinity and temperature show clear behavior with respect to the ice edge at a basin scale.

Chapter 3: *Large-scale horizontal dynamic processes: basin FWC and equilibration.*

A key advance in the latter parts of this thesis is the use of satellite-derived geostrophic velocities in the calculation of ice-ocean stress, which previous studies have neglected. We argue that especially due to the recent spin-up of the Beaufort Gyre, these velocities may no longer be dismissed. They are crucial to accurately calculating ocean surface stress curl and resultant freshwater accumulation or discharge. While ice-ocean models have heretofore been the primary tools for tackling this problem, this chapter is one of the first observational attempts to illustrate surface stresses and resultant Ekman pumping at this scale using ice, wind, and ocean data. Cumulatively integrating Ekman pumping through time shows that the surface stress curl reversals, more than hypothesized eddy flux, are a leading-order contributor to observed Beaufort Gyre stabilization.

Chapter 4: *Using remote sensing to revisit foundational dynamic calculations.*

Chapter 3 emphasized the ocean's role in changing ice-ocean stress, and that stress as a mechanism for gyre equilibration. It along with most ice ocean modeling studies relied on a geostrophic drag coefficient derived from observations in the early 1970s. Chapter 4 investigates how that geostrophic ice-ocean drag coefficient and its turning angle may have changed in recent decades. Observational studies of ice-ocean stress in both the recent and distant past have relied on ice-based measurements from camps and platforms such as ice-tethered profilers. With the benefit of satellite and buoy observations of ocean and ice velocity, we can use remote sensing to construct a stress balance on sea ice under the assumption of free drift (that is, neglecting internal ice stress during periods of low ice volume). We explore how and why the ice-ocean stress coefficient has decreased and its turning angle has increased, evaluating the relative influences of wind, water, Coriolis, and internal stresses before ultimately constructing a five-year climatology of coefficients and turning angles in the Beaufort Gyre.

Appendix: *Circulation timescales, averaging, and adjustment.*

The same satellite tool that in Chapter 3 yielded geostrophic ocean velocities takes center stage in this appendix to the thesis: dynamic ocean topography (DOT), which describes the sea surface height relative to the geoid. Following similar modeling studies, this investigation uses observational tools and a calculated magnitude squared coherence to relate DOT to ocean bottom pressure (OBP) to evaluate the timescales on which the ocean behaves baroclinically versus barotropically. This relationship illustrates the effect that forcing fields and timescales have on the dynamics that distribute freshwater throughout the Arctic Ocean; this thesis section links the large-scale atmospheric forcing (i.e., AO) from Chapter 2 with the horizontal dynamics of

Chapter 3. Because the satellite data fields cover the full Arctic Ocean, this appendix sets the stage for future work expanding our forcing discussion beyond the Beaufort Gyre.

Chapter 2: *Local, vertical processes: the mixed layer and its FWC.*

An edited version of this chapter was published by AMS. Copyright (2017) American Meteorological Society: Dewey, S.R., Morison, J.H. and Zhang, J., 2017. An Edge-Referenced Surface Fresh Layer in the Beaufort Sea Seasonal Ice Zone. *Journal of Physical Oceanography*, **47(5),** pp.1125-1144. doi:10.1175/JPO-D-16-0158.1

2.1 Introduction

The Beaufort Sea Seasonal Ice Zone (SIZ) is the area of the Canada Basin that lies between minimum and maximum annual sea ice extents. The SIZ encompasses the ice edge and the Marginal Ice Zone (MIZ) as they move north and south each year, in conditions ranging from full ice cover to open water. Based on this definition of the SIZ, its size is variable. In 2012 the September SIZ along 150°W reached northward of 80°N; in 2014 it extended merely to 75°N.

The variability of such an area and the fragility of the first-year ice it principally contains motivate the study of the underlying ocean, especially since the Beaufort Sea and Canada Basin account for the greatest recent loss in Arctic multiyear sea ice extent (Maslanik et al., 2011). This emerging influence of sea ice is due in part to the youth of the Beaufort Sea SIZ as we know it today; Comiso et al. (2008) note the marked retreat of the western Arctic ice edge relative to satellite-derived climatology, and Rabe et al. (2014) observe an increase of freshwater storage contemporary with sea ice decline in many parts of the Arctic Ocean.

Seasonal Ice Zone Reconnaissance Surveys (SIZRS) is a program of repeated ocean, ice, and atmospheric measurements across the Beaufort Sea SIZ designed to track and understand the interannual variability of the SIZ. These measurements are taken aboard United States Coast Guard Arctic Domain Awareness (ADA) flights of opportunity using aircraft expendable atmosphere and ocean probes. They are designed to capture full air and water column properties in variable ice conditions spanning the SIZ. In addition to these sections, SIZRS buoy deployments provide continuous time series in several locations in the SIZ.

Hydrographic data gathered as part of SIZRS have shown that the summertime upper ocean temperatures along the 150°W line above 50 m depth have increased up to 2°C, and salinities have decreased as much as 5 psu relative to summertime climatologies (Timokhov and Tanis, 1997; Boyer et al., 2012; Johnson et al., 2012; Seidov et al., 2014). The SIZRS dataset enables us to quantitatively characterize this relationship through the Canada Basin and through the melt season.

As the SIZ distinguishes itself from long-term averages, a coherent pattern emerges in its behavior. When the background gyre signal in salinity is removed, the salinity in the upper 20 m of the Beaufort Sea SIZ registers significantly with the ice edge, independent of year and latitude, and the seasonal appearance of an observed fresh layer relative to the edge is determined almost exclusively by the change in sea ice extent.

2.2 SIZRS Observations

The SIZRS stations are typically at each degree latitude at least from 72°N to 76°N along the 140°W and 150°W lines of longitude in the Beaufort Sea. To capture the full extent of the SIZ, from open water to ice-covered areas, sampling in some years has extended farther north. The annual minimum ice edge in the western Arctic had already been retreating farther north (Drobot et al., 2008), but in September of 2012 ice extent was the lowest of the satellite record and SIZRS sampling extended to 80°N, 150°W to reach sea ice.

SIZRS sampling times are designed to capture the full arc of the SIZ melt season, with repeat occupations of the survey lines each month. Sampling in 2012 began in May; in subsequent years sampling started in June to increase the likelihood of finding completely open leads free of new ice (more than minimal surface ice prevents the expendable probes from

deploying properly). Sampling usually concludes in October, though the 2013 field season ended in August due to suspended Federal government operations. Despite these gaps in temporal coverage, the SIZRS dataset offers unique *in-situ* snapshots of the SIZ even during months of limited ship access. In this analysis we focus on the 150°W line because it has the most continuous record of observations and thus provides more information for analysis and modeling than the 140°W line, the occupation of which only began in 2013.

Instrumentation for the hydrographic portion of the SIZRS missions is a Tsurumi-Seiki (TSK) Aircraft eXpendable Conductivity, Temperature, and Depth probe (AXCTD), first deployed in the Canada Basin as part of an International Polar Year hydrographic survey (McPhee et al., 2009), and similar to the Sippican instruments used in the Eurasian Basin by Childers and Brozena (2005). McPhee et al. (2009) compared AXCTD profiles to surface-deployed CTD profiles and found TSK AXCTDs accurate to 0.02 psu and 0.02°C. Probe depth is determined by fall-rate calculation and accurate to 2% with a resolution of 0.11 m and a maximum depth of 1100 m; in the modeling portion of this present study, hydrographic data are smoothed to 1-m resolution to reduce instrument noise.

During the SIZRS ADA flights, the AXCTDs were dropped into open leads from C-130H Hercules aircraft flying at speeds of 60-70 ms^{-1} and altitudes of 60-120 m. Data were transmitted in real time to one of the aircraft's antennae as a 172 MHz FM radio signal, converted to engineering units by a TSK converter, and recorded on a laptop computer. The raw telemetered data stream is also archived on a solid-state sound recorder. Comparisons with ITP data (whoi.edu/itp), UpTempO data (psc.apl.washington.edu/UpTempO), and with ship cruise data (whoi.edu/website/beaufortgyre/data) indicate no significant differences between our full-depth profiles and those in similar Arctic ice conditions.

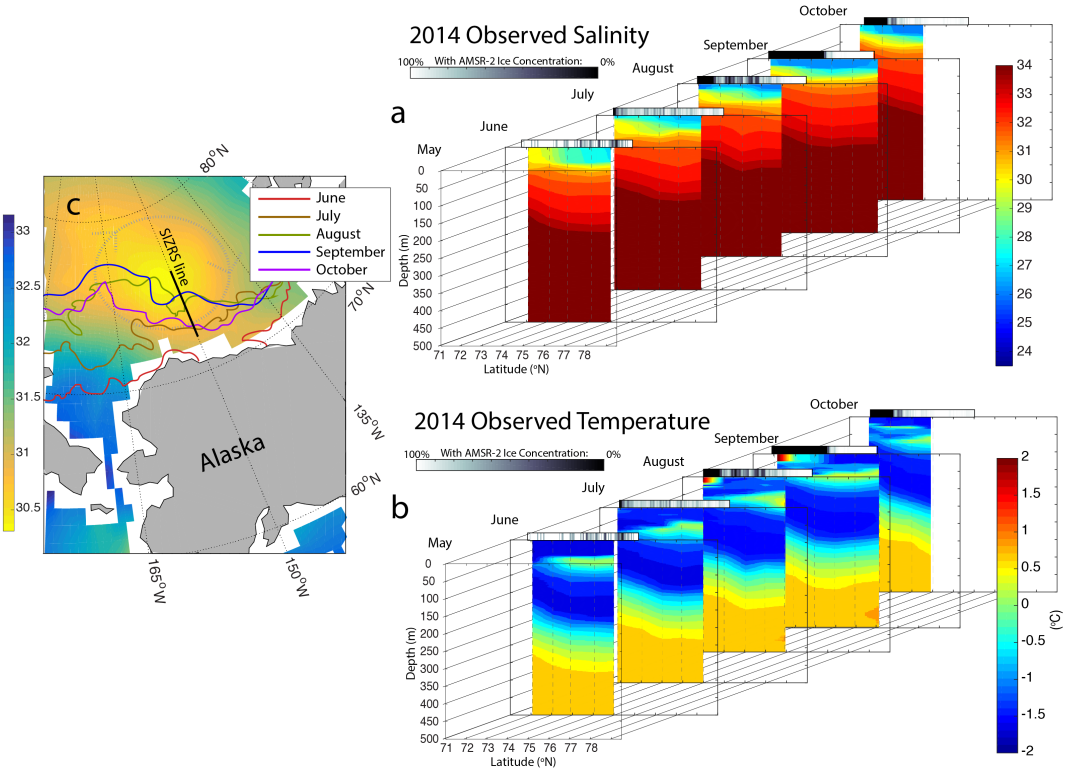

Figure 2.1 Sections of salinity **(a)** and temperature **(b)** to 500m are shown with over-plotted AMSR-2 sea ice concentration on the date of deployment. The SIZRS 150°W line is also shown in its regional context, against lines representing the 15% AMSR-2 ice edge average for the week of each deployment in 2014, a dashed circle indicating the typical position and direction of the Beaufort Gyre, and summer climatological 30-m salinity from the PHC3.0 climatology (Steele et al., 2001) indicating the gathering of freshwater in the center of the gyre due to Ekman convergence **(c)**.

2.3 Observational Analysis

The evolution of temperature and salinity along 150°W during 2014 was typical of SIZRS seasons. Figure 2.1b shows how the surface ocean warms in response to receding ice cover in August and September and how that heat may be trapped as a near-surface temperature maximum (NSTM) with the onset of freezing in October. The summer Pacific Water layer is visible at 50-70 m depth.

As in each previous year, 2014's SIZRS salinity sections reveal the formation of a near-surface low-salinity layer south of the ice edge, extending farther north following the ice edge (Figure 2.1c) and growing deeper as the season progresses (Figure 2.1a). This observation can be explained as the freshening of the near surface layer by melting ice. A sample calculation of the change in freshwater content (FWC) between June and September 2014 at 74°N 150°W illustrates this. Following Carmack (2008), we consider the FWC (in meters) to be

$$\mathrm{FWC}_{\mathrm{ocean}} = \int_{2}^{20} \frac{34.8\text{-}S(z)}{34.8} dz \qquad (2.1)$$

where salinity data are smoothed to 0.5-m depth resolution, and the top 2 m of data are excluded to eliminate the effects on salinity measurements of any AXCTD sensor start transients or local lead effects. This is reasonable because owing to mixing, we expect that the salinity in the top 2 m to be nearly the same as the salinity at 2 m depth. While in the summertime central Arctic Ocean, a freshened surface layer can develop in the leads between ice floes under quiet conditions (Hayes and Morison, 2008), SIZRS has not generally sampled under such conditions. In the early part of the SIZRS season there has been limited melt, and later in the season the very near surface is reasonably well-mixed as the ice concentration decreases and floes move in free drift. However, as a test of the sensitivity of the FWC calculations to this assumption, we assume an extreme case where the 2 m is 0.5 psu less than the ambient mixed layer salinity, and the effect would be a reduction in FWC of 0.1 m.

The melt season change in FWC in the top 20 m of this station is taken as the difference between the September and June integrals. We assume a mean sea ice salinity of 10 psu and June

and September ice thicknesses of 1.25 m and 0.6 m, respectively, per Lindsay and Schweiger's (2015, see their Figure 4) recent climatological study of sea ice thickness. Under this assumption, we calculate the FWC of the sea ice in equivalent meters of freshwater by multiplying sea ice thickness (H_{ice}) by the local AMSR-2 average sea ice concentration (SIC) for the week of each SIZRS measurement; this value is then scaled by the density ratio of sea ice (ρ_{ice}) to freshwater (ρ_{FW}) sea ice salinity (S_{ice}), in psu, to estimate the amount of freshwater yielded by melt:

$$FWC_{ice} = \frac{\rho_{ice}}{\rho_{FW}} * H_{ice} * \frac{SIC(\%)}{100} * (1\text{-}S_{ice}) \qquad (2.2)$$

Thus, the FWC change (FWCC) of the ocean balances the loss of sea ice:

$$FWCC_{ocean} = \int_2^{20} \frac{34.8\text{-}S_{Sept}(z)}{34.8} dz \; - \; \int_2^{20} \frac{34.8\text{-}S_{June}(z)}{34.8} dz = 1.04 \text{ m} \qquad (2.3)$$

$$FWCC_{ice} = \frac{900 kgm^{-3}}{1000 kgm^{-3}} * 0.6 \text{ m} * 0.049 * \left(1 - \frac{10}{1000}\right) - \frac{900 kgm^{-3}}{1000 kgm^{-3}} * 1.25 \text{ m} * 0.996 *$$

$$\left(1 - \frac{10}{1000}\right) = \text{-}1.08 \text{ m} \approx \text{-}FWCC_{ocean} \qquad (2.4)$$

Any difference between the FWC values of the melting ice and the upper ice-free ocean replacing it could be attributed to horizontal advection or uncertainty in the values of sea ice salinity, thickness, or concentration. Assuming ±10, ±0.2 m, and ±10%, respectively, the FWCC can change by ±0.24 m.

The comparison is crude but the difference between the freshwater input by the melting ice and the change in observed fresh water content does have a difference of 4 cm. This difference suggests that 4 cm worth of freshwater from ice melt did not remain where the ice

melted but was advected away. These very rough, observationally-based estimates indicate 96% of the SIZ salinity change is due to vertical mixing and 4% associated with horizontal advection and other process that remove freshwater. Accounting for uncertainty in sea ice FWC, we find that this salinity change ranges from 81% to 100%.

Because of the first-order role of ice melt and the apparent relationship of surface salinity to distance north or south of the ice edge, it is useful to view the SIZRS data in a reference frame relative to the ice edge rather than to station latitude. To accurately locate the ice edge in a MIZ characterized by highly variable ice concentrations, we use weekly mean sea ice concentration from the AMSR-2 (2013 and 2014; 3.125-km resolution) and SSM/I (2012; 25-km resolution) passive microwave satellite data. The southernmost incidence of a threshold concentration is

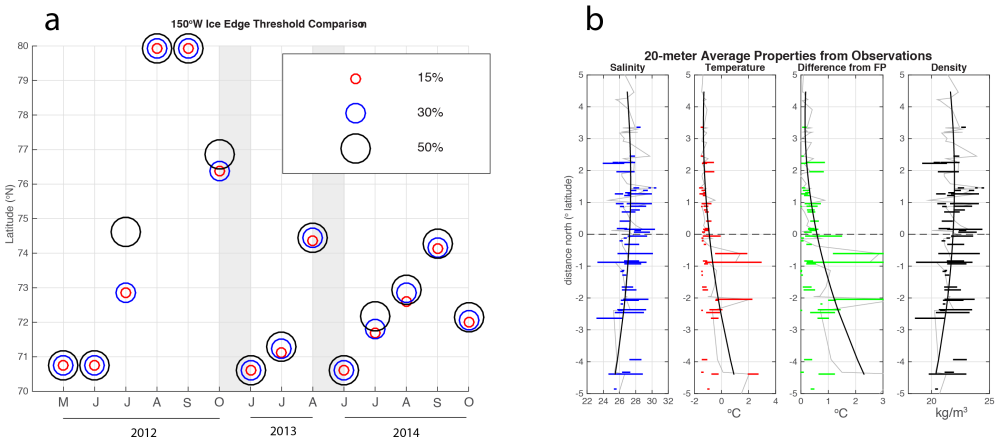

Figure 2.2 (a): Comparison of sea ice edges from SSM/I (2012) and AMSR-2 (2013-2014) passive microwave products. Concentric circles indicate agreement in ice edge position between concentration thresholds. The largest disparities in ice edge position occur at the beginning and end of the SIZRS season, during the onsets of melt and freeze-up. The resolution of the SSM/I data is 25 km, and the AMSR-2, 3.125 km. **(b):** 20-m averages (gray) of salinity, temperature, difference from calculated freezing point, and density from all deployments on 150°W relative to the 15% ice edge. Thick black lines show a quadratic fit to the data, and colored bars display the full range of values at each distance. Average salinity values decrease both to the north and south of the ice edge, while temperature increases above the freezing point south of the ice edge. Variance in temperature is substantially greater to the south of the ice edge, as insolation heats open water, whereas salinity variance remains relatively consistent throughout the section.

considered the edge. For 15%, 30%, and 50% threshold concentrations, ice edges are nearly indistinguishable at the resolution of the satellite products except during the onsets of melt in July and freeze-up in October (as signified by the decrease and increase in sea ice extent along the 150°W section; see Figure 2.1c and Figure 2.2a). Because these products have trouble distinguishing melt ponds from open water, and may therefore underestimate sea ice concentration (Rösel et al., 2012), overlap of the 15% and 50% edges increases our confidence in having located an edge. We therefore use 15% concentration as the definition of the ice edge, in keeping with the National Snow and Ice Data Center definition of sea ice extent.

In quantifying the relationship of the surface layer to the ice edge, we look at the upper 20 m of the water column. This depth lies above sources of stored heat like the Near-Surface Temperature Maximum (Jackson et al., 2010) and Pacific Summer Water (Steele et al., 2004) and within typical mixed layer depth ranges for the Beaufort Sea and Canada Basin (Toole et al., 2010; Peralta-Ferriz and Woodgate, 2015). To avoid overlap with these features, we consider the average properties above them—that is, 20-m mean salinity and temperature.

The upper 20-m mean temperatures plotted versus ice edge position defined above (Figure 2.2b) support the idea of similar salinity patterns moving with the ice edge. They become highly variable south of the ice edge and stay consistently within 0.5°C of the freezing point under the ice. While some portion of this heat could be from warming Pacific inflow through the Bering Strait (Shimada et al., 2006; Woodgate et al., 2006), Steele et al. (2010) find that 77-83% of surface layer warming in the Pacific Arctic comes from local radiative heating, and the contribution of Bering Strait inflow is limited to the southern Beaufort Sea nearest to the Alaskan coast. While Steele et al. (2010) perform this calculation for the upper 60 m of the water column,

we will show one-dimensional model analysis with SIZRS data (see Section 4) also supports local, predominantly solar warming in the upper 20 m.

The 20-m mean salinities for each station registered relative to the ice edge position (Figure 2.2b) also reveal a pattern on the scale of the SIZ. The water reaches peak salinity slightly north of the ice edge and freshens away from the edge to the north and south. The location of the peak salinity is pushed northward in late-summer to early-autumn months (August through October) as water to the south freshens due to ice melt.

The freshening well to the north of the ice edge indicates that melt is not the only influence on this 20-m average salinity. This northern upper ocean freshening is a component of the anticyclonic Beaufort Gyre circulation (Proshutinsky, et al., 2009). Figure 2.1c illustrates the location of the Beaufort Gyre with the PHC 30-m salinity climatology for winter (Steele et al., 2001) when the anticyclonic circulation is typically strongest, and a sketched circle representing the circulation pattern. The SIZRS upper ocean salinity along 150°W (Figure 2.3a) shows a minimum in the northern third of the section at the middle of the Beaufort Gyre. Two features stand out when SIZRS measurements are compared to the National Ocean Data Center (NODC) salinity climatology (Seidov et al., 2015; Figure 2.3b): basin-wide, the upper ocean is fresher in SIZRS observations, and that freshening is greatest in the middle of the gyre and just south of the ice edge (Figure 2.3c). It seems clear that the spatial variation in observed upper ocean salinities results from a mix of SIZ signals and larger-scale influences largely independent of ice edge position and associated with the Beaufort Gyre.

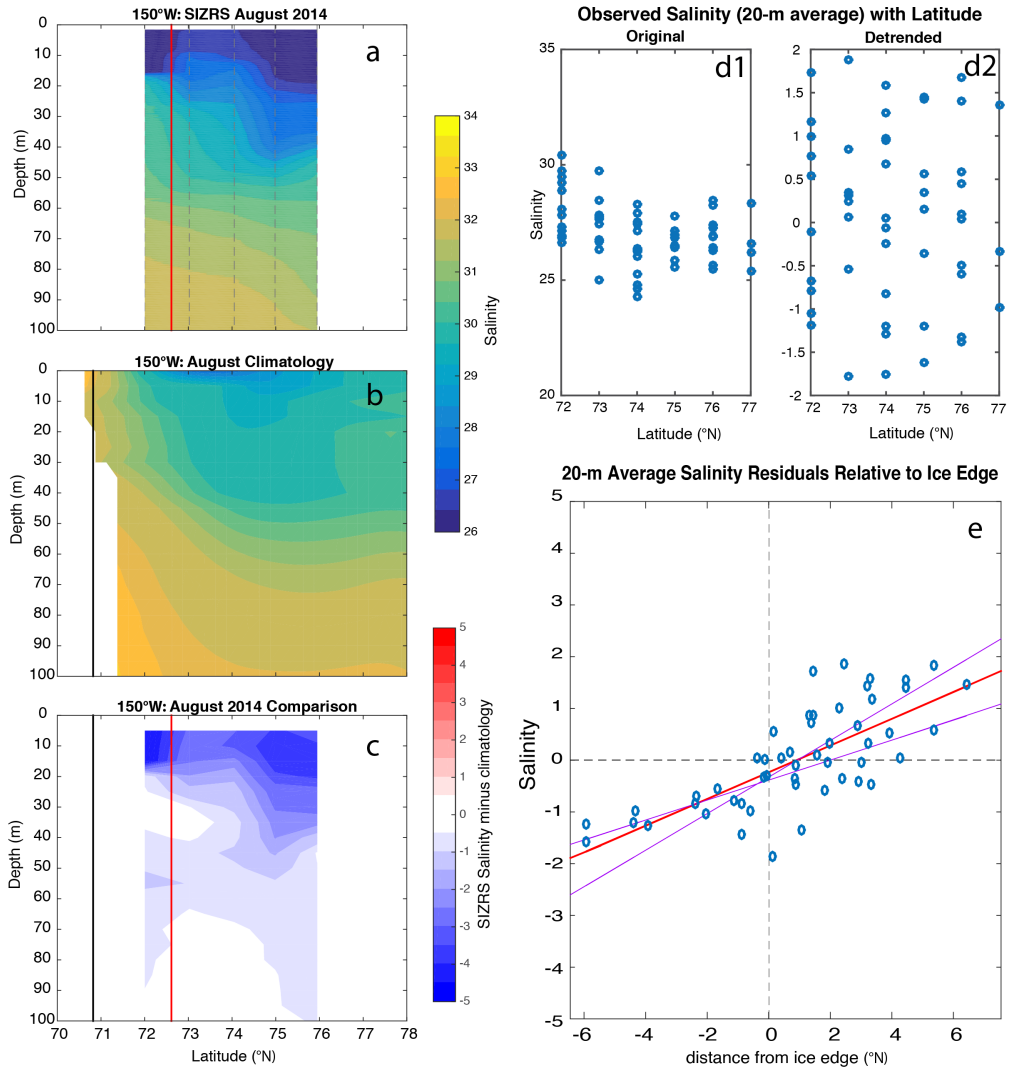

Figure 2.3 (a-c): Comparison of SIZRS data to regional monthly climatology along 150°W. Observed ice edge is overplotted in red; climatological ice edge is overplotted in black. (Each employs a 15% concentration threshold, with the first using AMSR-2 passive microwave product and the second NSIDC's monthly sea ice concentration climatology from passive microwave data, available at http://nsidc.org/data/smmr_ssmi_ancillary/monthly_means.html.) SIZRS drop locations are shown with dashed gray lines in a. The National Ocean Data Center climatology (b) uses World Ocean Atlas data through the end of 2011. 4c shows the difference in salinity, in psu, when the climatology is subtracted from the SIZRS data. Areas of maximum freshening are found at the 2014 ice edge and at the center of the Beaufort Gyre (~75°N, see also Figure 2.4). **(d1-d2):** 20-m average salinities from all months and all years versus latitude, before (d1) and after (d2) removing the gyre signal. **(e):** Salinity residuals after removal of the AO-correlated gradients are plotted versus ice edge distance. When the gyre signal is removed, residual values correlate significantly with distance from the ice edge. The blue circles show residuals from all SIZRS months in 2012-14; the red line is a linear fit to the data, and the purple lines are extrema for such a fit, generated in a 1000-iteration bootstrap simulation.

In the anticyclonic Beaufort Gyre system freshwater is gathered at the mid-basin (e.g., Proshutinsky et al., 2009) by Ekman transport convergence of near surface water by the anticyclonic winds of the Beaufort High. North of the ice edge, the meridional gradient in our observed 20-m average salinities is an expression of the upper ocean freshening and surface doming of the Beaufort Gyre (Figure 2.4b). The center of the gyre varies slightly with time, but lies between 72.4°N-74.4°N and 139°W-151°W according to satellite-derived dynamic ocean topography (Morison et al., 2012; Giles et al., 2012) and at 73.5°N and 143°W from *in situ* observations (Proshutinsky et al., 2009). Dynamic height calculations to a reference depth of 500 m using the Monthly Isopycnal and Mixed-layer Ocean Climatology (MIMOC) and NODC climatologies (Johnson et al., 2012; Seidov et al., 2015) show the center of the Beaufort Gyre dome on 150°W falls at 74°N-75°N; this center latitude aligns with location of the minimum, SIZRS-observed 20-m salinity, which falls between 73°N and 75°N (Figure 2.4b). An increasingly negative salinity gradient in this latitude range indicates an increase in Beaufort Gyre doming and intensity.

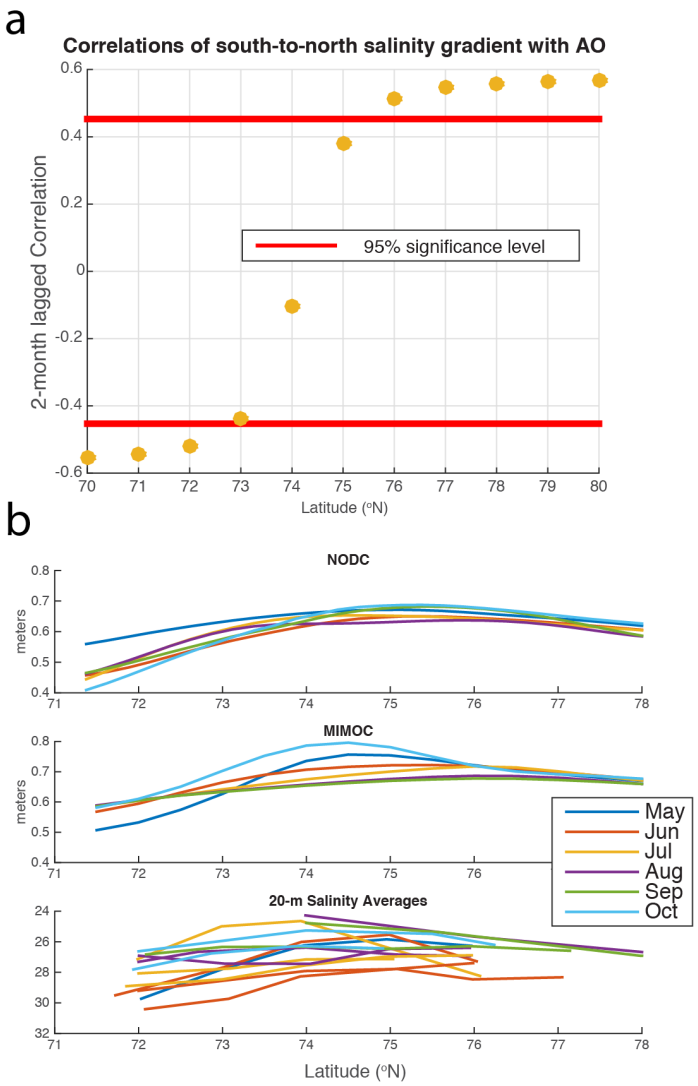

Figure 2.4 (a): Correlations of a northward gradient in 20-m average salinities at each degree from 70°N-80°N with the 2-month-lagged AO. **(b):** Comparison of dynamic heights calculated from NOAA and MIMOC monthly climatologies along 150°W. These heights indicate that the center of the Beaufort Gyre lies between 74°N and 75°N on 150°W. 20-m mean salinities for every SIZRS monthly survey are shown in the bottom panel; the latitudes of peak salinity occur at or just south of the center of the gyre, as derived from calculated dynamic height relative to 500 m.

We thus find that the salinity pattern associated with the ice edge is superposed on the gyre-scale salinity patterns. To more clearly show the ice edge salinity pattern, we must identify and remove the time-varying gyre signal without eliminating the ice-edge signal. To achieve this separation, we seek metrics of the strength of the Beaufort Gyre and the associated salinity gradients that are independent of the near-surface salinity data themselves. For this we consider

three proxies for gyre strength: the monthly Arctic Oscillation (AO) index, tilt of isopycnals in the halocline, and ocean bottom pressure near the middle of the Beaufort Gyre.

The AO is the leading principal component of monthly mean sea level pressure anomalies in the Northern Hemisphere (Thompson and Wallace, 1998) taken here from the NCEP/NCAR reanalysis (http://www.cpc.ncep.noaa.gov/products/precip/CWlink/daily_ao_index/monthly.ao.index.b50.current.ascii.table).

A quadratic fit to the 20-m average salinities for each section is used to create an array of northward salinity gradients at each latitude for all months. (The mean R^2 value for all of these monthly fits is 0.82, and the median is 0.92.) These arrays correlate significantly (>95%) at a two-month lag with the monthly AO index (Figure 2.4a), indicating that large-scale atmospheric processes do in fact control the overall shape of salinity across the gyre, but that the oceanic response to atmospheric forcing is delayed.

The sign of the correlation between northward salinity gradient and AO is negative to the south and positive to the north, inflecting between 74°N and 75°N. This sign change reflects the behavior of the gyre dome along 150°W. The sea surface height tendency of the Beaufort dome is opposite to the salinities, because the fresher water lies in the middle of the gyre. The correlation pattern of Figure 2.4a indicates that as the lagged AO increases, the dome steepens and the northward salinity gradient to the south of the gyre center becomes more negative. To the north, the gradient becomes more positive. The opposite is true as the AO shifts to its low regime, so that the lagged AO is always negatively correlated with the salinity gradient south of 74°N-75°N and positively correlated north of those latitudes. The correlation magnitude is

significant everywhere except in the center of the gyre dome, because the salinity gradient is always near zero at the center of the gyre (Figure 2.4a).

The positive correlation between lagged AO and the strength of the Beaufort Gyre may seem counterintuitive, since high AO is generally associated with cyclonic circulation and the Beaufort Gyre is an anticyclonic feature. The reason for the positive correlation lies in the location of the center of action of the AO relative to the Beaufort Gyre. Morison et al. (2012, Figure S1) have identified two expressions of the AO in the Arctic Ocean circulation. In an idealized low-AO anticyclonic regime, the anticyclonic flow of the Beaufort Gyre extends to the northwest and includes the East Siberian Sea; in a high-AO cyclonic regime, the Beaufort Gyre is restricted to the central or eastern Canada Basin and a cyclonic circulation dominates the Russian side of the Arctic Ocean. This arrangement means that an increase in the AO results in strengthened northeastward wind stress on the northwest part of the Beaufort Sea and increased Ekman pumping of near-surface water towards the center of the Beaufort Gyre, and while the areal coverage of the Beaufort Gyre may decrease, its intensity increases (Morison et al., 2012). After a lag to allow the Ekman pumping to accumulate, this translates into increased freshwater content and doming of the gyre along 150°W.

The 2-month-lagged AO index may therefore be treated as a proxy for gyre strength and used to separate basin-scale salinity signals from the fresh wake of a retreating sea ice edge. A lagged regression of the standardized 20-m salinities onto monthly AO at each latitude through time gives the salinity value attributable to gyre effects. Subtracting this value from the measured salinities yields a set of salinity residuals that correlates significantly (Figure 2.3e; Table 2.1) with distance from the ice edge. The ratio of the variance of these residuals to the variance of the 20-m average salinities is 0.6, so the residual salinity changes after removing the doming signal

correlated with AO amount to $(0.6)^{1/2}$ or 77% of the total variability. This is slightly less than the 81% to 100% variability we attribute to 1-D processes based on earlier estimates, but is reasonable considering that it represents an average including the northern part of the Beaufort Gyre not subject to the extreme surface fluxes of the SIZ.

Another proxy for gyre strength is the along-section slopes of two different isopycnals, σ_θ = 24 kgm^{-3} and σ_θ = 26 kgm^{-3}. These isopycnals fall between the depths of 10-60 m and 90-140 m, respectively, during SIZRS sampling. Similar to the 20-m average salinities, the depths of the σ_θ = 24 kgm^{-3} and σ_θ = 26 kgm^{-3} isopycnals follow a parabolic curve across the sampled latitudes. (For a quadratic fit, mean and median R^2 values for all monthly fits to the σ_θ = 24 kgm^{-3} fit are 0.79 and 0.80, respectively; for σ_θ = 26 kgm^{-3}, they are 0.84 and 0.89.) We correlate the slopes of these fits at each latitude with the meridional 0 to 20-m average salinity gradients. As in the AO correlation, these slopes correlate negatively with northward salinity gradients at lower latitudes, and positively at higher latitudes, changing sign at 75°N. We use a similar regression to that of the first (AO) case, replacing the monthly AO index with these isopycnal slopes and evaluating the correlation at zero lag. The residual salinity differences correlate significantly with distance from the ice edge (Table 2.1).

A third proxy for gyre strength is the Woods Hole Beaufort Gyre Exploration Project (BGEP) bottom pressure data (http://www.whoi.edu/beaufortgyre/data_moorings.html), from moorings at 75°N and 78°N on 150°W. This ocean bottom pressure is related to gyre spin-up at monthly time scales because circulation changes at these time-scales include a strong barotropic component [*Vinogradova et al.*, 2007]. Raw ocean bottom pressure (OBP) data concurrent with SIZRS measurements are taken from the BGEP site (http://www.whoi.edu/beaufortgyre/home) and de-tided using t_tide (Pawlowicz et al., 2002). The timeseries are de-meaned to account for mooring turnover in August of each year, and correlated with monthly AO indices and with SIZRS 20-m average salinity gradients northward. The pressures correlate significantly with AO indices at a two-month lag, though not significantly with the salinity gradients. When regressing

Table 2.1 Correlation coefficients (r-values) of salinity residuals with ice edge distance for each method. Bolded correlations have a p-value less than 0.001. Here p-value is the probability (0-1) that we would have collected the data we did had there been no relationship between salinity and distance from ice edge; the p-value acts as a measure of significance for the correlation. The last two rows show the correlation of upper-ocean salinities to ice edge distance if a quadratic fit to the data is removed, or if no fit is removed at all.

Gyre Proxy	**r** All Data (May – Oct)	**r** Autumn (Aug – Oct)	**r** Spring (May- July)
Lagged AO	**0.73**	**0.77**	**0.67**
$\sigma_\theta = 24$ kgm^{-3}	**0.58**	**0.64**	0.31
$\sigma_\theta = 26$ kgm^{-3}	**0.57**	**0.62**	0.25
BGEP A (75°N)	**0.59**	**0.72**	0.23
BGEP B (78°N)	**0.59**	**0.72**	0.23
Quadratic S-N fit	0.13		
No signal removed	0.38		

these SIZRS northward salinity gradients at each latitude onto the pressure time series, the difference in pressures between the two pressure gauges is so slight (the meridional gradient is on the order of 0.01 mm per degree latitude) as to produce identical correlations between the residuals from this regression and the distance from the ice edge. OBP, like the other proxies, yields higher correlations in the fall than in the spring (Table 2.1), likely due to the enhanced role of early summer melt in changing surface layer salinity.

For each proxy, we can establish that the relationship of salinity residuals to edge distance is statistically sound by using the 1000-iteration bootstrap sampling of Efron (1979). A Monte Carlo test with replacement, bootstrapping uses a probability distribution taken from the data rather than a normal distribution. The replacement of some values in the set with redundant values ensures that not all of the 1000 resamplings are identical and that the relationship to ice edge holds when some data pairs are missing or duplicated. We run this bootstrap analysis on a linear fit to our plotted salinity residuals vs. distance from the ice edge. This analysis generates upper and lower bounds for the linear fit (see magenta lines on Figure 2.3e for the AO proxy), showing that the relationship of salinity to edge distance is statistically robust and that the values of all salinity residuals from each proxy become more positive heading north. Standard errors in the slopes are minimal in the autumn case and at a maximum during spring runs, emphasizing again the role of melt in determining the presence of an ice-edge-referenced fresh layer.

Using three different proxies for the strength of the background gyre, we have separated the signals of basin salinity and ice-edge-influenced salinity. Having correlated monthly AO and bottom pressure to northward salinity gradients, we have shown that those parameters as well as isopycnal tilt may all be used to approximate gyre strength and yield the same general spatial pattern in salinity. Of the three proxies, the lagged AO delivers the strongest correlations (Table

2.1). This relationship only holds for salinity. The 20-m average temperatures do not correlate significantly with any of the gyre proxies used, a result that reinforces the role of local insolation in determining upper-ocean heat content.

2.4 Application of the PWP model to the SIZ

The relationship between salinity and distance to the ice edge, and the correspondence of observed upper ocean salinity change with observed ice melt, suggest that ice melt and vertical mixing in the surface layer are the primary drivers of the evolution of SIZ salinity changes through the summer. This implies that horizontal advection is secondary— salinity changes are largely due to freshwater entering the ocean at the surface rather than being advected into the sites of the SIZRS stations from elsewhere. If this essentially 1-D view of SIZ upper ocean processes is true, it should also be reflected in the evolution of the thermal and density structure of the upper ocean given reasonable estimates of surface thermal and stress forcing. Therefore, to test the hypothesis that 1-D mixing processes are dominating the evolution of the SIZ upper ocean structure, we develop and use a SIZ adaptation of the 1-D mixing model of Price, Weller, and Pinkel (1986), hereafter referred to as the PWP model, to see if it can simultaneously account for the observed upper ocean thermal, density, and salinity changes in the SIZ.

Our implementation of the PWP uses radiative, sensible, and latent heat fluxes; zonal and meridional surface stresses; and freshwater flux to make adjustments to the top cell of an ocean depth grid. Following the usual PWP formulation, at each time-step, heat fluxes are first combined to calculate the thermal change to the top grid cell. Then freshwater fluxes are used to calculate a new salinity for the top grid cell. A density profile is computed and static instability is removed by mixing each cell with the one below it until the density profile is stable. After this

stabilization, momentum from surface stress is added to the mixed layer cells at the top of the array (the mixed layer cells are those where the density difference between cells is less than $5x10^{-4}$ kgm^{-3}). Velocities in the mixed layer are free to rotate at the inertial frequency. The array is then adjusted for stability at the base of the mixed layer by mixing the base cell and that just below it until they meet threshold criteria for two different Richardson numbers. Mixed-layer stability uses the bulk Richardson number, and shear flow instability the gradient Richardson number:

$$R_{bulk} = \frac{g \Delta \rho h}{\rho_0 (\Delta V)^2} \quad , \quad R_{grad} = \frac{g \partial \rho / \partial z}{\rho_0 (\partial V / \partial z)^2} \qquad (2.5)$$

where V is the horizontal velocity vector, h is the depth of the mixed layer, and deltas are taken to be the difference in values between the cell at the base of the mixed layer and the cell just below it. The adjusted arrays for temperature, salinity, and density are then saved and subject to the next time-step's fluxes.

Sea ice presents a challenge in accurately estimating the surface fluxes that drive the PWP model simulations of polar oceans. Previous implementations of a high-latitude PWP (Hyatt, 2009; Toole et al., 2010) have incorporated a flux law with summertime basal melting following Maykut & McPhee (1995) and a constant wintertime upward heat flux. We opt to use the output of a separate, three-dimensional ice-ocean model, the Marginal Ice Zone Modeling and Assimilation System (MIZMAS), to provide ocean surface fluxes. MIZMAS is a regional ice-ocean model derived from the Pan-Arctic Modeling and Assimilation System (PIOMAS) (Zhang et al., 2008a; Zhang et al., 2008b).

We take the hybrid approach of using MIZMAS to drive the simpler 1-D model for

several reasons. While this approach cannot capture the ocean changes that stem from such things as the ice-ice and ice-ocean interaction and advective effects simulated by the much more complete and sophisticated MIZMAS model, it serves to isolate the effect of 1-D mixing. Because our explicit goal is to test the observation-based hypothesis that upper ocean evolution during ice edge retreat is primarily a 1-D mixing process, we do not want to cloud the conclusion with the possibility that more involved model physics are at play in the simulations. At the same time, even in this 1-D view the surface forcing at one location varies with time according to the atmospheric forcing and the state and rate of change of the overlying ice cover. The surface stress, ice growth, and melt simulated by the more complete model drives our PWP runs without the requirement that we build a separate ice model or make many simplifying assumptions about ocean, momentum, heat, and salt fluxes.

In addition to limiting the physics to 1-D mixing processes, the hybrid approach has the advantage that while MIZMAS provides the required forcing, PWP provides a more appropriate vertical resolution. MIZMAS has 40 ocean levels, and its resolution in the upper 77.5 m is 5 m, but we wish to resolve the mixed layer at a finer vertical resolution consistent with the 1-m vertical resolution of the observations obtained after smoothing 10-cm resolution raw data to reduce instrument noise. We are able to run the PWP at the same 1-m vertical resolution as our smoothed SIZRS observations.

MIZMAS' radiative fluxes and winds are forced by NCEP-R1, and the model assimilates sea ice concentration and drift to generate daily, grid-cell-averaged fluxes as well as ocean profiles. For this investigation, daily fields for ocean surface heat fluxes and stress are interpolated to 3-hour increments. Since MIZMAS' curvilinear grid resolution is near 0.4 degrees longitude and 0.04 degrees latitude in the SIZRS region, the model grid cells closest to

SIZRS AXCTD station coordinates are used for model forcing; forcing coordinates are chosen to fall at no farther than 0.25 degrees from the station sites. While the spatial and temporal resolutions of MIZMAS are not optimal for running our 3-hour model at one location, they represent the best available option for the continuous coverage and assimilated forcing needed to drive the PWP.

Initial temperature and salinity profiles are selected from SIZRS observations at our most often-sampled latitudes on 150°W: 72°N, 74°N, and 76°N. PWP runs are initialized with profiles that have no evidence of eddy activity and which have similarly clean profiles at the same station the following month. We define eddies as spikes in smoothed upper-ocean temperature or salinity at depths not associated with typical heat extrema (i.e., NSTM or Summer Pacific Water). These selection criteria allow for nineteen separate 1-month model runs starting at different months spanning the duration of the SIZRS program. These nineteen runs allow coverage of one month over multiple latitudes as well as the same month in multiple years. For example, there are model runs starting in June in all three years, as well as at multiple latitudes in each of those years (Figure 2.5a). The model is run at 3-hour time-steps and 1-m depth resolution over the top 100 m of the water column. Background diffusivity is set at 10^{-6} m^2s^{-1}, per Guthrie et al. (2013) and in agreement with SIZRS-deployed airborne expendable current profilers (Guthrie, personal communication), and optical attenuation coefficients are set to Jerlov oceanic Type II (Jerlov, 1976).

2.4.1 Taking Surface Fluxes From MIZMAS

While we use MIZMAS output to eliminate the need for an ice model on top of our PWP ocean, we adjust MIZMAS fluxes before feeding them into the PWP. These adjustments are

motivated by comparison of MIZMAS and initial PWP simulation results with SIZRS observations, but we have tried to limit them to accounting for possible biases in underlying reanalysis products and the inherent differences between the MIZMAS and PWP model paradigms.

The accuracy of MIZMAS temperature, salinity and other metrics are investigated in the model-observation synthesis portion of Zhang et al. (2016a), which uses multiple observational datasets to evaluate MIZMAS in the Beaufort Sea region. To focus here on the SIZ surface-layer properties, comparisons of MIZMAS simulated to SIZRS-observed month-to-month changes in upper-ocean temperature and salinity are illustrated in Figure 2.5b for the periods shown in Figure 2.5a. The average of the differences between MIZMAS and observed profiles over the nineteen 1-month periods are plotted with ±1 standard deviation.

Pertinent to the heat flux for PWP in the SIZRS periods, comparisons with SIZRS observed month-to-month temperatures (Figure 2.5b) indicate that MIZMAS predicts temperatures approximately 0.5°C cooler than observed at the surface. However, MIZMAS temperatures are 0.5°C warmer than observed at the bottom of the summer mixed layer around 20-m depth in the NSTM, whose formation is a primarily 1-D phenomenon (Steele et al., 2011) driven by radiative heating. With respect to salt flux, MIZMAS salinities are frequently over 1 psu higher than observations in the mixed layer in the months considered (Figure 2.5b), comparable to the mean salinity 0.65 psu bias in the upper 100 m found in the two profiles considered in Zhang et al. (2016a; see their Figure 4).

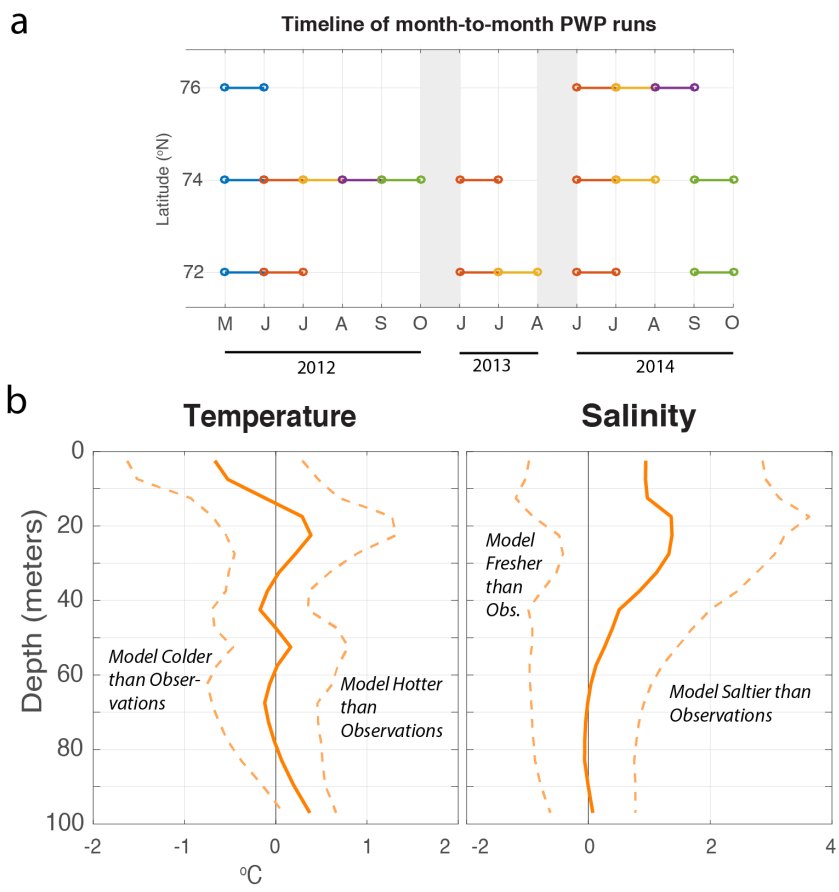

Figure 2.5 (a): Months, years, and latitudes for each of nineteen PWP runs on 150°W. **(b):** Mean temperature and salinity differences between MIZMAS and observations over all depths and all months, plotted with ±1 standard deviation (dashed lines).

2.4.2 Heat Flux

We seek refinements to MIZMAS derived flux inputs to PWP that are based on known biases in the reanalysis products that drive MIZMAS or clear requirements imposed by the inherent differences between PWP and MIZMAS. In the case of heat flux, we think the excess heat deep in the mixed layer and deficiency of temperature near the surface shown by MIZMAS (Figure 2.5b) are due to the combination of too much overall solar heating of the mixed layer and relaxation to a -1.8°C fixed freezing point temperature at the ocean's surface in the presence of ice (Zhang et al., 2016a). The former factor suggests adjustments to MIZMAS forcing that affect surface heating are necessary to the implementation of the 1-D PWP model.

The first adjustment is to remove an apparent bias due to the reanalysis input to MIZMAS, and then we subtract any ocean surface heating that goes directly to basal ice melt. The SIZRS timeline primarily covers the sea ice melt season, during which solar shortwave radiation exercises the principal control on bottom melting in areas of reduced ice coverage, and the role of longwave radiation is diminished (Perovich et al., 2011). Sensible and latent heat fluxes are much smaller than these radiative fluxes and so we treat them as low-order contributions and do not adjust those inputs to PWP. However, Lindsay et al. (2014) have shown that NCEP-R1 shortwave radiation is biased as much as 100 Wm^{-2} above observed values during the SIZRS sampling season. Using the average bias for the starting month of each PWP run from Lindsay et al. (2014—see their Figure 2), we subtract these values from our shortwave time series.

In addition to removing bias, we must account for the partition of ocean surface heat flux between basal ice melt and ocean heating. Sensitivity analyses of the PWP model in ice-covered conditions without this accounting produce surface warming up to 6°C above observations. Perovich et al. (2011) show that, across different ice concentrations and locations, 89% of shortwave radiation in the surface ocean typically goes to bottom melt of the overlying sea ice. MIZMAS, with its ice layer, accounts for this partition, but our ocean-only PWP cannot. Using the sea ice concentration (SIC) from MIZMAS, we can account both for the ice melt and for the shortwave bias in one equation:

$$SW=\left(100\%*\left(1\text{-}SIC\right)+ 11\%*SIC\right)*(SW_{reanalysis} - bias) \qquad (2.6)$$

This scaling results in a total reduction of shortwave input to the PWP ocean surface heating of 50%-80%, consistent with the range of reduction Perovich et al. (2011) observed in their analysis of a Beaufort Sea ice mass balance buoy. While this range is large and susceptible to error, it represents a best estimate of what a realistic shortwave input may be.

2.4.3 Momentum Flux

In our approach to momentum flux forcing for the PWP model, we do not have to modify MIZMAS surface stress for ice concentration, but similar to heat flux, we do scale surface stress inputs to account for reanalysis bias. During the SIZRS season floes move in near free drift, a condition in which internal ice stresses are negligible, so this ice regime has the potential to transfer most of the wind stress into the surface of the liquid ocean, without substantial change in magnitude (Martin et al., 2014). That is, if we consider the MIZMAS stress balance to be $\tau_{ocean} = \tau_{air} + F_i$ as stated in Martin et al. (2014), where the Coriolis contribution to this force balance is ignored and we consider the ice interaction force, F_i, as negligible in the MIZ per Hibler (1979), virtually all the momentum imparted by the wind to the ice or open ocean surface is ultimately transferred into the upper ocean. MIZMAS surface ocean stress includes stress from open water as well as ice-covered regions, and it accounts for the difference in momentum transfer over the two types of surface. For these reasons, we do not make stress adjustments based on ice concentration.

We do, however, scale the magnitude of the spatial-average surface stress. Initial sensitivity analyses of PWP suggested that the MIZMAS-derived surface stress was insufficient for PWP to replicate observed mixed-layer deepening. One reason for this is an underlying bias in wind speed used to drive MIZMAS. MIZMAS wind forcing is derived from NCEP-R1

(Kalnay et al., 1996), which can underestimate observed mean wind speeds by 25% (Lindsay et al., 2014). The PIOMAS and MIZMAS air-ice drag law is adjusted slightly to best match modeled ice velocity to drifting buoy ice velocities over the whole Arctic Ocean. This would account for bias in the reanalysis winds except in the SIZ where ice concentration can be low and the wind stress on open water accounts for a greater percentage of the aggregate momentum transfer. We assume that the mechanical forcing over the SIZ mix of open water and sea ice should scale with the square of wind speed. We therefore increase PWP surface stress forcing by scaling up MIZMAS aggregate ocean surface stresses by multiplying by $2.29 = 1/(1-0.25)^2$ to account for this wind speed bias. This adjustment increases PWP surface layer mixing and results in a mixed layer evolution that better agrees with observations.

2.4.4 Salt Flux

We derive the surface buoyancy, proportional to salt flux, for PWP from MIZMAS ice melt. Because sea ice is fresher than seawater (~10 psu bulk salinity for sea ice versus ~30 psu for seawater) sea ice melt produces negative salt flux and positive buoyancy flux downward. Conversely, sea ice formation produces salt and negative buoyancy flux downward. MIZMAS produces ice thickness estimates that agree with observations (Lindsay and Schweiger, 2015) and are consistent with sea ice changes over the summer in the Beaufort Sea. Therefore, to assess the month-to-month contributions of ice melt and formation to upper-ocean salinity, we calculate the freshwater flux as FWC change, in meters per second, due to area-averaged MIZMAS ice volume melt over each station's latitude. This calculation uses the satellite remote sensing derived sea ice concentration (see "SIZRS Observations") times the change in MIZMAS ice thickness, with an assumed sea ice salinity of 10 psu consistent with first-year ice. This method

allows us to calculate total freshwater drainage from the sea ice without having to parse the contributions of top and bottom ice melt. The method provides a higher-spatial resolution estimate of sea ice concentration than the MIZMAS cell-averaged value. This increased resolution is useful close to the ice edge. The change in ice cover from one month to the next is divided evenly over time-steps in the PWP run, resulting in a salt/freshwater flux that is constant over a month. While this smoothing does not capture the typically spatially varying nature of brine release from ice growth in leads (Nguyen et al., 2009), it can adequately describe the more spatially uniform release of freshwater due to seasonal melt.

2.5 Results from Observations and the PWP model of the SIZ

Examples of month-to-month transitions in upper ocean observed and simulated changes (Figure 2.6) indicate that the PWP model and observations behave qualitatively as we expect during summer and winter periods of ice melt and formation. After one month's observation is used to initialize the PWP, the model's output can be easily compared to observations from the following month in the same location. Example month-to-month PWP simulation results for early summer melt (Figure 2.6a) and late summer/overwinter freeze-up (Figure 2.6b) illustrate that the model can at least qualitatively capture the range of mixed layer behaviors we expect to see over the SIZRS season. In early summer, for example June to July 2012 (Figure 2.6a), the surface meltwater flux downward increases stratification that limits deep turbulent momentum transfer and results in development of a freshened shallow mixed layer, 12 m deep in the observations and 8 m deep in the PWP simulation. This mixed layer freshens by about 2 psu in both observations and PWP simulations. Solar heating warms the shallow mixed layer by an observed 0.75°C. The modeled upper ocean warms in the new mixed layer although less than

observed, but as in the observations, the modeled warming extends to a some extent down to 25 m, suggesting some radiant energy penetrates deeper than mechanical mixing.

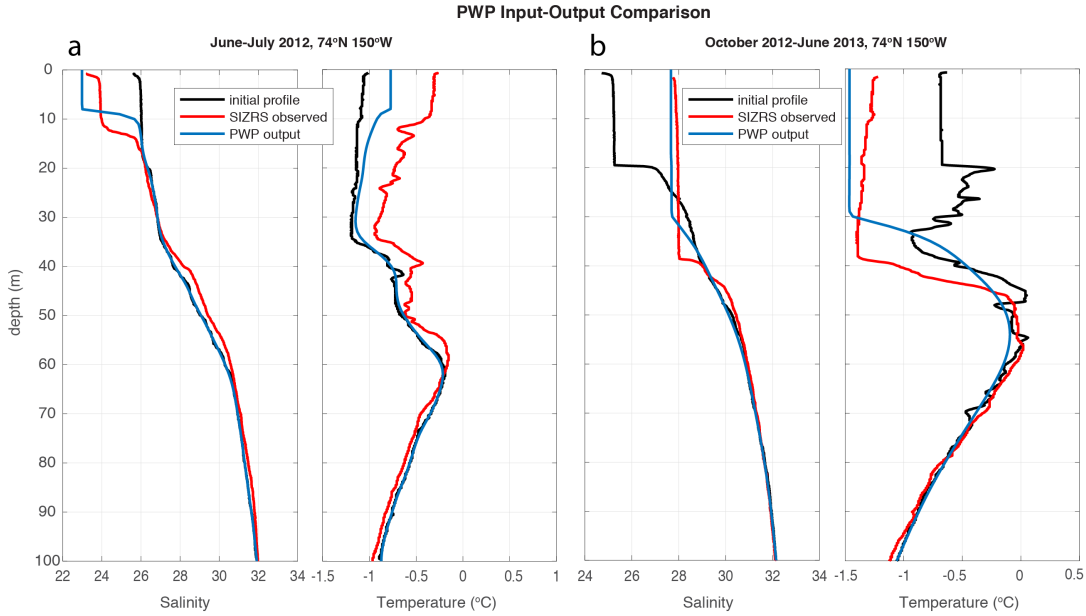

Figure 2.6 Examples of the early summer shoaling **(a)** and overwinter deepening **(b)** of the mixed layer in month-to-month PWP runs from June to July 2012 and October 2012-June 2013 at 74°N, 150°W. Black lines indicate the observed profiles used to initialize the PWP, and blue lines the PWP output. Red lines are the observed profiles contemporaneous to the blue lines.

The opposite is true of an overwinter run from October 2012-June 2013: downward freshwater (buoyancy) flux transitions from positive to negative resulting in near neutral to unstable stratification for which surface stress causes deepening of the mixed layer to 38 m (observed) and 30 m (PWP) from its shallow, 20-m late summer state (Figure 2.6b). The mixed layer also becomes almost 3 psu saltier in both the observations and PWP simulation as sea ice forms. Driven by wintertime cooling of the surface ocean, the observed and modeled mixed layer temperatures decrease by about 0.75°C to near the salinity determined freezing point.

Considering all 19 month-to-month PWP simulations, the agreement with observations varies, but as indicated by the ensemble averages of the differences between PWP and observations, average agreement is reasonably good (Figure 2.7). Over the upper 100 m of the water column the ensemble average bias of the PWP temperature changes relative to the observed temperature changes is -0.05°C and the standard deviation, averaged over depth, of model biases relative to observations is 0.38°C (Figure 2.7a). The magnitude of this standard deviation in the upper 20 m is comparable in magnitude to the temperature variability observed south of the ice edge (Figure 2.2b). The maximum ensemble average bias is 0.34°C in the upper 5 m. Similarly, over the upper 100 m, the ensemble average bias of the PWP month-to-month salinity changes relative to the observed (Figure 2.7b) is -0.08 psu and the standard deviation averaged over depth is 0.43 psu. The maximum ensemble average bias is -0.73 psu in the upper 5 m.

These PWP simulated biases relative to observed month-to-month changes are smaller than the departures of the MIZMAS temperature and salinity changes from the observed month-to-month changes. In the sense that MIZMAS is a simulation over a longer period of time than the month-to-month PWP simulations, this comparison is a little unfair. However, as discussed above, the MIZMAS temperature and salinity biases are likely partly due to biases in the NCEP reanalyses used to drive MIZMAS. Indeed if we drive PWP with MIZMAS forcing but no

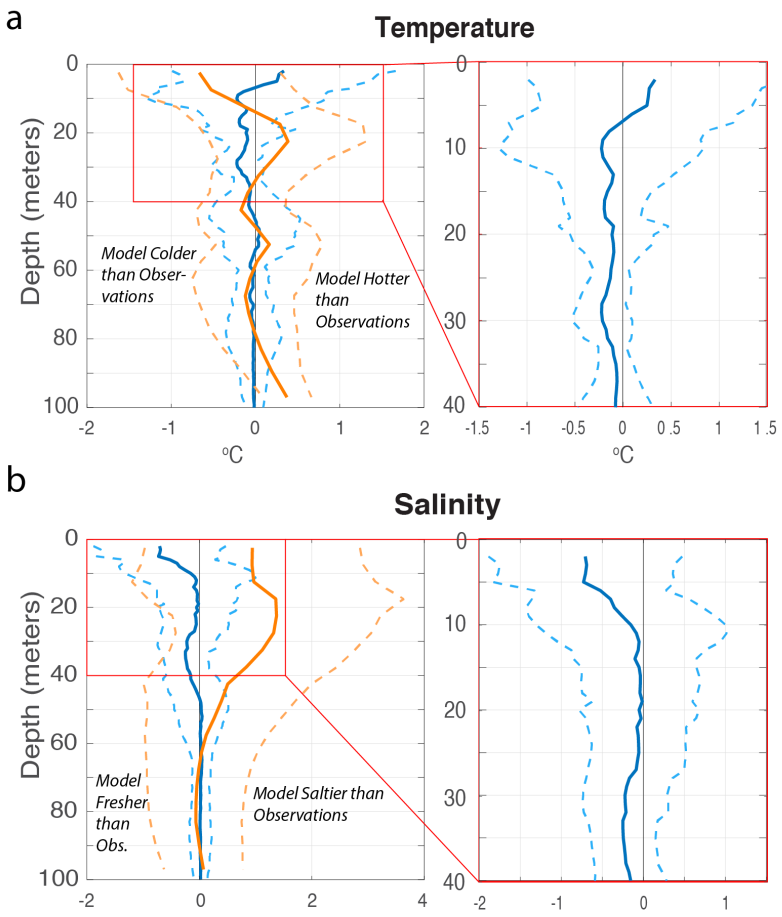

Figure 2.7 Mean temperature **(a)** and salinity **(b)** differences between PWP and observations (blue) and MIZMAS and observations (orange) over all depths and all months, plotted with ±1 standard deviation (dashed lines). The top 40 m of the PWP differences are shown in the red boxes.

correction for NCEP biases (Figure 2.8a), PWP, like MIZMAS, ends up with too much heat (2°-6°C) in the upper ocean (in MIZMAS this effect is reduced by fixing the temperature to -1.8°C at the surface). Similarly, without correcting upward the input forcing of stress, the PWP near-surface stratification is higher than observed; salinities are too low near the surface and too high deeper in the mixed layer (Figure 2.8b).

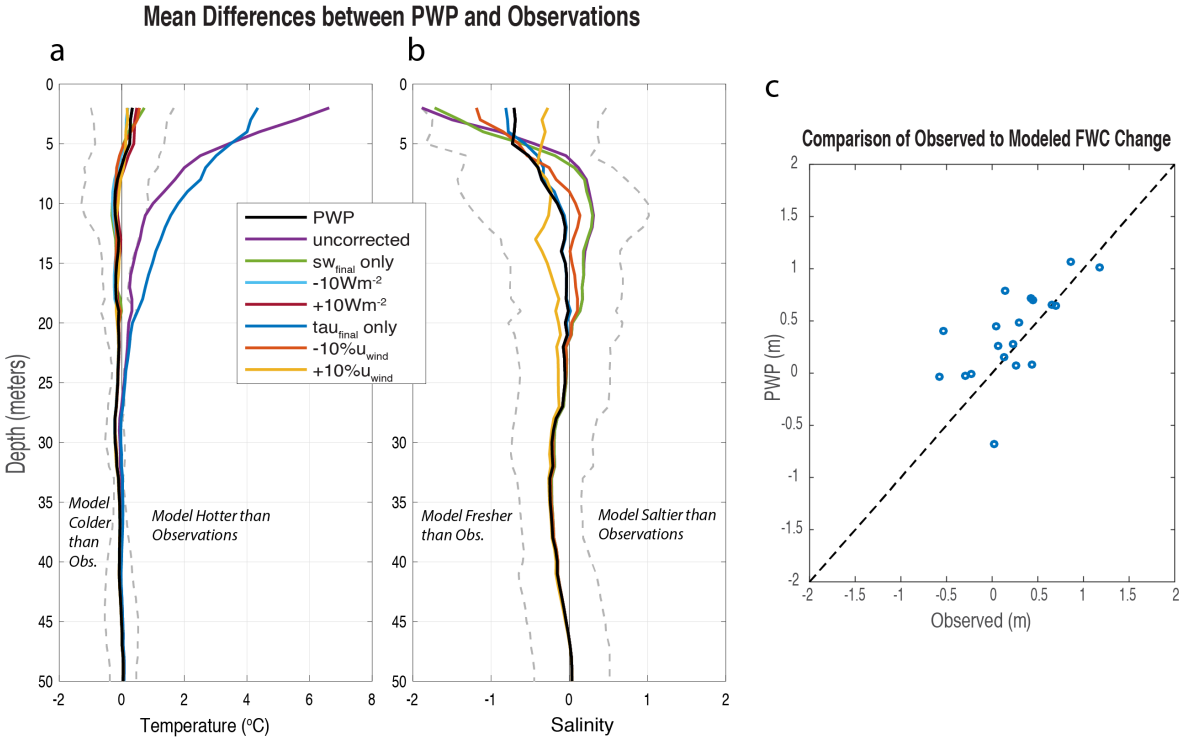

Figure 2.8 (a-b): Mean temperature and salinity differences between PWP and observations over all depths and all runs with adjustment of shortwave and surface stress forcing. Eight different scenarios are considered: one in which no changes to forcing are made, one in which only the shortwave input is changed, one in which only the surface stress is changed, and 2 each where the bias adjustments based on Lindsay et al. (2014) are increased or decreased about the final value for one forcing while the other is held constant at its final value. The eighth scenario is the final PWP output, flanked by one standard deviation (dashed lines). **(c):** Comparison of freshwater content change relative to 34.8 in PWP simulations and SIZRS observations. Change in meters is shown against a 1:1 line, with the majority of the PWP FWC change slightly in excess of that found in observations. These changes are consistent with earlier estimates of the FWC of sea ice and the underlying oceanic change. Because the ratio of its mean FWC magnitude to that of observations is approximately 1.13, the excess freshwater from the PWP is likely advected away.

In addition to the PWP runs with the corrected MIZMAS shortwave heating, stress, and freshwater flux, we have run several sensitivity studies to demonstrate the relative importance of shortwave heating and surface stress in the PWP implementation (Figures 2.8a & b). Eight different ensembles of 19 runs each are conducted in addition to the primary PWP ensemble with corrected MIZMAS-based forcing. The first run makes no corrections to MIZMAS shortwave or stress inputs. As discussed above, this arguably yields results most comparable to MIZMAS because the fluxes are not adjusted for reanalysis biases. In the second example only the shortwave input is corrected, and in the third only the surface stress is corrected. Without any corrections to forcing (including both the scaling of shortwave heat and the removal of bias), PWP yields a surface temperature bias of +6°C (Figure 2.8a) and a salinity bias of -1.7 psu (Figure 2.8b). Changing only the shortwave input makes the PWP temperature profiles more closely match SIZRS observations, but it results in an average salinity bias of -1.5 psu at the surface (Figure 2.8b). Likewise, changing only surface stress yields a salinity profile close to observations but a temperature bias of +4°C (Figure 2.8a).

To understand the interplay between the two primary forcing adjustments, we include two runs in which the shortwave forcing has been varied while the surface stress input to PWP is consistent with the primary PWP ensemble, and two runs in which the surface stress has been changed while the shortwave forcing correction remains the same. Adjustments of shortwave bias by 10 Wm^{-2} about the corrected value result in little change from the primary result, whereas adjustments of surface stress by 10% result in changes in near-surface stratification (Figure 2.8a & b). In each case, these changes are small relative to the primary corrections, reinforcing the physical assumptions that led to those corrections.

2.6 Vertical Mixing versus Advection in the SIZ

With respect to the question of the relative roles of vertical mixing versus advection, perhaps the most telling result of these analyses is the slight negative bias in average PWP salinity month-to-month change (Figure 2.7b) and associated total fresh water content (FWC) changes relative to observed changes. Arguably the negative bias in observed salinity change is at least partly due to advection not represented in the model, and the ratio of FWC bias to total FWC change is a potential measure of advection as a fraction of the total change attributable to mixing.

As shown in Figure 2.8c, the PWP model is able to reproduce the freshwater content change integrated between 2 m and 20 m depth. The 2-m upper limit eliminates the effects on salinity measurements of any AXCTD sensor start transients. As in our sample calculation at the beginning of this manuscript, a reference salinity of 34.8 is used for freshwater content calculations, following *Carmack et al.* (2008) and *Aagaard & Carmack* (1989). Estimated errors from this FWC calculation are on the order of 10^{-4} m..

The ratio of the mean magnitudes of FWC change in the PWP simulations to FWC changes in the observations is approximately 1.13, with a standard deviation in each of 0.3 m, suggesting 1-D vertical mixing of sea ice melt can account for about 87% of upper ocean freshening in the SIZ with on the order of 10% of freshwater being advected away. This result is similar to the back of the envelope calculation based on observations alone, 81% to 100% and the portion of salinity variability across the Beaufort Gyre not associated with variations in gyre circulation, 77% (e.g., correlated with the AO).

2.7 Inter-Seasonal Robustness of the PWP and the Wintertime Role of Horizontal Advection

Although it is not the focus of this work, an important question is the role of 1-D mixing to wintertime evolution of the Beaufort Sea SIZ region. Does the formation of seasonal ice cover and the associated negative freshwater flux drive upper wintertime ocean changes through vertical mixing to the same degree that melting and positive freshwater flux does in the summer? We explore this question by simulating the transition from fall to late spring using our PWP driven model by growth of the ice cover.

We have conducted runs of the PWP from October 2012 to June 2013 and August 2013 to June 2014, at 72°N, 74°N, and 76°N on 150°W (Figure 2.9). Generally, model-simulated mixed layer temperatures are within a quarter degree Celsius of observations, and model-simulated salinities are within less than 1 psu (Figure 2.9). However, in the case of the 2013-2014 run, the PWP predicts a mixed layer fresher than observations by 2 psu at 76°N.

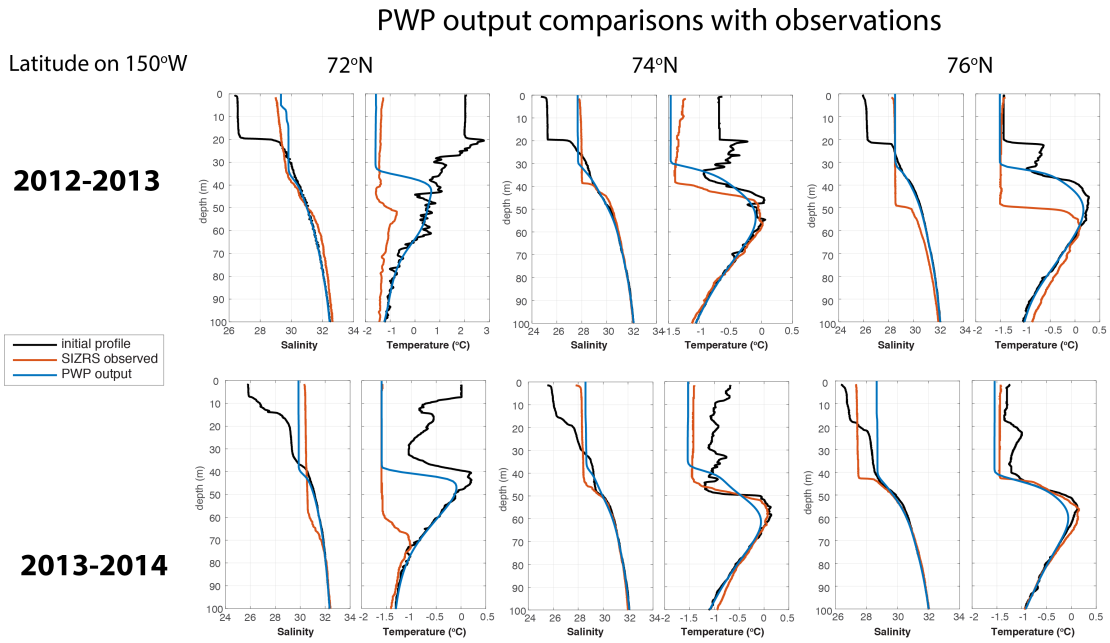

Figure 2.9 PWP runs on three latitudes from October 2012 to June 2013 and August 2013 to June 2014. Black lines are the profiles of temperature and salinity used to initialize the PWP run, and blue lines are the PWP output. Red lines are the observations contemporaneous with the end of the PWP run; the success of the PWP is determined by the resemblance of the blue lines to the red.

Considering the variances of the difference between simulated and observed over-winter salinity changes, we find that the change in salinity shown by the model accounts for >95% of the variance in the observed over-winter salinity changes (Table 2.2). While the model does closely approximate mixed layer depths in the majority of runs, in others it can underestimate the depth by up to 15 m. This difference may be due to the temporal resolution of the PWP surface stress forcing. The depth of wintertime mixing tends to scale with u_*/f, where u_* is the friction velocity and f is the Coriolis parameter (e.g., McPhee, 2006). The surface stress forcing interpolated from daily MIZMAS surface fluxes likely does not capture the peak stresses and maximum mixed layer deepening associated with winter high-wind events. Indeed, the SIZRS scenario differs from that described by Fer et al. (2017) in their 1-D analysis of wintertime change in the Nansen Basin. They find that entrainment from below the mixed-layer, rather than brine rejection, dominated the

salinity changes therein. This contrast likely reflects the difference between the Eurasian Basin SIZ characterized by outflowing ice underlain by inflowing warm salty Atlantic Water (e.g., Untersteiner, 1988) versus the Beaufort Sea SIZ characterized by ice and a relatively stable surface layer trapped in an anticyclonic gyre circulation and isolated by a cold halocline from Atlantic Water heat below.

Table 2.2 The ratio $1 - \frac{var(\Delta S_{observed} - \Delta S_{PWP})}{var(\Delta S_{observed})}$, which describes the fraction of variance in SIZRS observed monthly salinity change is accounted for by the PWP. Shown are values for two different depth ranges (0 to 40 m and 0 to 50 m, chosen because of typical winter mixed-layer depth ranges) for each latitude at which the model was run on 150°W.

		72°N	**74°N**	**76°N**
Upper 40 m	*2012-2013*	0.9911	0.9502	0.9367
	2013-2014	0.9996	0.9960	0.9994
Upper 50 m	*2012-2013*	0.9868	0.9486	0.8430
	2013-2014	0.9607	0.9750	0.6746

Our salinity results indicate that the majority of freshwater content change in the upper ocean in the Beaufort Sea comes from vertical fluxes that originate with local sea ice melting and formation, suggesting that the contributions of freshwater surface horizontal advection are small relative to vertical 1-D processes. To independently estimate the contributions of horizontal advection to surface freshwater distribution, we have calculated advection in MIZMAS using the dot product of velocities and smoothed salinity gradients gridded onto a rectangular, 0.2-degree longitude by 0.1-degree latitude matrix, bounded by 155°W, 135°W, 80°N, and 70°N. We use this advective salt flux to calculate convergence at each gridpoint (in $kgm^{-3}s^{-1}$), in order to estimate a cumulative salinity change over each SIZRS season.

We find the MIZMAS-derived horizontal salt flux convergence to be O[10^{-8}] to O[10^{-9}] $kgm^{-3}s^{-1}$ averaged on 150°W between 72°N and 76°N. When we compare the advective change to that from vertical freshwater fluxes, the expected change in salt content per cubic meter, O[10^{-1}] kg, is approximately one order of magnitude smaller than that expected from melting one cubic meter of ice, O[10^{0}] kg, over six months. For example, advection of 2 x 10^{-9} $kgm^{-3}s^{-1}$ yields 0.31 kg of salt per cubic meter in 6 months. This translates roughly to a salinity change of 0.3, 20% of the surface salinity change from June to September 2014 at 74°N 150°W of approximately 1.5. These results are consistent with the 10%-20% residual role for advection estimated from observations and comparisons of PWP results with observations.

2.8 Discussion

Observations in the Beaufort Sea SIZ indicate a characteristic pattern of upper ocean freshening aligned with the retreating ice edge position. This behavior can be seen in the SIZRS data at a basin scale—melt occurs everywhere, and the resulting freshening is apparent throughout the gyre but most prominently south of the ice edge where ice has completely disappeared (Figure 2.1) and associated cumulative surface freshwater flux is greatest. The observed changes are consistent with vertical mixing of sea ice meltwater into the upper ocean. The PWP model was developed and run to test this assertion by seeing if the changes in upper ocean temperature as well as salinity structure could be simulated by a 1-D mixing model driven by realistic surface mechanical and thermal forcing. The conclusion is a qualified yes; PWP simulations produce salinity and temperature changes that account for about 90% of the observed month-to-month changes in the Beaufort Sea SIZ.

The success of the 1-D PWP simulations in the Beaufort Sea indicates that the alignment of the freshening pattern with the ice edge position is because salt distribution is almost totally dependent on the amount of local sea ice melt. As a consequence of complete ice melt south of the sea ice edge, the meltwater left behind as the edge retreats remains at roughly the same radial position instead of being gathered to the center of the gyre. On an inter-seasonal time scale, from fall to spring, lateral advection of freshwater in the gyre interior is also small relative to surface vertical fluxes. Observed bulk changes in ice and ocean properties, PWP simulations, and estimates of Ekman convergence suggest 1-D mixing of ice meltwater is responsible for about 77%-89% of the upper ocean salinity changes in this region.

This surface behavior overlies long-term changes in the structure of the Beaufort Gyre, both in its intensification and in its response to the AO. In the past, freshening of the gyre has been associated with convergent Ekman transport of fresh surface water (Proshutinsky et al., 2002; Proshutinsky et al., 2009; Giles et al., 2012). These authors and others attribute freshening of the Beaufort Sea to increased anticyclonic-wind-driven spin-up of the Beaufort Gyre. However, Zhang et al. (2016a) show that the Beaufort Gyre has stabilized at a high level since 2008, a timeframe that encompasses our 2012-2014 SIZRS campaigns. Similarly, McPhee (2013) indicates that after 2008, ocean geostrophic surface currents were moving at speeds comparable to those of the overlying ice. This stabilization is consistent with our results. In summer and fall of 2012-2014 Ekman convergence appears to have small influence and the seasonal evolution of freshwater distribution is controlled by 1-D mixing processes.

Furthermore, the apparent relationship between Beaufort Gyre strength and hemispheric atmospheric forcing in 2012-2014 is not what we had expected. The classical assumption is that because gyre spin-up and freshwater content increases occur under anti-cyclonic forcing of the

Beaufort High, the cyclonic influence of a positive AO (Rigor et al, 2002) would cause gyre weakening and a decrease in freshwater content (Proshutinsky et al., 2002). However, Morison et al. (2012) have argued that the Canada Basin freshens under a high AO state because of advection of Eurasian runoff into halocline of the western Arctic Ocean. Our SIZRS 2012-2014 results make an even stronger connection. These results associate increased AO with increased doming of the Beaufort Gyre. We have shown that, in addition to bottom pressure and isopycnal tilt, on sub-annual timescales the AO index acts as a workable proxy for gyre strength when an appropriate lag between atmospheric forcing and oceanic action is considered.

We find that in 2012-2014 the seasonal behavior of the surface ocean in the Beaufort Sea SIZ area is dominated by vertical processes as the sea ice cover recedes. It is clear from our SIZRS observations that the seasonal sea ice edge plays a significant and similar role in setting surface ocean properties at the SIZ scale, independent of how far north this edge lies. Through a modeling investigation, we argue that observed surface freshening in this area may be described as a primarily vertical process, dominating advective influence in the upper 20 m of the study region. The reduced influence of the advective effects may be because by 2012 the ocean had spun up to the point where average surface geostrophic velocities are roughly equal to average sea ice velocities (McPhee, 2013). As a consequence, surface stress decreases in magnitude and potentially reverses direction, and the typical average Ekman convergence is small. However, in this semi-equilibrated state, a small increase in the AO at monthly timescales resulting in strengthened northeastward wind stress on the northwest part of the Beaufort Sea not sampled by our SIZRS surveys may cause enough Ekman pumping of near-surface water towards the center of the Beaufort Gyre to increase its intensity.

Chapter 3: *Large-scale horizontal dynamic processes: basin FWC and equilibration.*

An edited version of this chapter was published by AGU. Copyright (2018) American Geophysical Union: Dewey, S., Morison, J., Kwok, R., Dickinson, S., Morison, D. & Andersen, R., 2018. Arctic ice-ocean coupling and gyre equilibration observed with remote sensing. *Geophysical Research Letters,* **45**. doi:10.1002/2017GL076229

3.1 Background

The correspondence among wind, ice drift, and Arctic Ocean circulation have been studied since Nansen's observation that ice moves at 20° to the right of surface wind and at 2% of the wind speed [*Nansen*, 1902]. *Thorndike and Colony* [1982, hereafter referred to as TC82] regress winds and buoy-derived ice velocity and confirm Nansen's rule of thumb with respect to the ice velocity's variance. This result can lead to the idealization that ice motion is solely dependent on wind [e.g., *Ma et al.,* 2017]. However, TC82 also find it impossible to distinguish the forcing of mean ice velocities between wind-forced and ocean-forced. Indeed, Arctic sea ice velocity shows a strong similarity to geostrophic ocean surface velocity from ICESat dynamic ocean topography (DOT) in 2004-2009 [*Morison et al.*, 2012], implying that the ocean forcing plays a significant role in driving the ice.

Kwok et al. [2013] perform an updated regression analysis similar to TC82 but informed by present Arctic ice conditions and remote sensing data. The pattern of residual ice velocity that they attribute to the ocean strongly resembles the ocean velocity from ICESat DOT. Moreover, they find that for the most part ocean speeds exceed ice speeds, suggesting the ocean is driving the ice rather than acting as a passive drag on wind-driven motion.

The tendency for the ocean to drive the ice is apparent, and perhaps nowhere more important than, in the Beaufort Sea. The Beaufort Gyre is one of the dominant features of the mean Arctic Ocean circulation. Driven by the Beaufort High in atmospheric pressure, it flows anticyclonically over the Canada Basin, and is a convergence zone boasting the highest sea

surface height [*Kwok and Morison,* 2011] and freshwater content in the Arctic Ocean [*Serreze et al.,* 2006; *Carmack et al.,* 2008]. Locally, this freshwater influences stratification and sea ice formation; were it to exit the Arctic Ocean, it could potentially disrupt deep water formation, the ocean's meridional overturning circulation, and global climate [*Proshutinsky and Johnson,* 1997; *Aagaard and Carmack,* 1989; *Proshutinsky et al.*, 2002; *Koenigk et al.,* 2007; *Jahn & Holland*, 2013; *Sévellec et al.*, 2017].

The Beaufort Sea has been identified as a region of the largest summer sea ice areal decline in the past decade [*Comiso et al.,* 2008], and has experienced the greatest recent loss in multiyear sea ice [*Maslanik et al,* 2011]. Given its role in freshwater storage and the rapidly diminishing ice cover, the Beaufort Gyre has garnered much attention as a nexus of change, especially with respect to its recent accumulation of momentum.

Proshutinsky and Johnson [1997] propose two regimes of Arctic Ocean circulation based on the strength of the sea surface height gradient driving the Beaufort Gyre. In the anticyclonic (cyclonic) phase, the gyre intensifies (weakens) as surface height gradients increase (decrease) due to enhanced (reduced) Ekman transport convergence driven by more (less) negative surface stress curl under a strengthened (weakened) Beaufort High. Expanding on this notion, *Proshutinsky et al.* [2009] emphasize the role of the anticyclonic phase in accumulating freshwater, relating a maximum of freshwater accumulation to maximally negative wind stress curl.

In the mid 2000s the Beaufort Gyre intensified and accumulated freshwater [*McPhee et al.,* 2009; *Proshutinsky et al.,* 2009]. The intensification was manifest in satellite altimetry measurements of increased doming of the gyre [*Morison et al.,* 2012; *Giles et al.,* 2012]. Objective analysis of a broad collection of hydrography [*Rabe et al.,* 2011], corroborates the

accumulation of freshwater in the gyre, as does freshwater content estimated from the trends in satellite-derived sea surface height [*Giles et al.*, 2012] and the difference between this height and ocean bottom pressure [*Morison et al.,* 2012].

The doming of the Beaufort Gyre is driven by convergence of Ekman transport, or Ekman pumping, in which the rate of doming is related to negative surface stress curl. Under the persistent negative stress curl of the Beaufort High, doming should continue to increase. However, model and observational evidence has shown that since about 2009, the Beaufort Gyre has stabilized following the period of spin-up [*Zhang et al.,* 2016a; *Krishfield et al.,* 2014; *Petty et al.,* 2016; *Armitage et al.,* 2017]. Freshwater content of the Beaufort Gyre has seemingly plateaued [*Zhang et al.,* 2016a; *Krishfield et al.,* 2014], indicating that despite its persistently anticyclonic wind forcing, the gyre is no longer accumulating more freshwater. One explanation for this equilibration of the gyre is horizontal eddy diffusion of momentum in the ocean [*Manucharyan and Spall*, 2016; *Manucharyan et al.*, 2016]. Eddy diffusion that exports freshwater and momentum tends to balance halocline deepening due to cyclonic surface forcing and is thus a contributor to long-term stability. Were this the only stabilization mechanism, the ice velocity would always exceed geostrophic water velocity. Instead, the recent stabilization of the Beaufort Gyre has been associated with geostrophic water velocity exceeding ice velocity.

Similar to the finding of *Kwok et al.* [2013], as part of the Beaufort Gyre spin-up, *McPhee* [2013] and *Armitage et al.* [2017] show that geostrophic ocean currents in the Canada Basin have increased to rival and sometimes exceed ice drift speeds. It is the relative velocity of the ice and ocean that determines the strength and direction of ice-ocean surface stress. Therefore we argue that in the presence of an ice cover with internal ice stress, which dissipatively retards ice motion, the difference in ice and ocean velocities is a key agent in the observed gyre

stabilization because of changing ice-ocean stress [*Kwok and Morison*, 2017]. Specifically, where the ice is slowed by internal ice stress and the ocean moves faster than the ice, the sign of the ice-ocean stress and associated Ekman pumping are reversed, and the gyre dome decreases—even as the sign of average wind stress curl may predict convergence.

Several model studies have looked at the change in ocean surface stress under recent, increasingly ice-free conditions [*Zhang et al*., 2012; *Martin et al.* 2014; *Martin et al.*, 2016; *Tsamados et al.*, 2014]. This paper constitutes a first observational evaluation of the Ekman pumping-internal ice stress dissipation and its influence on gyre stabilization. Key advances in this analysis are the use of satellite-derived geostrophic velocities in the calculation of ice-ocean stress, which previous studies [*Petty* et al., 2016; *Timmermans et al.,* 2014; *Yang*, 2009, *Ma et al*., 2017] have neglected, and the finding that for present conditions the Ekman pumping ice-ocean stress dissipation is likely at least twice as great as ocean eddy dissipation of gyre energy.

3.2 Coupling of Ice and Ocean Velocity

To understand the fundamental connection between ice motion ($\bar{V}$) and geostrophic water velocity ($\bar{V}_g$), we consider the quasi-steady-state horizontal force balance for sea ice with complex velocity $\bar{V} = u + iv$, draft *D,* surface ocean density ρ_0, and horizontal length scale *L*. As discussed in *McPhee* [1980, 1982], this balance is one between the Coriolis effect ($if\left(\bar{V} - \bar{V}_g\right)$), air-ice stress ($\bar{\tau}_{ai}$), ice-ocean stress ($\bar{\tau}_{io}$), and horizontal internal ice stress $\bar{\tau}_{ii}$, a result of interaction of the ice floes:

$$if\left(\bar{V} - \bar{V}_g\right) = \frac{1}{\rho_0 D}\left(\bar{\tau}_{ai} - \bar{\tau}_{io}\right) - \frac{1}{\rho_0 L}\bar{\tau}_{ii} \qquad (3.1)$$

$\bar{\tau}_{ai}$ is the forcing solely dependent on the square of wind velocity because wind speed is so much larger than typical ice velocities. For the purpose of scaling, $\bar{\tau}_{ii}$ is an idealized representation of internal ice stress. At horizontal scales where the force exerted by internal ice stress is comparable to that exerted by surface stresses, $\bar{\tau}_{ii}/L$ is comparable to $\bar{\tau}_{ai}/D$. It can be considered a dissipative force dependent on horizontal gradients in ice velocity, and is difficult to measure directly.

$\bar{V}_g$ is the surface geostrophic water velocity forced by the horizontal gradient in dynamic ocean topography, η:

$$\bar{V}_g = u_g + iv_g = i\frac{g}{f}\left(\frac{\partial \eta}{\partial x} + i\frac{\partial \eta}{\partial y}\right) \qquad (3.2)$$

$\bar{V}_g$ appears in (1) as an expression of the force exerted on the ice by the gradient in η. The ice-ocean stress, $\bar{\tau}_{io}$, is related by the quadratic geostrophic drag law to the difference between ice velocity and $\bar{V}_g$ [*McPhee*, 2008]. Consequently, (1) indicates that whenever wind stress forcing is small and horizontal scales are large enough or the ice cover thin enough to reduce internal ice stress, sea ice velocities are damped to the geostrophic water velocity. This explains in part the similarity of large-scale ice velocity and Arctic Ocean surface circulation [*Kwok et al.*, 2013]. However, ice velocity is also coupled to the geostrophic water velocity (or sea surface tilt) indirectly through Ekman transport convergence (Ekman pumping):

$$W_{Ek} = \nabla \times \left(\frac{\tau}{\rho_0 f} \right) \qquad (3.3)$$

$$\tau = \alpha \tau_{io} + \left(1 - \alpha\right) \tau_{ao} \qquad (3.4)$$

where W_{Ek} is the vertical velocity difference between the surface and the bottom of the ocean planetary boundary layer due to Ekman transport convergence, α is the ice concentration, and τ_{ao} is the wind stress on open water areas.

The relative degree to which W_{Ek} affects the surface height, η, and the isopycnals below the mixed layer depend on the time and space scales of the forcing. For Arctic latitudes at basin length scales and time-scales shorter than seasonal to a year, the ocean response is largely barotropic [*Vinogradova et al.*, 2007] so that much of W_{Ek} can result in vertical velocity of the surface, $\dot{\eta}$. At shorter space-scales and longer time-scales baroclinic adjustment occurs so that a larger fraction of W_{Ek} goes into displacing isopycnals. In any event, negative (positive) stress curl results in upward (downward) $\dot{\eta}$ and progressive doming (dishing) of the surface.

At lower latitudes where the beta effect (variation of *f* with latitude) is strong, the progressive change in the surface height and isopycnal depth are dissipated by generation of Rossby waves. In an ice-free Arctic Ocean, where beta is small and this dissipation mechanism is essentially unavailable, doming and pycnocline displacements would likely increase until limited by interaction with topography or baroclinic instability. However, under an ice cover this

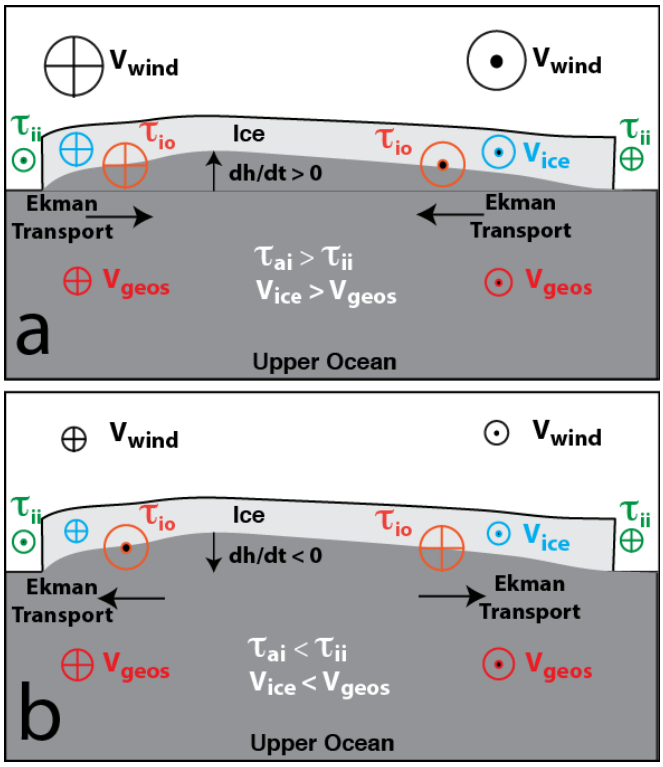

Figure 3.1 Illustration of Ekman pumping-internal stress feedback for gyre equilibration [adapted from *Kwok & Morison*, 2017]. On top, the condition in which the wind stress dominates the internal ice stress, and ice velocity is greater than the surface geostrophic water velocity. In this case, Ekman convergence increases the surface tilt (doming) and this in turn increases the surface geostrophic velocity. On the bottom, the condition in which internal ice stress is greater than the wind stress, and the surface geostrophic water velocity is greater than the ice velocity. In this case, the ice-ocean stress leads to divergence (less doming), and with this decrease in tilt, decreases the ice and ocean geostrophic velocities.

progressive doming is limited because it increases the associated geostrophic water velocity while internal ice stress retards ice velocity. This proceeds until the geostrophic water exceeds ice velocity so that ice ocean stress, stress curl and W_{Ek} reverse, doming stops, and Ekman pumping reverses (Figure 3.1) [*Kwok and Morison*, 2017] until ice velocity and the geostrophic water velocity equilibrate.

Ultimately, the Beaufort Gyre is subject to a three-way balance between spin-up, the Ekman pumping - internal ice stress feedback, and the generation of eddy flux [*Meneghello et al.*, 2017] by baroclinic instability. Our observations indicate that with the present ice cover, the Ekman pumping-internal ice stress feedback contributes more to gyre stabilization than eddy flux.

3.3 Methods and Data

Using constitutive relationships for the total ice-ocean and air-ocean stresses (Eqs. 3.5 & 3.6), we then scale the stresses by interpolated ERA-Interim ice concentration (*Yang*, 2009) to yield surface stress at each point on a 25-km equal area polar stereographic grid (Eq. 3.4). Here we refer to doming of the surface and downward motion of the pycnocline as downwelling and downward surface motion with upward motion of the pycnocline as upwelling. The curl of $\boldsymbol{\tau}$ is then used to diagnose downwelling (upwelling), or freshwater accumulation (release) conditions (Eq. 3.3).

$$\vec{\tau}_{io} = \rho_o |C_{iw}| \mathrm{e}^{\mathrm{i}\beta} (\vec{u}_i - \vec{u}_g) \left| \vec{u}_i - \vec{u}_g \right| \tag{3.5}$$

$$\vec{\tau}_{ao} = C_d \rho_a \vec{U}_{10} \left| \vec{U}_{10} \right| \tag{3.6}$$

In these equations, ρ_o and ρ_a represent the surface densities of water and air, respectively. $\vec{u}_i$, $\vec{u}_g$, and $\vec{U}_{10}$ are the velocities of sea ice, ocean geostrophic surface velocity, and 10-m winds. C_d is an air-ocean drag coefficient, here taken as 1.25×10^{-3}. C_{iw} and β are the drag coefficient and the turning angle of the ocean geostrophic drag law for which we use the values of 5.5×10^{-3} and 23° [*McPhee*, 1980]. With a changing ice cover, there has been much effort to

update these values [*Cole et al.* 2017; *Cole et al.*, 2014; *McPhee* 2012; and *Lu et al.,* 2011], though a brief sensitivity analysis of β showed negligible changes in the magnitude of W_{Ek}.

Dynamic Ocean Topography (DOT), in meters, is calculated from the Synthetic Aperture Radar Interferometric Radar ALtimeter (SIRAL) on the European Space Agency's CryoSat-2 (CS-2) satellite [*Kwok & Morison,* 2016]. The DOT data used here are two-month averages from April 2011-April 2015, a period shown by the model of *Zhang et al.* [2016a] and the DOT observations of *Armitage et al.* [2017] to be one of stabilization of the Beaufort Gyre. The data are Kriged to a grid, smoothed with a 250-km diameter Gaussian filter per *McAdoo et al.* [2013], and their gradients used to calculate ocean geostrophic velocities. Ocean surface density is interpolated to each 25-km grid point from the PHC climatology [*Steele et al.*, 2001], though results are not sensitive to this choice of climatology. Air density is taken as the canonical value of $1.25 kgm^{-3}$.

We use monthly, optimally interpolated, satellite-derived ice velocities (as described in *Kwok et al.* [2013], with a per-vector uncertainty of $2 cms^{-1}$). These agree with IABP buoy-derived velocities [Rigor, personal communication 2017]. The buoy-satellite hybrid velocities of NSIDC [*Tschudi et al.,* 2016] were not used because they are lower than our velocities and buoy velocities [*Sumata et al.*, 2014, 2015], and thus exaggerate any ocean velocity exceedance of ice velocity. Also, their hybridization creates artificial divergence in the velocity field [*Szanyi et al.*, 2016].

Monthly 10-meter wind velocities and sea ice concentration come from ERA-Interim reanalysis [*Dee et al.*, 2011], optimal both for spatial resolution (nominally 0.75° x 0.75°) and agreement with observations [*Lindsay et al.*, 2014].

3.4 Sea Ice and Geostrophic Ocean Velocities

Our observed DOT and derived geostrophic velocities confirm that the ocean rivals the sea ice in speed. In order to present areal or temporal averages, we define the Beaufort Gyre region as within the box shown in Figure 3.2. Taking the mean over the five year period (April/May 2011 – April/May 2015) at each 25-km grid point (Figure 3.2a) demonstrates the similarity of average ice and geostrophic ocean velocities. Two main flow patterns emerge based on position in the gyre. In the eastern Beaufort Gyre region, the ocean velocities are constrained to align with bathymetry and run parallel to the Canadian Archipelago while the ice has a component towards the gyre center. In the western portion of the Beaufort Gyre region, the

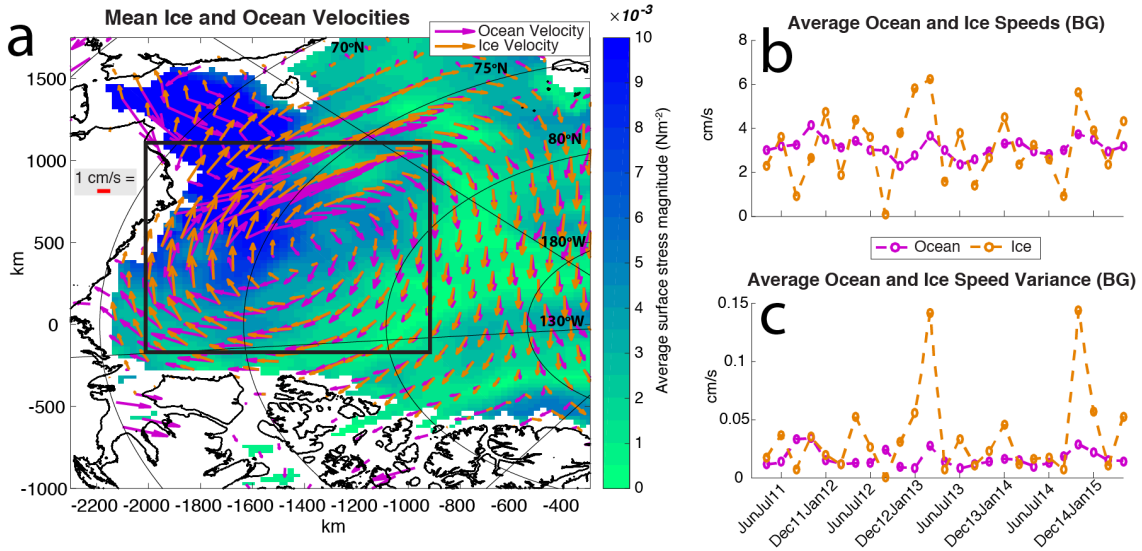

Figure 3.2 (a) Map of average ocean and ice velocity vectors over average surface stress magnitude. Ice velocities are only included in the calculation when ice is present. High stress magnitudes are centered in the area of the western Beaufort Gyre, an area of particularly energetic ocean flow. **(b & c)** Timeseries of ice and ocean speeds and variance in the Beaufort Gyre region, as indicated by the box in panel a. The ice and ocean move at comparable speeds though the ice speed typically has more variance.

ocean demonstrates energetic northwestward flow. This flow has a large impact on ice-ocean stress and Ekman pumping in the region.

The averages over the Beaufort Gyre region indicate that the time-average ice and surface geostrophic ocean speeds are nearly the same, ranging from 1-6cm/s (Figure 3.2b), and that this speed agrees with the model-based findings of *Zhang et al.* [2016a; see their Figure 8], which were 3-4 cm/s after 2008. The ice, however, demonstrates higher speed variance (Figure 3.2c), compared to an ocean whose speed is more constant, similar to TC82. The ice variance, along with ice speed, tends to peak in the winter (Dec-Jan), likely due to intense storm events. Storminess may have caused the strong peak in Dec14-Jan15, because it was an exceptionally windy winter according to the model results of Liu et al. (2015). In Dec12-Jan13, the high variance may be due to a more motile ice pack following an extreme summer concentration minimum [*Parkinson & Comiso*, 2013]. Variance and speed peak to a lesser extent in the spring at the onset of the melt season (Apr-May and Jun-Jul) as the ice pack first starts to loosen.

3.5 Ice-Ocean Feedback: Implications for Gyre Equilibration

The relative velocities of the ice and ocean determine which part of the ice-ocean system is exerting stress on the other. In a system where the ice and ocean are both moving anticyclonically, if the ice is moving faster than the ocean, downward Ekman pumping of the pycnocline and increased doming result. If the surface ocean is moving faster than the ice, the sign of the Ekman pumping reverses, the ocean surface flattens or dishes, and the system becomes an upwelling, divergent system (Figure 3.1).

The frequency with which the average Ekman pumping is of one sign or the other can indicate the stability of the gyre: If the gyre is convergent about half the time and divergent the other half, then we expect a stable system with a constant average upper-ocean freshwater content. *Zhang et al.* [2016a] show that freshwater content in the Beaufort Gyre is fairly stable

based on model output; *Krishfield et al.* [2014] observe the beginning of a freshwater content plateau in ice-tethered profile data. Raw data from the Beaufort Gyre moorings show the same plateau through 2015 (Woods Hole Oceanographic Institution, 2017; see their Figure 3).

We use two measures of the frequency of divergence versus convergence. One is the spatially-averaged value of Ekman pumping through time, and the other is the frequency with which ice-ocean stress opposes ocean motion (i.e., the swiftly-flowing ocean is driving the ice). We consider the ocean to be driving the ice when the ocean speed exceeds ice speed and the ocean velocity vector is within 23 degrees (β) of the ocean-to-ice (opposite of ice-to-ocean) stress vector. A map of the percentage of 2-month periods when the ocean drives the ice (Figure 3.3a) shows that for much of the Beaufort Gyre region, the ocean drives the ice about half the time. This is particularly true in the west near the Northwind Ridge region, in the northern part of the Beaufort Gyre, and along the margin of the Canadian Archipelago.

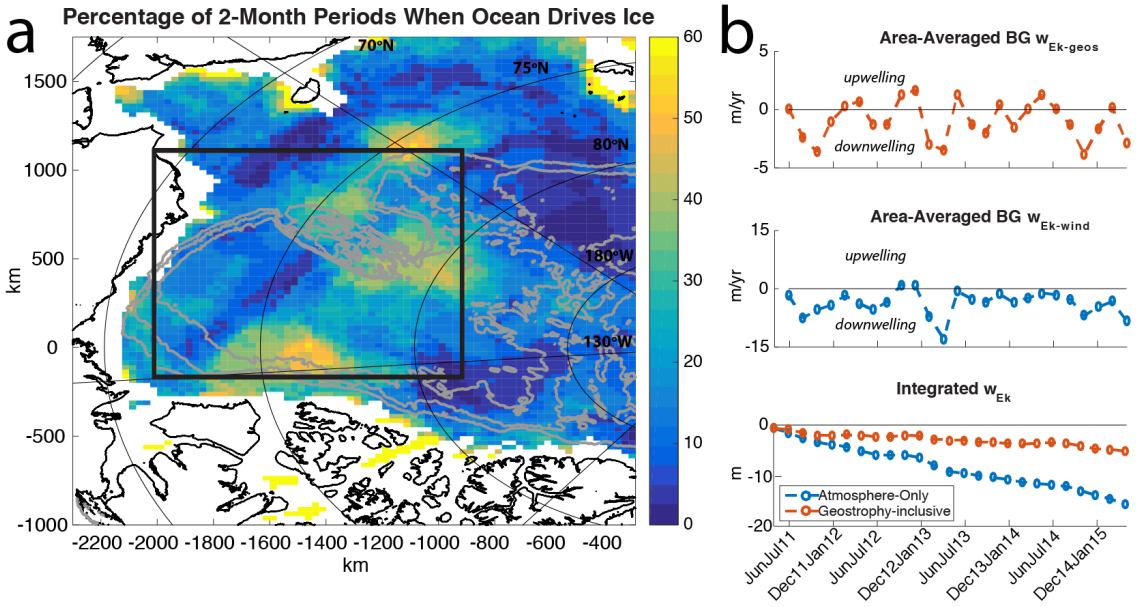

Figure 3.3 (a) Map of the frequency with which ocean drives the ice. This parameter is calculated from how often ocean speed exceeds the ice speed ocean velocity vectors are pointed in the same direction (within $\beta = 23°$) as ocean-to-ice stress vectors. Within the Beaufort Gyre region, as indicated by the box, the ocean drives the ice between 20% and 60% of the time. **(b)** Timeseries of the Beaufort Gyre region average $W_{Ek\text{-}geos}$, as calculated within the box in panel **a**. When geostrophic ocean velocity is included in the calculation, upwelling conditions prevail about 40% of the time, consistent with the frequency range shown in panel **a**. When only the atmosphere is considered in the calculation of $W_{Ek\text{-}wind}$ (middle), the Beaufort Gyre switches to a consistently downwelling system. The order of magnitude of $W_{Ek\text{-}wind}$ is consistent with the 10-20 myr^{-1} downwelling rate reported by Timmermans et al. [2014]. When each of these quantities is cumulatively integrated through time (bottom), the change in meters in height of the geostrophic-inclusive scenario is one-third that of the atmosphere-only case, and closer to the 0 value that would indicate a stable gyre. In a stable gyre, this difference from 0 can be accounted for by the effects of other processes, such as horizontal eddy fluxes.

Considering $W_{Ek\text{-}geos}$ versus time (Figure 3.3b), we see that the Beaufort Gyre is an upwelling system about 40% of the time. There is a small seasonal signal when like months are averaged, with increased downwelling in the spring and fall and downwelling minima spaced 6-8 months apart, but this signal is overshadowed by other variations. With only the wind stress as forcing (that is, calculating $W_{Ek\text{-}wind}$ using only $C_d \rho_a \vec{U}_{10} \left| \vec{U}_{10} \right|$ and no ice-ocean stress), only two 2-month periods out of 25 demonstrate upwelling and there is even less variability in $W_{Ek\text{-}wind}$.

Cumulatively integrating these quantities through time yields about 5 m of downwelling for $W_{Ek\text{-}geos}$, which, while negative, is a third of the value of $W_{Ek\text{-}wind}$ when only atmospheric forcing is considered. This difference suggests that the reversals in $W_{Ek\text{-}geos}$ bring the integral closer to the 0 value of a fully stabilized gyre.

Additionally, the timeseries of $W_{Ek\text{-}geos}$ and geostrophic ocean velocities characterize the feedback that stabilizes the gyre. Take, for instance, the convergent scenario: With increased doming, we expect an increase in geostrophic ocean velocities (resulting from increased DOT) to lag slightly behind the peak of downwelling, or negative $W_{Ek\text{-}geos}$. Indeed, when the timeseries of $W_{Ek\text{-}geos}$ and geostrophic ocean speed are considered, there is a significant negative correlation between the two ($r=-0.6$, $p<0.01$) at a two-month lag. The geostrophic ocean speed is not significantly autocorrelated beyond zero lag, so the $W_{Ek\text{-}geos}$-ocean speed relationship supports the proposed oceanic gyre equilibration mechanism. Thus, the timescale for this equilibration process is on the order of months (e.g., *Dewey et al*., 2017), not years. It is likely that this process has always been occurring, but our ability to observe it has been limited.

A question arising from this temporal analysis is whether the spatial distribution of $W_{Ek\text{-}geos}$ has any influence on stabilization. Not only should Ekman pumping be considered through time, but also through space. A map of the average ocean surface stress curl from Apr-May 2011 through Apr-May 2015 shows some patchiness in downwelling and upwelling (Figure 3.4a)—patchiness not constrained to the Beaufort Gyre, indicating the potential for similar ice-ocean interaction to be occurring basin-wide.

The presence or absence of sea ice hints at some of the reason for this patchiness. The sea ice concentration most conducive to stress curl reversals in the Beaufort Gyre is around 50%-80% (Figure 3.4b). *Martin et al.* [2014] point to the upper end of this concentration range as

optimal for momentum transfer from air to ocean. Bordering the Canadian Archipelago, the ice concentration is higher and curl reversals more likely result from the differences in directions of ice and water velocities—even as average curl over the gyre may be negative, it may become positive locally where horizontal velocity shear occurs near land or less mobile ice. These conditions underscore the necessity of ice cover for stress curl reversal.

In the context of so much literature using wind stress curl as the determinant of Ekman pumping (e.g., *Giles*, 2012) and/or assuming zero ocean velocity (e.g., *Petty* et al., 2016; *Timmermans et al.,* 2014), this calculation of ocean surface stress invites comparison with "atmosphere-only" and "zero ocean geostrophic current" scenarios. The degree to which the ocean surface stress in these cases differs from our earlier results demonstrates the importance of ice-ocean stress and nonzero geostrophic current, respectively. Atmosphere-only forcing (Figure 3.4c) and zero geostrophic current (Figure 3.4d) show the same pattern of upwelling adjacent to the coast with downwelling in the central Beaufort Gyre region. The scenario in which there is no geostrophic current has more coastal upwelling, indicating that the ice-ocean stress curl exceeds the theoretical atmosphere-ocean stress curl. This result is consistent with *Spreen et al.* [2011], who observe an increase in ice drift speed that cannot be accounted for by wind speed trends. They attribute much of this increase, especially in the near-coastal marginal seas, to thinner ice cover (i.e., wind momentum is converted into ice momentum more readily, with less internal ice stress).

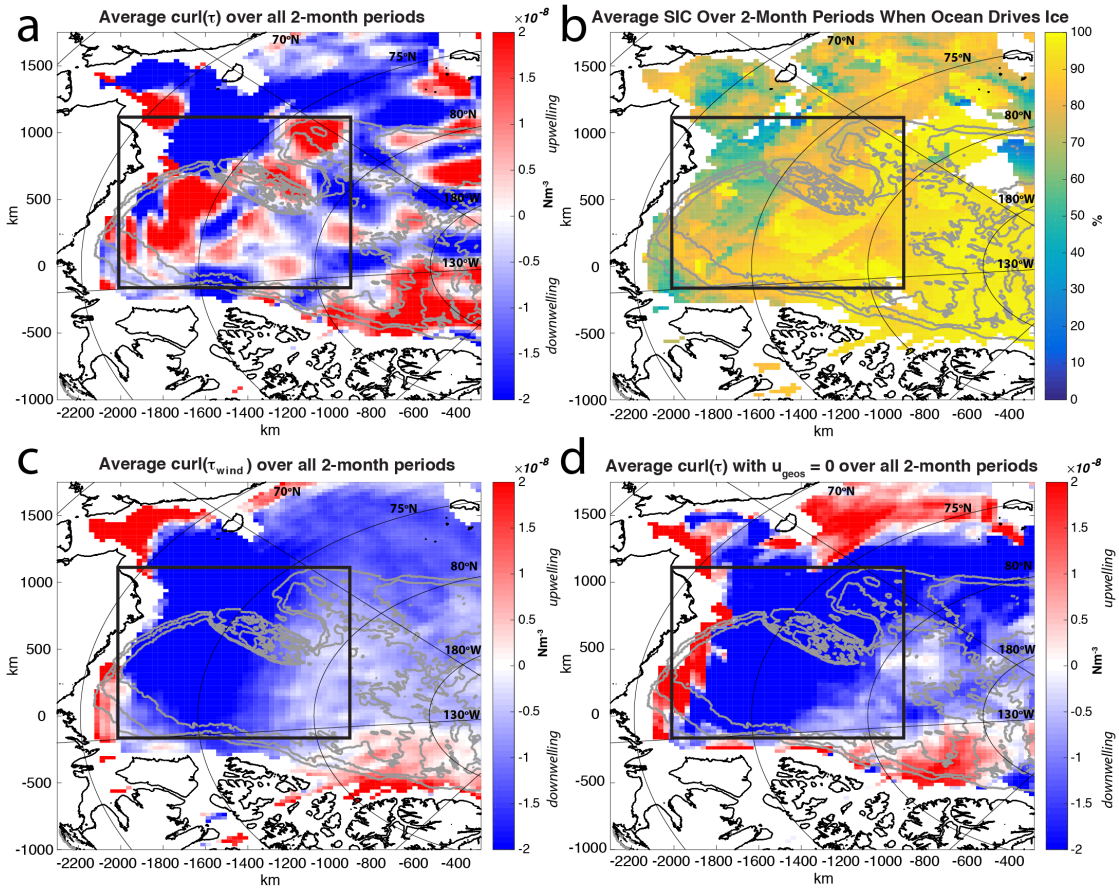

Figure 3.4 Maps showing **(a)** the average ocean surface stress curl over all months April/May 2011 – April/May 2015. The patchy nature of the curl map suggests interesting ice-ocean interaction outside of the immediate Beaufort Gyre. **(b)** average sea ice cover over the periods when the ocean drives the ice (see Figure 3.3a for frequency map), and average ocean surface stress curl for the case studies of **(c)** wind-only forcing and **(d)** zero ocean geostrophic velocity.

3.6 Timescales for Equilibration

Primarily because of the variability we see in Ekman pumping at bimonthly time scales (Figure 3.3a), our sense is that the Ekman pumping – ice drag stabilization has a time scale of days to 1 or 2 months. The data demonstrate variability at the 2-month interval inherent in our DOT averages. However, higher-frequency variability more likely comes from the atmosphere than the ocean. The time-scale between major wind forcing events is about 2 to 3 weeks. The

time-scales of the physical processes are shorter still. The time-scale of the Ekman pumping process is f^{-1}, or about 12 hours.

The inherent time scale for the decay of ice velocity due to horizontal shear in the ice (Eq. 3.1) is $T = \frac{\rho L^2}{K_{viscous}}$, where $K_{viscous}$ is the shear viscosity for an assumed viscous ice rheology. For a length scale, L=200 km, corresponding to the scale beyond which surface forces have tended to dominate internal ice stress (TC82), and for $K_{viscous}$ equal to 10^{10} kg m^{-1}s^{-1} [*Leppäranta*, 2005], T equals one hour. At the low end of the viscosity range, with $K_{viscous} = 10^8$ kg m^{-1}s^{-1}, T equals about 4 days. These scales indicate Ekman pumping and ice drag stabilize ice and ocean velocity at time scales of less than a week.

In contrast, gyre adjustment through eddy generation occurs with a time-scale ($T \sim L^2/K_{eddy}$) of 6 years [*Manucharyan and Spall*, 2016]. Observations suggest K_{eddy} =500 m^{2}s^{-1} [*Meneghello et al*., 2017], implying T=3 years for L=200 km. *Carmack et al.* [2008] estimate the ocean freshwater residence time in the Canada Basin to be 11 years, with the sea ice residence time closer to 3-5 years, suggesting similar time-scales for leakage of mass and momentum from the gyre. These diffusion processes have time scales much longer than the Ekman pumping–ice drag feedback.

3.7 Conclusions

We have calculated ocean surface stress using DOT-derived geostrophic velocities, satellite-derived ice velocities, and reanalysis winds. Ocean geostrophic velocity in the Beaufort Gyre area rivals that of the overlying sea ice, and the ocean often drives the ice, leading to frequent surface stress curl reversals. With these reversals come changes in the ocean between up- and downwelling systems, leading to a gyre that is stable over time. We propose a feedback

between the internal ice stress and the ocean geostrophic velocity, such that the relative influences of wind forcing and internal ice stress influence the doming of the ice and water and their velocities in turn (Figure 3.1).

Based on the fundamental force balance introduced in Section 1, we think that this mechanism for gyre equilibration has been in place as long as there has been an ice cover in the Beaufort Gyre substantial enough to generate internal ice stress. Only recent advances in observations have allowed it to be measured. Among the different dissipation processes that may counteract wind-driven gyre spin up, our proposed mechanism operates on daily to monthly scales. Consequently, the interplay of atmosphere, ice, and ocean has reached a critical point where the Beaufort Gyre is stable following years of spin-up. Geostrophic ocean currents rival ice motion and cannot be neglected.

Chapter 4: *Using remote sensing to revisit foundational dynamic calculations.*

This chapter is being prepared for journal submission as "Dewey, S., Morison, J., Kwok, R., Dickinson, S., & Morison, D., 2019 (in prep). Revisiting Empirically-Derived Western Arctic Ice-Ocean Stress Coefficients in the Age of Satellite Remote Sensing."

4.1 Background

The Arctic Ocean's sea ice is inarguably changing, experiencing a decline in its areal coverage, thickness, and year-to-year persistence (Strong & Rigor, 2013; Comiso et al., 2007; Maslanik, 2011; Peng et al., 2018). As a result of this change, air-ice-ocean momentum transfer has also evolved, in part leading to an acceleration of western Arctic Ocean geostrophic currents in the last decade (Giles et al., 2012; McPhee, 2013; Armitage et al., 2017). Given this acceleration, the traditional conception of an ice cover exerting stress on a passive ocean is no longer always valid. Recent investigations of western Arctic ice-ocean interaction have focused on an accelerated ocean's role in driving surface stress curl changes, often acting as a leading-order agent in Beaufort Gyre equilibration (Dewey et al., 2018; Zhong et al., 2017; Meneghello et al., 2018).

Each of these investigations has employed a fixed ice-ocean drag coefficient common to most of the ice-ocean models in the Arctic Ocean Model Intercomparison Project (AOMIP, Woods Hole Oceanographic Institution, 2010). However, given the recent changes in the sea ice and ocean this parameter and its provenance bear revisiting. The canonical value of the magnitude of the geostrophic drag coefficient, 5.5×10^{-3}, is based on twice-daily measurements of ice and wind velocity sampled during the Arctic Ice Dynamics Joint Experiment (AIDJEX) in 1975 (McPhee, 1980). Based on the formula for the momentum balance of sea ice in free drift (i.e., no internal ice stress), McPhee (1980) calculates the ice-ocean stress as a residual from wind and ice velocity data and an assumed ocean geostrophic velocity based on hydrography.

This approach to the ice-ocean drag coefficient is compelling in its simplicity and efficiency and effectively averages over variations in turbulent stresses and form drag. It also lends itself to the kind of large-scale remote sensing study undertaken here. In this chapter, we employ in-situ and satellite observations to estimate the ice-ocean geostrophic drag coefficient in the Beaufort Gyre region at daily to monthly scales, using the force balance of McPhee (1980).

While this is one of the first observational studies to attempt to update the 5.5×10^{-3} value, several modeling studies have also tackled this problem. The emphasis of many of these investigations, however, has been to partition types of stress (e.g. form drag vs. skin friction) and to evaluate parameterizations in each particular model (Martin et al., 2016; Lu et al., 2011; Tsamados et al., 2014). Because these parameterizations allow drag coefficients to vary, observational determinations of these coefficients and their variation are useful. Additionally, with the growth of the marginal and seasonal ice zones (Strong & Rigor, 2013; Steele & Ermold, 2015) and the recent ability of models to resolve and incorporate appropriate floe size distributions (Arntsen et al., 2015; Zhang et al., 2015; Zhang et al., 2016b; Stern et al., 2018), the partitioning of stress on sea ice is a fertile area of research. While our observational study calculates only a total geostrophic ice-ocean drag coefficient, we do discuss how different contributing stresses may be affecting that overall value, and how that value changes with time.

The use of observations to calculate drag coefficients has many merits. Not only does it put bounds on the total value of the drag coefficient, it is crucial to modeling accuracy (Castellani et al, 2018) and interpretation. Ice-ocean drag is directly related to calculating Ekman pumping and ocean freshwater content redistribution. Locally, this freshwater influences stratification and sea ice formation, and its export from the Arctic drives global ocean circulation (Aagaard and Carmack, 1989; Koenigk et al., 2007; Jahn & Holland, 2013; Sévellec et al., 2017).

Moreover, the interdependence of salt, heat, and momentum fluxes means that the correct drag coefficient and related friction velocity have a great bearing not only on the ocean's mechanics, but also on its thermodynamics (Maykut & McPhee, 1995). Accurately constraining drag also has implications for model feedbacks, since often model ice growth and melt are parameterized according to fields such as lead fraction indices (Roy et al., 2015) and ice thickness, which alter the thermodynamics and mechanics of the ice.

The first section of this chapter discusses the data sources and methods used in the calculation of a Beaufort Sea regional ice-ocean drag coefficient under conditions of free drift; the second compares the calculated values to observational and modeled values from the literature; and the third explores the potential drivers for variations in the drag coefficient, including calculated uncertainty. The final section motivates and suggests future directions for this line of inquiry.

4.2 Methods & Data

We calculate daily values of the ice-ocean drag coefficient magnitude, C_w, and turning angle, β, from 2011-2015 using the stress balance for an ice floe in free drift (Figure 4.1). In this scenario, the stresses of wind and water on the ice are balanced by the Coriolis force, and the ice does not experience any internal stress or floe interaction force. Assuming a quadratic drag law and per McPhee (1980), the momentum balance is thus

$$\rho_a C_{10} \vec{U}_{10}{}^2 = imf\vec{V} + \rho_w C_w e^{i\beta} \vec{V}^2 \qquad (1)$$

where vectors of ice and ocean velocities and stresses are expressed in complex notation with imaginary components north and real components east, and vector "squared" quantities may be understood as $\vec{V}^2 = (u^2 + v^2)e^{itan^{-1}(v/u)}$, where $\vec{V} = \langle u, v \rangle$.

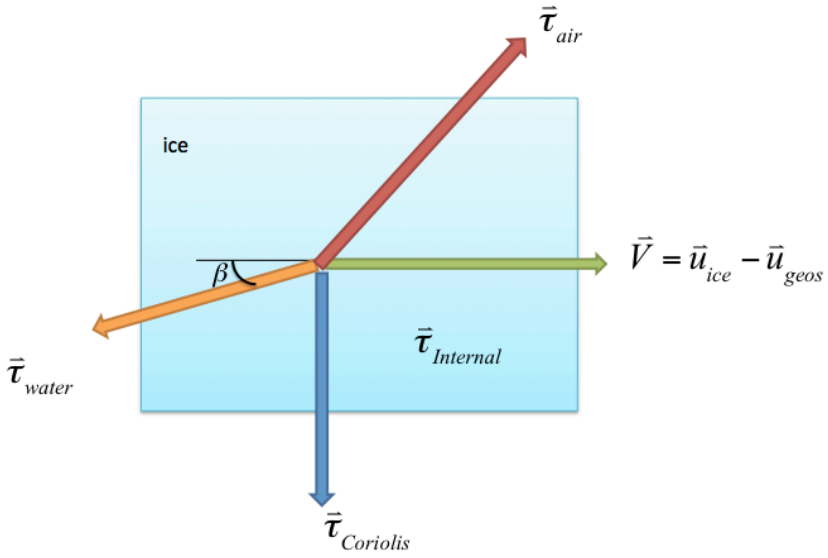

Figure 4.1. Ice force balance diagram in a coordinate system moving at the geostrophic ocean velocity (due to sea surface tilt) as in McPhee (1980). Vectors are meant to illustrate relative directions and are not to scale.

ρ_a is the density of air, C_{10} the 10-meter air-ice drag coefficient, and $\vec{U}_{10}$ the 10-meter wind velocity. m is the average mass of the ice per unit area, f the Coriolis parameter, and $\vec{V}$ is the ice velocity relative to the geostrophic ocean current due to sea surface tilt. ρ_w is the density of seawater, and $C_w e^{i\beta}$ the ice-ocean geostrophic drag coefficient, inclusive of a turning angle, β. Rearranged per McPhee (1980), this equation becomes

$$\frac{\vec{U}_{10}^{\,2}}{\vec{V}^2} e^{i\delta} = \frac{\rho_w C_w}{\rho_a C_{10}} \left\{ e^{i\beta} + \frac{mf}{\rho_w C_w \vec{V}} e^{i\pi/2} \right\} \qquad (2)$$

Where δ is the angle between the ice and wind velocity vectors. Solving for $C_w e^{i\beta}$ yields

$$C_w e^{i\beta} = \frac{\rho_a}{\rho_w} \frac{C_{10}\vec{U}_{10}^{\,2}}{\vec{V}^2} e^{i\delta} - \frac{mf}{\rho_w \vec{V}} e^{i\pi/2} \qquad (3)$$

Each of the variables on the right hand side is available from satellite remote sensing datasets, climatology, or reanalysis, or can be derived from these observations. The value of ρ_a is held constant at 1.25 kgm^{-3}. C_{10} is taken from recent airborne observations of surface roughness

in the Beaufort Gyre region (Petty et al., 2017) and set at 1.18×10^{-3}. Geostrophic ocean velocity is derived from monthly averages of CryoSat-2 dynamic ocean topography and interpolated to daily resolution, and daily ice velocities are taken from the IABP-D product (Polar Science Center, 2018), which optimally-interpolates buoy drift to create a velocity grid at 2° latitude by 10° longitude resolution, from 70°N to 90°N and 0° to 360°. $\vec{U}_{10}$ comes from ERA-Interim reanalysis (Dee et al., 2011), and ρ_w is from the PHC climatology (Steele et al., 2001). While ERA-Interim is a reanalysis, its wind velocity components are post-processed to be comparable to nearby meteorological observations (ECMWF, 2018). The processing and rationale for use of each particular dataset in this chapter are described in greater detail in Dewey et al. (2018).

When we perform calculations using buoy-derived ice velocities, we use interpolated values at each point corresponding to each IABP-D optimally-interpolated location. In the Beaufort Gyre, these four points lie at 74°N and 78°N by 140°W and 160°W. Thus our sampling locations are similar to McPhee (1980)'s original use of four AIDJEX camps and Cole et al. (2017)'s use of four instrumented clusters, though they are more widely spread geographically (Figure 4.2). With buoy-derived ice velocities (and later in this chapter, satellite-derived velocities), we base our calculations on gridded observational data rather than point measurements at specific stations.

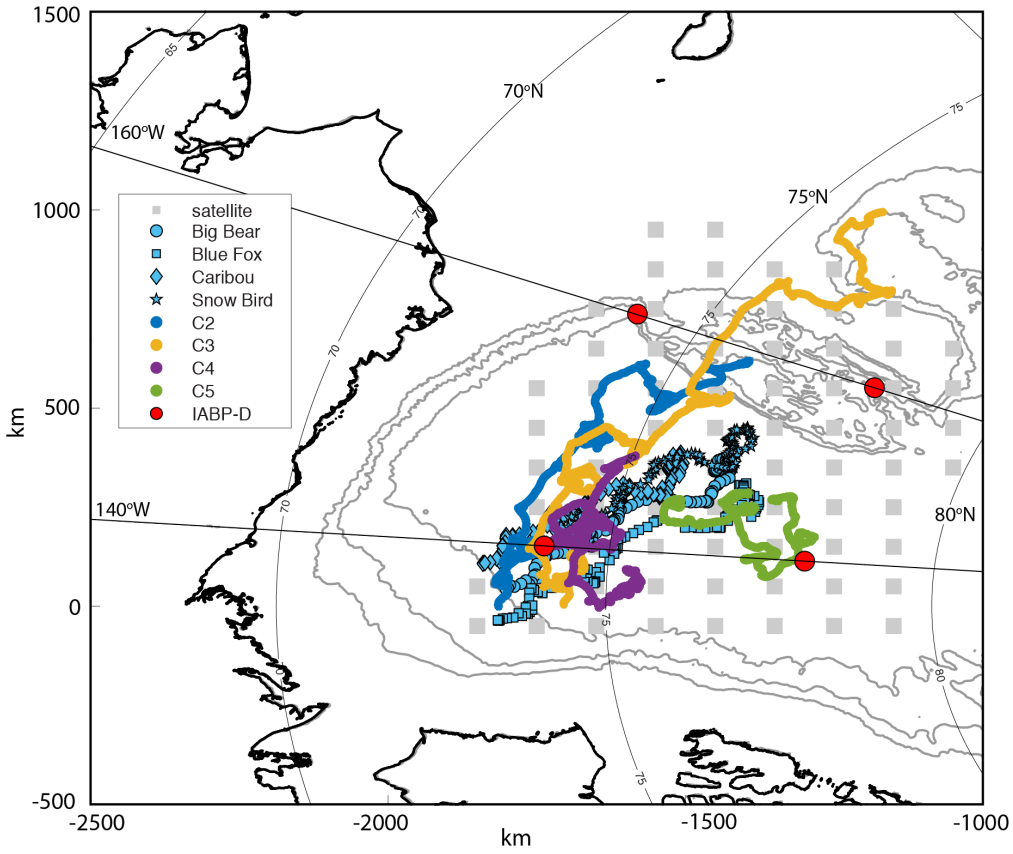

Figure 4.2 Map of field measurements from AIDJEX, MIZ (Cole et al., 2017), IABP-D, and satellite ice velocity grid points from Kwok et al. (2013). Cyan shapes show each of the drifting ice stations from AIJDEX, from 1 June – 30 September 1975. Colored lines show the drift tracks of ITPs during 2014. Red dots show the grid points for the optimally-interpolated IADP-D daily ice drift velocity product, and gray squares show the satellite ice velocity grid points.

This gridding can lead to its own challenges. If we perform the force balance on a grid cell basis, we must find the average thickness of ice within each grid cell. In order to calculate the effective average ice mass per unit area we multiply thickness taken at monthly intervals from CryoSat-2 (Kwok & Cunningham, 2015) with an assumed constant ice density of 917 kgm^{-3}. Because these thickness data are only available at monthly resolution and from October to April, we perform an annual cosine harmonic fit to the product of these two variables,

reflecting the behavior of modeled volume trends (Schweiger et al., 2011; Roy et al., 2015), in order to interpolate over missing months.

Sea ice concentration is taken from SSMI (Kaleschke et al., 2001). In our present study, calculated values of $C_w e^{i\beta}$ are ignored in grid cells in which the sea ice concentration is 0%. We have run cases in which we scale thickness by concentration, which does not appreciably change the annual volume fit discussed in the previous paragraph. Ice concentration provides a useful reference for free drift, as concentrations less than 80% imply that internal ice stress and interaction forces between floes are at a minimum (Leppäranta & Omstedt, 1990; Leppäranta, 2005). Indeed, we find that the ice concentration at each of the four IABP gridpoints is below 80% from the beginning of July to mid-October of each year.

We first calculate the ice-ocean drag coefficient and turning angle at daily resolution from 2011-2015. As in McPhee (1980), we edit our buoy-derived ice velocity time series to exclude those cases when the difference between ice and ocean velocities is less than 8 cms^{-1}. We then apply a 28-day weighted linear least squares regression smoothing filter (Matlab's rlowess.m), to the calculated ice-ocean drag coefficient and turning angle. This filter first computes a local weighted regression, then further weights the regression using the mean absolute deviation (MAD) of the residuals, assigning zero weight when the residuals are greater than 6 MAD and thus diminishing the effect of outliers. This filtering gives a clearer indication of the month-to-month behavior of the drag coefficient, without the noise inherent in daily velocity data. We take the mean value of the calculated drag coefficients and turning angles from four different grid cells of the optimally interpolated IABP-D dataset. These locations are near both the region of AIDJEX drift and the Marginal Ice Zone clusters used in the Cole et al. (2017)

in-situ calculation of drag coefficients, enabling comparison of our values of C_w and β with those from the literature.

Because deriving the ice-ocean drag coefficient from a stress balance relies on an assumption of zero internal ice stress, it is good to validate this free drift assumption using observations. One benefit of our high-velocity editing is that it reduces the relative impact of unaccounted-for internal ice stress. By virtue of the quadratic dependence of stress on velocity, this editing ensures that the force balance is dominated by ice-ocean stress relative to internal ice stress. Here we also use the ratio of ice to wind speed, a variation on the Nansen number, as an indication of free drift. The commonly accepted threshold for free drift conditions in the Arctic is 2% (Leppäranta, 2005), and Cole et al. (2017) use this same ratio and criterion. (The Nansen number may also be estimated from the ratio of wind and water drag coefficients on the ice once they are known [Leppäranta, 2005]). For his own determination of free drift, McPhee (1980) compares modeled and observed ice velocity behavior, as well as examining summertime enhancement of inertial oscillations in the ice-ocean system.

We use both 100-km gridded monthly satellite-derived ice velocities (Kwok et al., 2013) and daily IABP buoy-derived velocities to get a sense of this Nansen number, and find that our approximation of the Nansen number approaches or exceeds the 2% threshold during July through October of each year (Figure 4.3). We opt to use daily buoy-derived velocities in subsequent calculations in part because they meet this criterion, and to optimize for temporal resolution when editing out velocities lower than 0.08 cms^{-1}. For clarity and consistency, we mark July 1 through October 31 in all time series figures to indicate the free drift period. This window extends from melt onset to the beginning of freeze-up, corresponds with sea ice concentrations at or below 80%, and also serves as a helpful visual reference.

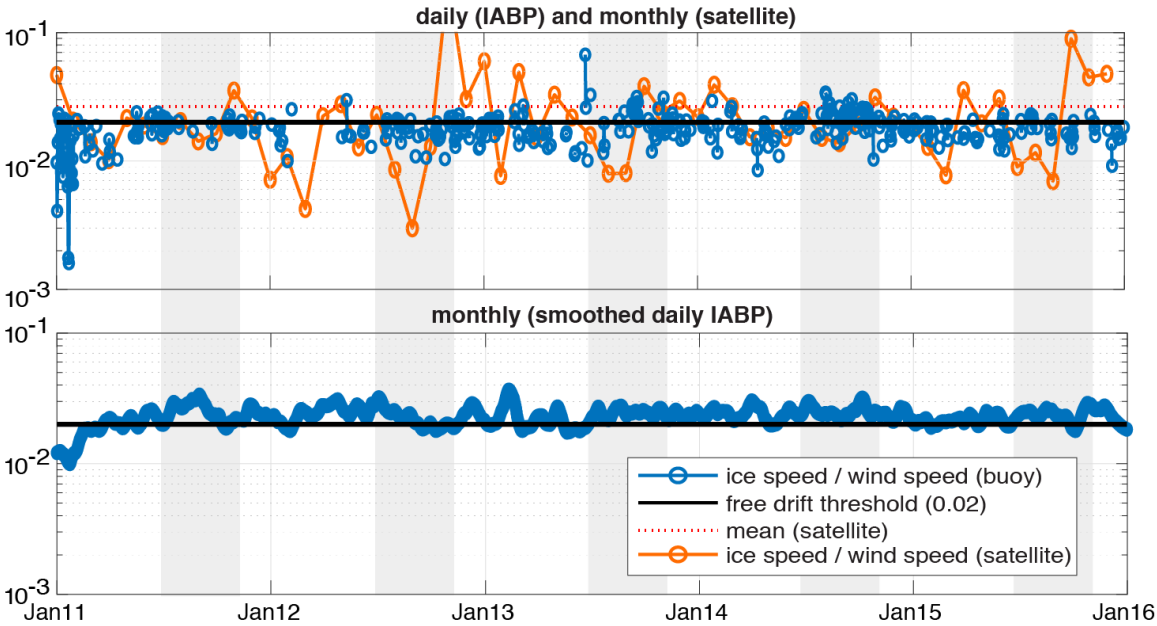

Figure 4.3. Daily ratios of ice speed to wind speed, calculated using daily IABP-D velocities (blue), before (top) and after (bottom) smoothing with a 28-day weighted linear least squares regression. Values calculated using monthly ice velocities (orange) are shown for comparison. The 2% free drift threshold is denoted with a horizontal black line, and the mean of the satellite timeseries is shown in red. Vertical gray bars over each timeseries denote the July 1 – October 31 period of assumed free drift.

4.3 Values of the Ice-Ocean Drag Coefficient

Within the larger July-October window, we calculate our ice-ocean drag coefficient and turning angle from 20 July-29 August (Julian days 201-241), the period over which McPhee (1980) derived the 5.5×10^{-3} and 23° values. During that time, our smoothed C_w calculated with daily IABP-D buoy-derived ice velocities varies between 1.8×10^{-3} and 1.1×10^{-2} (Figure 4.4), with a mean value of 4.7×10^{-3}. Values of the ice-ocean turning angle reach up to 80° though primarily they vary about a mean of 41° during our calculation window, in agreement with those of Cole et al. (2017). The turning angle is usually highest when the drag coefficient is lowest, with the highest turning angles during seasons of melt. Unlike the drag coefficient, the ice-ocean turning

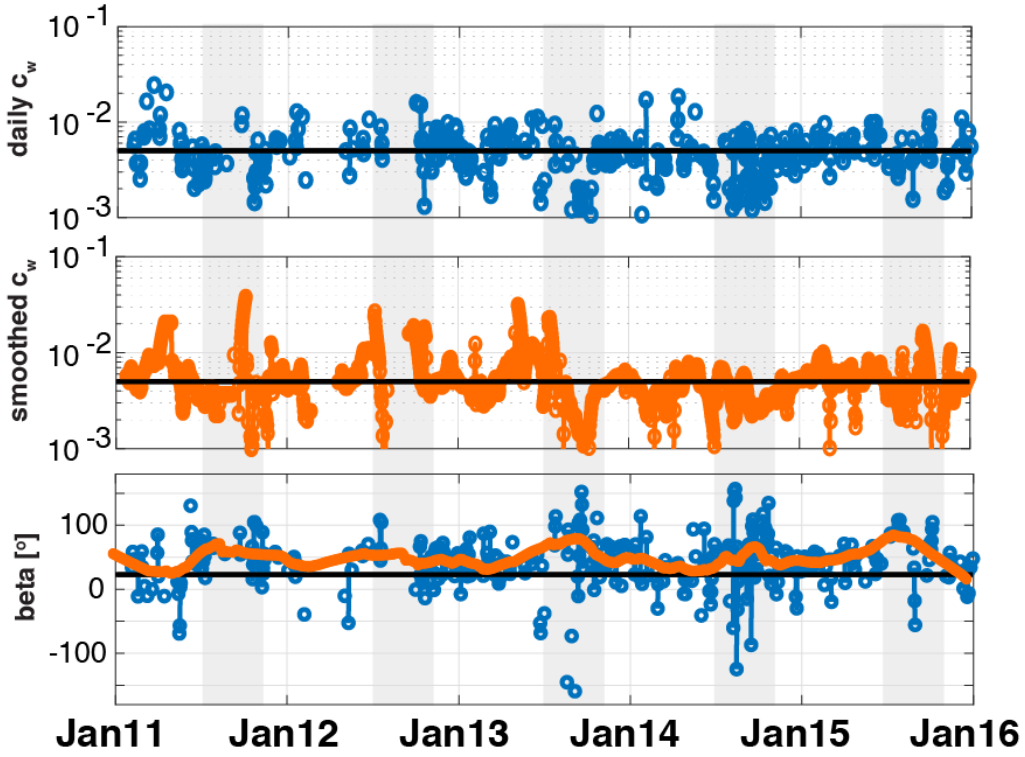

Figure 4.4. Timeseries of average C_w before (top) and after (middle) smoothing. Bottom: Average β before (blue) and after (orange) smoothing. Black bars in each subplot denote historical values, 5.5×10^{-3} (C_w) and 23° (β). Vertical gray bars denote the July1 – October 31 assumed period of free drift.

angle has increased slightly since AIDJEX, when the value of β varied from 4.6°-36° about an average of 23° across all stations during forty days of the summer (McPhee, 1980).

Our calculations of C_w are bounded by those from the recent Marginal Ice Zone experiment, in which Arctic Ocean Flux Buoy (described in Shaw et al., 2008) turbulence measurements at four clusters yield median values of C_w ranging from $4\text{x}10^{-4}$ to $2\text{x}10^{-2}$ (Cole et al., 2017, see their Figure 12) during the July-August calculation window. The authors directly calculate a friction velocity u_*, ($(\boldsymbol{\tau}/\boldsymbol{\rho})^{1/2}$) from velocity sensors mounted on Ice-Tethered Profilers. This friction velocity is a point measurement of stress, which Cole et al. (2017) relate to the local relative (ice minus ocean) velocity through C_w, and which does not require the force balance assumption that we have used. That these two distinctly different methods yield results in approximate agreement lends confidence to our own calculations. The values of C_w and β are also similar to those found by Randelhoff et al. (2014), who directly calculated u_* from an ice-mounted turbulence instrument cluster during a weeklong (26 July-3 August) survey in the Nansen Basin of the Eastern Arctic, another area of high variability in seasonal sea ice concentration.

The Beaufort Sea C_w has decreased and β has increased since AIDJEX; we present several reasons why in the next section.

4.4 Variation of the Ice-Ocean Drag Coefficient

We explore two different explanations for the decrease in C_w and concurrent increase in β: roughness and buoyancy flux. In addition to having changed in concentration and thickness since AIDJEX, the character of the ice surface has also changed, with newly-forming first-year ice being smoother than the much more common heavily ridged multiyear ice of the past.

Decreased hydraulic roughness can result in lower drag coefficients and increased turning angles (McPhee, 1979; McPhee, 2012). Therefore we would expect that overall, in an ice regime with more undeformed first-year ice like that in the Beaufort Sea, the drag coefficient would decrease and the turning angle would increase.

A thought experiment reinforces this intuition, and demonstrates the link between decreased ice thickness and ice roughness. If we imagine that the drag coefficient at the base of the ocean's near-surface logarithmic stress layer is close to the geostrophic drag coefficient, we can approximate roughness length $z_0 = he^{\kappa/\sqrt{C_w}}$ (McPhee, 2008) where h =2m is depth and κ = 0.4 is the von Kármán constant. With the assumption that roughness elements of ice (e.g., keels) scale with thickness, halving this roughness length allows us to calculate a new drag coefficient, 4.3×10^{-3}:

$$\frac{1}{2} * he^{\frac{\kappa}{\sqrt{5.5\times10^{-3}}}} = he^{\frac{\kappa}{\sqrt{4.3\times10^{-3}}}} \qquad (4)$$

This coefficient is similar to our average July-August value, 4.7×10^{-3}, suggesting that ice thickness has played a large role in its decrease since AIDJEX.

The difference between the theorized value, 4.3×10^{-3}, and our observed value, 4.7×10^{-3}, may be due to the partitioning between skin and form drag, and to the impact of ice thickness changes on the two types of drag. Pressure-ridge keels and the blunt edges of floes are the causes of form drag, and arguably the height of these features varies with thickness. However, the spacing of keels and floe edges has also varies with ice thickness (Leppäranta, 2005) if the ice is half as thick, the vertical scale of keels will be halved but their spacing would be doubled due to a halving of floe size. For this reason, the form drag may not have been reduced as much as skin friction by the reduction in ice thickness. Previous estimates of the proportion of skin to form drag (Steele et al., 1989; JD Smith, 1976, personal communication) sit around 50%-50%. For

that case, if skin friction C_w was reduced to 4.3×10^{-3} while form drag C_w remained at 5.5×10^{-3}, the average C_w would be 4.9×10^{-3}. A value of 4.7×10^{-3} as we obtain suggests that skin drag may account for 66% of the drag during the July-August window.

We are able to explain much of the change in C_w with decreasing sea ice thickness, but in addition to roughness, the freeze-thaw cycle of the ice may lead to buoyancy fluxes that impact C_w during certain seasons. McPhee (2012) conducts an in-depth analysis of the impact of stratification and a shallow pycnocline on C_w and β, finding that freshwater flux from ice melt increases ice velocity and turning angle for the same ice-ocean stress, and that for higher ice speeds, a shallow pycnocline results in larger turning angles. Randelhoff et al. (2014) confirm this latter result in the Nansen Basin.

To examine the impact of buoyancy flux on our present results, we use changes in ice volume to estimate daily salt flux (analogous to buoyancy flux in the low temperatures of this region) and find that there is significant downward buoyancy flux (freshening and shoaling of the surface mixed layer greater than 0.5 $cmday^{-1}$) during the first half of our assumed July-October free drift period (Figure 4.5). We apply an annual cosine harmonic fit to C_w and β in order to visually highlight their seasonal evolution. The maximum freshwater buoyancy flux appears to immediately precede the annual minimum in C_w and maximum in β (Figure 4.5).

That this relationship is lagged suggests that stratification may be more important than buoyancy flux in determining the drag coefficient. Recent investigations from Beaufort Gyre moorings show that melting and freezing ice only comprised 15%-28% of surface freshwater content change from 2006-2011, greater than had been previously assumed but still small (Krishfield et al., 2014). More compellingly, the Beaufort Gyre is more stratified now than it was in 1975 (Toole et al., 2010), and summer mixed-layers in the region have both shoaled and

freshened in the last 30 years (Peralta-Ferriz & Woodgate, 2015). Thus the seasonal cycle of buoyancy flux is imposed on a background of greater stratification than was present during AIDJEX, and the extrema in C_w and β coincide with the times of expected maximum stratification.

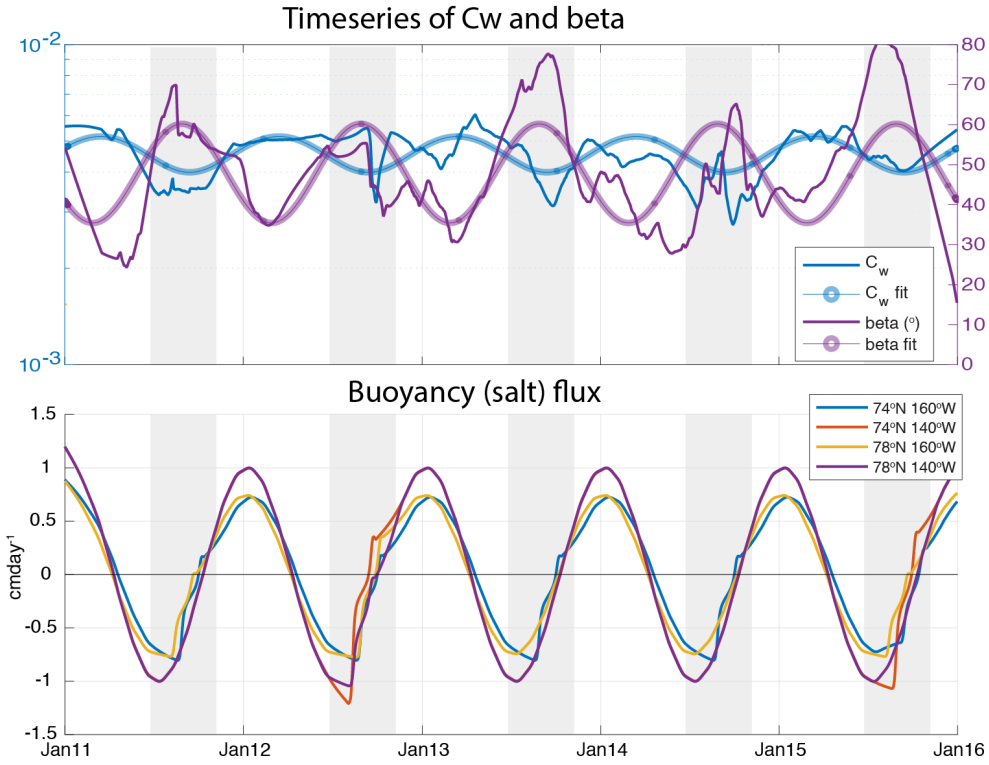

Figure 4.5. Top: Smoothed timeseries of the mean C_w and β, shown with annual cosine harmonic fits. Bottom: Time series of the fresh water flux, used as a proxy for buoyancy flux, at each IABP-D grid point, with gray shading indicating an assumed period of free drift, 1 July – 31 October of each year. Shown in cm day^{-1}, this flux is calculated as a per-unit-area freshwater flux from ice melt or formation.

This variability must be placed in the context of uncertainty, given the many observational datasets used to calculate C_w and β. Rampal et al. (2009) calculate the uncertainty of buoy-derived drifts in IABP to have an upper bound of 0.3-1 cms^{-1}. In the DOT dataset used to calculate geostrophic ocean velocities, the variance in the Beaufort Gyre for each grid cell is a maximum of 0.5 cm, which translates to a velocity uncertainty of up to 2 cms^{-1}. Uncertainties in

thickness (Kwok, 2018; Kwok & Cunningham, 2015) and ERA-Interim wind speeds (Lindsay et al., 2014) are presented relative to observations, and may be taken as 6 cm and 50 cms^{-1}, respectively. During 20 July-29 August, the uncertainty of the mean in C_w is $2.5x10^{-4}$ and that in β is 5.3°. The variances of each parameter are comparable to the variance in values described in Cole et al. (2017) who attribute the wide range in stress coefficients and turning angles to increased surface stratification.

While our confidence in C_w is limited to summer because we lack internal ice stress data, it is worth seeing whether we may infer wintertime internal ice stress magnitudes from our stress balance equation. Assuming that the stress components during free drift periods represent the full force balance without internal ice stress, can we calculate internal ice stress using the difference between a wintertime force balance and these summer conditions? Using our full, unedited velocity dataset, we employ the force balance in Equation 1, assuming that its components sum to some "$\vec{I}$" rather than to zero, and hold the ice-ocean drag coefficient and turning angle constant at $4.7x10^{-3}$ and 41°, representative of the averages derived during free drift. With these assumptions, the magnitude of this internal ice stress term is often twice that of the wind or ocean stress terms. Using the scaling of PH/L per Leppäranta (2005) and treating the internal ice stress as an equivalent surface stress, we estimate the internal stress magnitude in Pa (P) of 1.5 m thick ice (H) over 200 km (L). We find that the internal ice stress with this scaling is 5kPa-15kPa, smaller than previously reported values from drifting buoys (Richter-Menge et al., 2002). However, this stress is of the same magnitude as the modeled compressive strength determined by Zhang & Hibler (1997), 10 kPa (Richter-Menge et al., 2002).

4.5 Discussion

We have used five years of remotely-sensed and in-situ ice and ocean data to derive an ice-ocean geostrophic drag coefficient in the Beaufort Sea. This calculation relies on a sea ice stress balance under the assumption of free drift. It is useful because it is observationally-based, but unlike in-situ turbulence measurements, it is an average over large and varied ice surfaces. However, our results do roughly agree with the outcomes of other recent in-situ ice-ocean drag analyses that use observed ocean vertical velocities to calculate a friction velocity (Cole et al., 2017; Randelhoff et al., 2014), increasing confidence in our own approach.

This study was motivated by the changes in sea ice extent and seasonality that have occurred since AIDJEX, when the analogous seminal sea ice stress balance was first carried out (McPhee, 1980). The upper ocean in the Beaufort Sea region has also freshened substantially since AIDJEX. We find that the free-drift period value of the drag coefficient C_w has decreased slightly since AIDJEX, while the turning angle has increased. These changes are consistent with the effects of decreased ice thickness, and with it roughness, as well as changes in stratification. In an abstract sense we can also think of the reduction in ice thickness as resulting in the turning angle approaching the idealized, vanishing ice, Ekman layer 45° turning angle between surface stress and surface velocity.

A caveat to these values is that they are local to the Beaufort Gyre, and that the climatology masks any significant high-frequency variance. Also, as with McPhee (1980), the lack of internal ice stress data means that we cannot calculate the actual C_w during the winter. We have attempted to explain the effects of internal ice stress and buoyancy flux on drag and its derivation here, but ultimately the applicability of this drag law, as with the result of McPhee's derivation, depends on the consistency of the basic shape and roughness of the underside of the ice cover through the seasons.

4.6 Addendum: Applying the 'new' C_w and β to Chapter 3

A quick calculation can demonstrate the impact of an ice-ocean stress calculated with $C_w = 5.5\text{x}10^{-3}$ and $\beta = 23°$ versus one calculated with $C_w = 4.7\text{x}10^{-3}$ and $\beta = 41°$, assuming the same water density, ice velocity, and ocean velocity. The ratio of these two stresses is 1.17. That is, the original stress is 17% larger than our new value. But how does this calculation translate into a full-basin estimate of ice-ocean stress?

It would seem that this dissertation chapter and its new values for the stress coefficient and turning angle could undermine the conclusions of Chapter 3, in which we based our Ekman pumping calculations on the traditional values of $5.5\text{x}10^{-3}$ for C_w and 23° for β. To assuage any fears that Chapter 3's conclusions may be invalid, we conduct a cursory sensitivity analysis of the integrated Ekman pumping results shown in Figure 3.3b. We find that these results are only sensitive to order-of magnitude changes in C_w and β. Using our updated values of $4.7\text{x}10^{-3}$ and 41°, our results are nearly identical to our original calculations. Doubling or even eliminating β does not appear to have much of an effect.

When we look at order-of-magnitude changes, we find a greater difference in our Chapter 3 results from an increase in C_w than from a decrease. Lowering C_w by an order of magnitude to $5.5\text{x}10^{-4}$ produces comparable results to our original investigation. When C_w is increased to $5.5\text{x}10^{-2}$, however, we find more upwelling results, which would be expected from increased ice-ocean drag, and which makes sense when we consider the timescales of spinup and spindown of the gyre. Spinup is mostly set by wind stress because Ekman pumping is proportional to surface stress, and happens at relatively short timescales (hours to days). However, during spindown when wind stress is small, the force balance is between internal ice stress and ice-ocean stress.

This suggests that an increase the ice-ocean drag coefficient, by increasing the Ekman pumping rate, would shorten the amount of equilibration time.

Chapter 5: Conclusion

This dissertation has examined physical changes in the western Arctic Ocean, describing the mechanisms by which ice, ocean, and atmosphere interact. In this dissertation, we have described how freshwater moves through this system both vertically and horizontally. We have shown that while modern satellite remote sensing tools and airborne hydrographic measurements reveal substantial change in the region, the basic governing equations for ice-ocean interaction have remained the same over the last several decades, As ice cover has become increasingly seasonal and the ocean in the Beaufort Gyre has accelerated, we explore the evolving features of its hydrography and circulation.

We have demonstrated that the shape of the Beaufort Gyre responds to the Arctic Oscillation at a lag of two months, and that the relative velocities of ice and ocean in the region are such that the sign of ocean surface stress curl frequently reverses. With this change, the net Ekman pumping results in a stable gyre, after years of observed spin-up. On smaller scales, we have shown that sea ice melt and formation is a locally one-dimensional process, but that its footprint is coherent across the basin with respect to ice edge position. In these areas of ice melt and formation, we have also described the ice-ocean stress coefficient and turning angle and how they have evolved to modern values. Despite the disparate scales of each of these processes, together the contents of this dissertation provide a three-dimensional, updated description of how the western Arctic Ocean surface physical system operates and transports freshwater, especially under recently diminished ice cover. A concise summary of each chapter, as well as possible future work, follows below.

Local, vertical processes: the mixed layer and its FWC.

In this chapter, we use airborne hydrographic measurements registered to a satellite-derived ice edge to describe temperature and salinity changes in the Beaufort Gyre's top 20 m. We find that both salinity and temperature align with the ice edge position, with temperature changes corresponding to the level of solar insolation available in the absence of ice and salinity signifying the amount of sea ice melt and formation. Back-of-envelope calculations of freshwater content indicate that these features are the result of one-dimensional vertical mixing processes, which we confirm through use of the PWP 1-D model (Price et al., 1986). To simulate the presence of sea ice in our ocean-only PWP, we force the model with output from the larger PIOMAS ice-ocean model (Zhang et al., 2008b), while accounting for biases in PIOMAS' own wind and shortwave radiative forcings.

In order to parse basin-scale and local salinity signals, we use several proxies for background gyre strength: ocean bottom pressure at two sites, the depth of several isopycnals, and the Arctic Oscillation (AO) index (Thompson & Wallace, 1998). Of these proxies, we find that the AO is the most effective for capturing the shape of the Beaufort Gyre, at a two-month lag. Thus a secondary result of this chapter is to confirm earlier studies that have linked gyre doming and freshwater accumulation to the AO (Morison et al., 2012).

Between our initial calculations, observations with the AO signal removed, and the PWP, we find that vertical processes account for at least 77% of salinity variability in the upper 20 m. Therefore, even as the Beaufort Gyre has strong horizontal circulation, its surface properties are set by freeze and melt processes at the ice edge. This result is notable given the recent spin-up of Beaufort Gyre circulation, and compels our investigation of changing surface stresses in Chapter 3.

Large-scale horizontal dynamic processes: basin FWC and equilibration.

Given the increases in Beaufort Gyre currents in the last decade followed by a period of stabilization, we examine the ocean's role in gyre equilibration. From the force balance on sea ice, we derive equations for ocean surface stress and resulting Ekman pumping that include the ocean's geostrophic velocity. We calculate this geostrophic velocity using CryoSat-2 dynamic ocean topography (DOT) measurements at 2-month intervals from 2011-2015. The DOT dataset represents a huge advance in observation of the ice-covered oceans, expanding the sea surface height record beyond sparse in-situ dynamic height calculations and seasonal IceSat DOT. Its measurement relative to the geoid also eliminates the need to select an assumed depth of no motion in calculating geostrophic currents.

While these currents had previously been assumed negligible, we show through comparison with ice speeds that the ocean speed is of the same magnitude as and therefore must contribute to the ice-ocean stress. That the ocean speed sometimes exceeds that of the ice implies that the sign of the ice-ocean stress will be negative—that is, that the ocean is exerting stress on the ice, rather than being driven as a passive slab. Difference in velocity direction between the ice and the ocean can also cause a sign change. Using these two criteria, we find that the ocean is driving the ice 20%-60% of the time during our study period.

As a means of comparison and to examine the spatial distribution of these stress curl reversals, we calculate surface stress with geostrophic current equal to zero. This assumption results in a negative surface stress curl everywhere in the gyre except next to the coasts. The spatial pattern of this stress curl resembles that of wind stress curl, which is similarly negative everywhere in the basin interior. Additionally, the gyre-wide, 5-year cumulatively-integrated

Ekman pumping from each scenario differs by about 15 m, with the geostrophy-inclusive value close to the 0 m of a fully-stabilized gyre.

While our analysis does not fully exclude horizontal eddy flux as a mechanism for equilibration, both this integrated Ekman pumping and the timescale of our ice-ocean interaction suggest that eddy flux is a second-order equilibrator. Due to the transient nature of wind forcing and momentum flux, ice-ocean drag operates at temporal scales of close to a week, whereas eddy-based gyre adjustment works on the order of years.

Reexamining ice-ocean interaction

Having considered how stress contributes to vertical fluxes and to gyre equilibration, in this chapter we revisit the geostrophic ice-ocean stress coefficient. Our gyre stabilization analysis in Chapter 3 as well as many other papers have used a fixed value for this parameter, though many model studies allow it to vary. We seek to determine how much this coefficient and its associated turning angle may have changed since the AIDJEX field program of 1975, and how much they might currently vary. Using the force balance from our discussion of equilibration, we are able to estimate values of the coefficient (C_w) and turning angle (β) during periods of assumed free drift from 2011-2015. This calculation employs observed and derived values, with only the wind velocity taken from a reanalysis, ERA-Interim.

C_w and β are calculated using daily IABP-D buoy-derived velocities, before and after smoothing with a 28-day weighted linear least squares regression. Comparison of these values to those from AIDJEX (McPhee, 1980) and the 2014 Marginal Ice Zone (MIZ) experiment (Cole et al., 2017) show that C_w has slightly decreased, to 4.7×10^{-3}, while β has increased substantially, to 41°. A brief sensitivity analysis of the Chapter 3 results using these updated values shows that

they are much more sensitive to an order-of-magnitude increase in C_w than to a decrease, and that changing or eliminating β had little effect.

We propose two principal explanations for the changes in drag coefficient and turning angle since AIDJEX: that a decrease in C_w and increase in β are a response to decreased ice thickness and increased stratification. We propose a scaling argument wherein thinning ice leads to smaller roughness lengths, and we find that the seasonal cycle of both C_w and β track that of surface buoyancy (salt) flux. Shortly following an influx of freshwater to the system, C_w decreases and β increases, coincident with maximal seasonal stratification, and with C_w's minimum typically corresponding to β's maximum.

All of this variation is consistent through the study period, 2011-2015. This periodicity and the stability of the large-scale Beaufort Gyre system enable the construction of an annual climatology for C_w and β. We are able also to estimate the magnitude of an internal ice stress term, using a fixed C_w and β estimated from free drift and a scaling equation (Leppäranta, 2005). This term is of a similar magnitude to both observed and modeled values.

Future Work

Any suggestion of future research pathways is impossible to decouple from discussion of impending Arctic change. Just as this dissertation has been motivated by the dramatic changes in sea ice cover and ocean circulation in the past decade, it compels us to ask what the consequences of future change might be. As polar scientists in the 21st Century we are constantly chasing the measurement of a stable baseline. Evidence of change can be as anecdotal as the quiet shortening of a field season due to structurally untenable ice camps or as blisteringly obvious as an anomalously high 6°C sea surface temperature measurement from a SIZRS cast.

Resisting at this moment the temptation to place a value judgment on these changes (i.e., loss of perennial sea ice coverage is "bad"), we can instead focus our response on adapting how we meet these changes and make measurements in and of shifting geophysical regimes. As non-residents of the Arctic region, we are limited to an outside observer's perspective. And yet this distance becomes our strongest suit, allowing us to adopt a full-field view of Arctic Ocean change. The tools at our disposal lend themselves to this approach: This dissertation should serve as an introit to modern airborne and space-based measurement of the ice-covered oceans, which are efficient means of environmental sampling across the broad spatial and temporal scales necessary to resolve basin-wide change. These scales have been a thematic undercurrent of this dissertation, an essential backdrop to each chapter, but they bear future examination in their own right, as they are both agents and outcomes of change.

Therefore future work rests in improving observations to match the scales of the phenomena we wish to resolve, and in this manner beginning to address the questions that this dissertation has left unanswered. Chapter 3 described a mechanism on the scale of days which we were only able to infer from monthly data, and Chapter 4, especially, highlighted how even monthly versus daily sampling of ice velocity can impact results. This disparity motivates the work in this dissertation's appendix, which compares observed sea surface height and ocean bottom pressure to show where and when the ocean behaves baroclinically. An obstacle to completing this analysis is data frequency and appropriate filtering, and we rely on moorings to supplement our satellite remotely-sensed data.

Increased observations with satellites such as the European Space Agency's Sentinel-2 and the Canadian Space Agency's recently-launched RADARSAT Constellation will provide sampling rates comparable with mooring sites, with larger spatial coverage. Continuous

observation of the polar regions will be critical to assessing and addressing Arctic Ocean change. The SIZRS program has demonstrated that we have the aircraft range and the scientific skillset to collect repeat atmospheric and hydrographic sections; field operations such as this one will allow us to sustain future observations across large areas in a way that shipboard research and moorings cannot offer.

Most importantly, we have had the benefit of focusing on observations during a period of Beaufort Gyre stability, and the ultimate test of the mechanisms we have proposed for equilibration lies in the future behavior of the system. We have somewhat speculatively identified internal ice stress as the counterbalance to ice-ocean stress in our discussion of gyre stabilization, and yet internal ice stress remains a large unknown in the Arctic system. It is largely dependent on ice rheology, geography, and boundary conditions (Leppäranta, 2005). Improved and increased in-situ observation of this stress remains a critical component of closing the momentum equations in the presence of internal ice stress and floe interaction forces. As the marginal ice zone increases, the latter of these processes is likely to become an unavoidable component of ice-ocean dynamics.

Appendix: Circulation Timescales, Averaging, and Adjustment

A version of this Appendix was presented in poster form at the 2018 American Geophysical Union Fall Meeting: Dewey, S., Morison, J., Kwok, R., Peralta-Ferriz, C., Andersen, R., Dickinson, S. and Morison, D., 2018, December. The observed relationship between dynamic ocean topography and ocean bottom pressure: characterizing Arctic Ocean circulation with complementary satellite tools. In *AGU Fall Meeting Abstracts*.

Abstract

Following similar model investigations (Vinogradova et al., 2007; Bingham & Hughes, 2008), this study combines GRACE, satellite altimetry, and in-situ hydrographic measurements to relate dynamic ocean topography (DOT) to bottom pressure (OBP) purely through observations. Calculated spanning 2003-2016, the coherence between DOT and OBP can reveal the time and space scales on which the ocean behaves baroclinically versus barotropically. This relationship can also illustrate the effect that forcing fields and timescales have on the dynamics that distribute freshwater throughout the Arctic Ocean, linking large-scale atmospheric forcing such as the Arctic Oscillation index with regional ocean behavior. Because these satellite data fields cover the full Arctic Ocean, we will be able to expand our forcing discussion beyond traditionally well-sampled systems such as the Beaufort Gyre, and chart a course for future integrated applications of GRACE-FO and altimetry from ICESat-2.

Background

Because isopycnal surfaces mirror the sea surface height, the relationship between DOT and OBP can describe how baroclinic or barotropic a flow is; when isopycnals align with isobars, the flow is barotropic and vertical density gradients are therefore only a function of pressure. Signals from large-scale atmospheric forcing are visible in DOT and OBP, such as when the ocean surface responds to the Arctic Oscillation index (see Chapter 2), or when submonthly

variations in OBP occur in response to basin-wide sea level pressure gradients (Peralta-Ferriz et al., 2011).

The relationship between DOT and OBP can also illustrate the effect that these forcings' timescales have on dynamics. Addressing this issue, Vinogradova et al. (2007) and Bingham and Hughes (2008) use the MITgcm to generate an admittance function relating sea surface height to OBP at both 1° and 0.25° resolution. They find that the high-latitude oceans are barotropic on timescales of months. Peralta-Ferriz et al. (2014) make a similar conclusion, and find that the marginal shelf seas are more barotropic in character than the deeper basins. The work in this Appendix offers the observational equivalent to these studies, computing the coherence of observed OBP with changes in DOT at varying timescales and at 25 km (~0.25°) resolution.

Evaluating this relationship on multiple timescales can be accomplished with SIZRS monthly hydrography, mooring-derived dynamic height, monthly DOT, monthly bottom pressure information from GRACE and hourly OBP from moorings. GRACE (Gravity Recovery and Climate Experiment) is a pair of satellites launched in 2002, which together measure Earth's gravity field based on their respective accelerations. The original GRACE mission was extended through late 2017, and the GRACE-Follow On (FO) mission was launched in mid-2018, in collaboration with the German Research Center for Geosciences, NASA's partners for the first iteration of GRACE.

Because the GRACE and DOT satellite fields cover the ocean outside of the Beaufort Gyre, we will be able to accurately incorporate the role of the Siberian shelf in Beaufort freshwater accumulation and deposition during these times, thinking beyond the traditional "flywheel" conceptual model of the gyre in which freshwater is alternately gathered or released in response to wind forcing.

Methods

This study integrates satellite remote sensing with in-situ hydrographic observations to describe a full complement of scales in time and space, ranging from daily to monthly and from local to regional; with these assets, we can describe the changing behavior of the ocean and motivate future applications of a new generation of satellite remote sensing instruments, such as IceSat-2 and GRACE-FO.

The satellite data used in this study are publicly available. CryoSat-2 and Envisat DOT data are available from the European Space Agency and from the Radar Altimeter Database System (RADS); the CryoSat-2 and RADS data are processed as described in Dewey et al. (2018). GRACE JPL Mascon data are available from the NASA MEaSUREs Program. Arctic mean values for DOT and OBP are shown in Figure A1. In this study, when the full timeseries is used, DOT data revert to the CryoSat-2 value rather than Envisat.

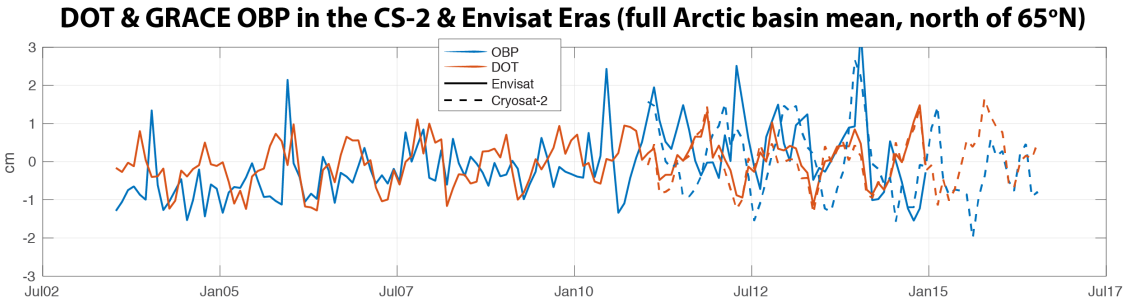

Figure A1. Timeseries of DOT (orange) and OBP (blue) averaged over all 25-km grid cells above 65°N latitude. Dotted lines indicate means over just the CryoSat-2 period, for both OBP and DOT.

However, the regional and depth-dependent variation of Arctic Ocean compels a further parsing DOT and OBP, in order to highlight the behavior of diverse marginal seas. In order to describe different bathymetric and circulation regimes across the entire Arctic basin, we make use of mooring data from three different sites. These are the Beaufort Gyre, the North Pole, and the Siberian shelves (Figure A2), from the Beaufort Gyre Exploration Project (BGEP,

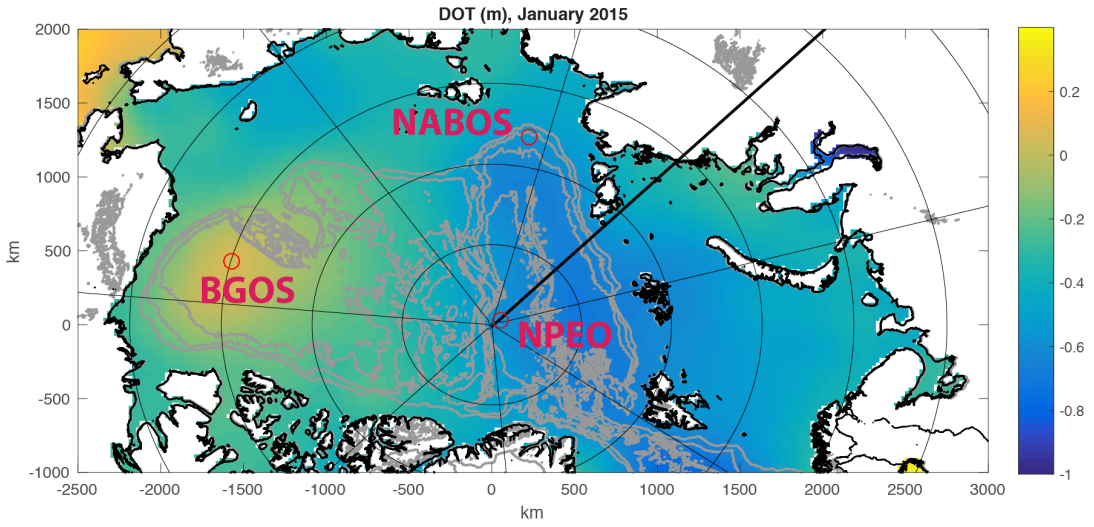

Figure A2. Map showing each of three mooring sites used for high-frequency OBP. Each of these sites lies in a different circulation regime of the Arctic Ocean: BGOS captures the Beaufort Gyre, NPEO the Transpolar Drift, and NABOS Siberian shelf circulation.

http://www.whoi.edu/beaufortgyre), the North Pole Environmental Observatory (NPEO, http://psc.apl.washington.edu/northpole), and the Nansen and Amundsen Basins Observational System (NABOS, http://nabos.iarc.uaf.edu), respectively.

Timeseries from each instrument are de-meaned and standardized, and in the case of OBP, de-tided using the Matlab routines of t_tide (Pawlowicz et al., 2002). Mooring data are lowpass filtered, and all timeseries are windowed using a full-length hanning window. The magnitude-squared coherence is then calculated with Matlab's built-in mscohere function, which uses an overlapped periodogram per Welch (1967). This coherence is a measure of how well two

variables correspond in frequency space. It is a function of the cross-spectral and autospectral densities of the variables. Higher magnitude-squared coherence indicates a stronger relationship between the inputs (Figure A3), analogous to the admittance employed by Vinogradova et al. (2007) and Bingham & Hughes (2008).

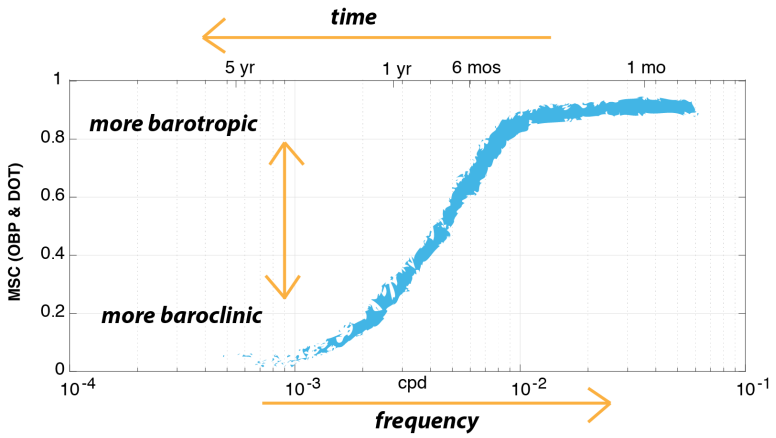

Figure A3. Schematic of magnitude squared coherence.

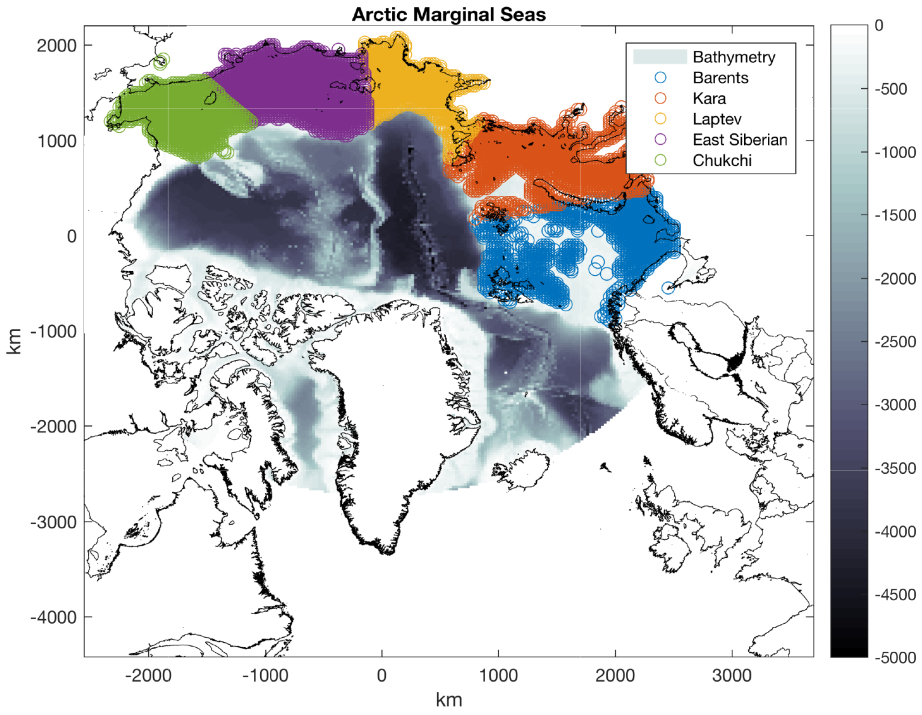

Figure A4. Map showing the division between Arctic Ocean marginal seas, with colors shown only for bathymetry less than 200 m.

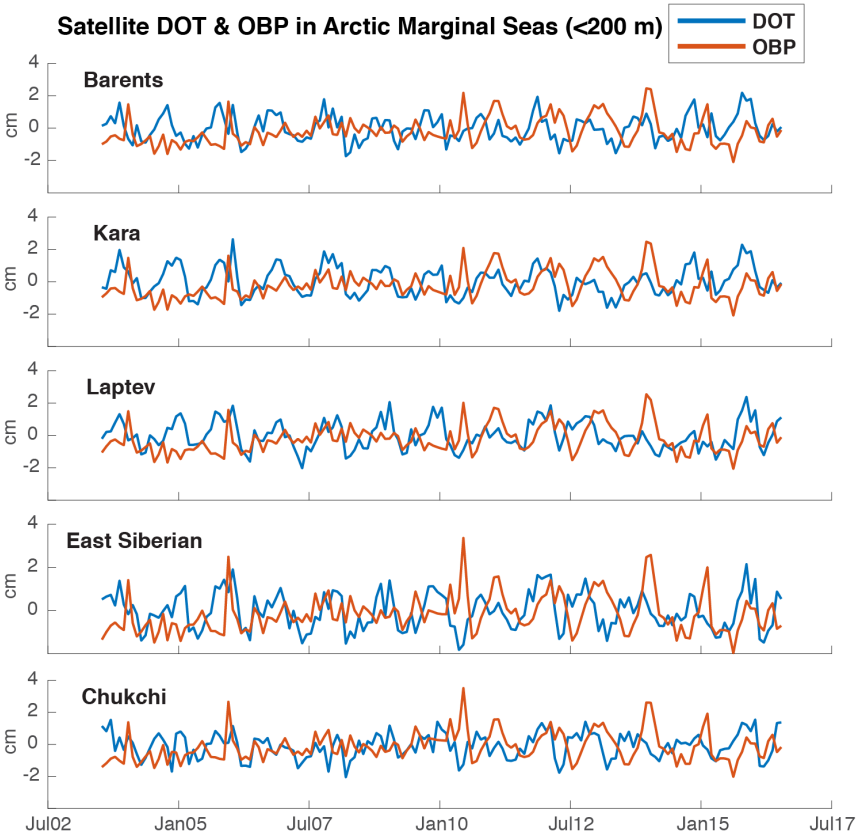

Figure A5. Timeseries of DOT and OBP in each marginal sea.

Analysis & Future Work

We analyze the coherence of two different groups of data, first with an intercomparison of the marginal seas and then looking at each mooring site to knit together high-and low-frequency data. The marginal seas are divided according to lines of longitude roughly following Alkire et al. (2017), with a bathymetric cutoff of 200 m (Figure A4) to avoid any continental slope effects. While timeseries of their DOT and OBP suggest that circulation in each sea should behave somewhat barotropically (Figure A5), they demonstrate low coherence at the upper end of the frequency spectrum resolved by satellite observations (Figure A6). Heartening, however, is the fact that the shallower seas such as the East Siberian and Chukchi, have greater coherence values than the deeper Barents and Kara seas.

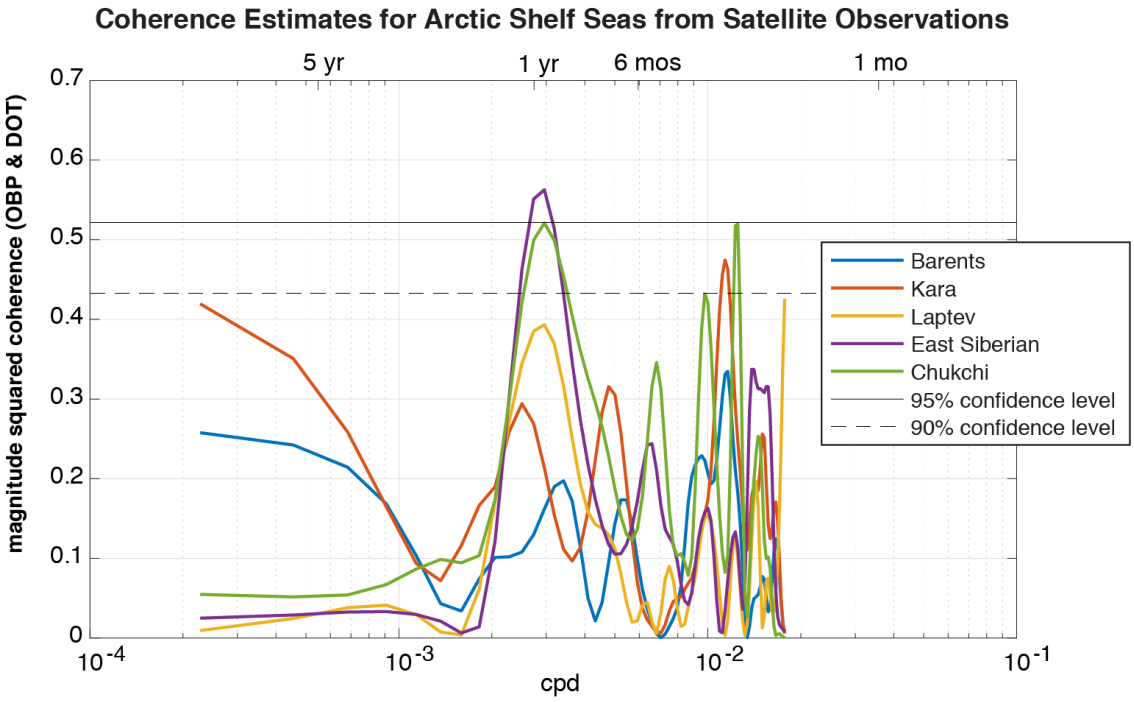

Figure A6. Satellite-based MSC estimates for each of the marginal seas in cycles per day, shown with 95% and 99% confidence limits.

For this reason, we use moored data to resolve higher frequencies, which yield higher and more significant coherence estimates as frequency increases (Figure A7); however, the observations have a high variance at this frequency and are based not on DOT, but on dynamic height calculated from mooring hydrography. Thus the challenge moving forward in this analysis will be to design a filter that captures the high-frequency signal without contamination. Past Arctic Ocean circulation modeling studies have shown high coherence, and only with better filtering of observations can we confidently identify and evaluate why and how much higher this modeled coherence is; only then can we accurately describe the movement of freshwater through the system.

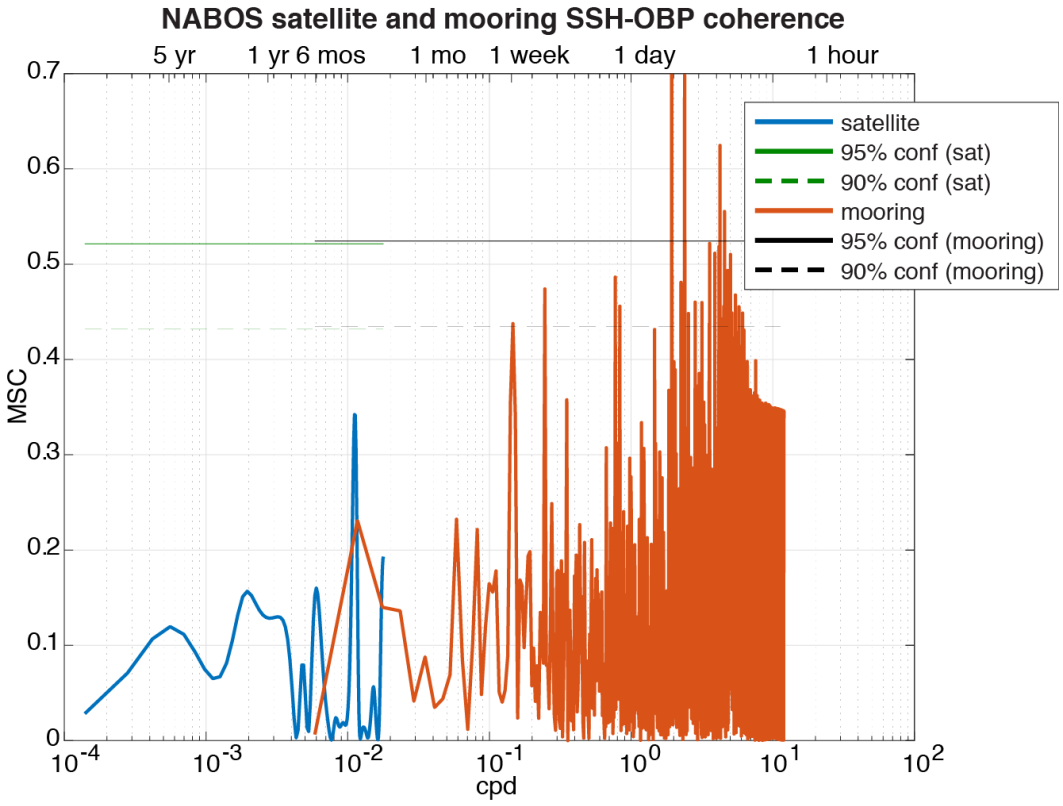

Figure A7. MSC estimates from satellite and mooring data.

Bibliography

Aagaard, K., Carmack, E.C., 1989. The role of sea ice and other fresh water in the Arctic circulation. Journal of Geophysical Research 94, 14485. https://doi.org/10.1029/JC094iC10p14485

Alkire, M.B., Morison, J., Schweiger, A., Zhang, J., Steele, M., Peralta-Ferriz, C., Dickinson, S., 2017. A Meteoric Water Budget for the Arctic Ocean: ARCTIC MW BUDGET. Journal of Geophysical Research: Oceans 122, 10020–10041. https://doi.org/10.1002/2017JC012807

Armitage, T.W.K., Bacon, S., Ridout, A.L., Petty, A.A., Wolbach, S., Tsamados, M., 2017. Arctic Ocean geostrophic circulation 2003-2014. The Cryosphere Discussions 1–32. https://doi.org/10.5194/tc-2017-22

Arntsen, A.E., Song, A.J., Perovich, D.K., Richter-Menge, J.A., 2015. Observations of the summer breakup of an Arctic sea ice cover: Summer Ice Floe Breakup. Geophysical Research Letters 42, 8057–8063. https://doi.org/10.1002/2015GL065224

Bingham, R.J., Hughes, C.W., 2008. The relationship between sea-level and bottom pressure variability in an eddy permitting ocean model. Geophysical Research Letters 35. https://doi.org/10.1029/2007GL032662

Boyer, T. P., O. K. Baranova, M. Biddle, D. R. Johnson, A. V. Mishonov, C. Paver, D. Seidov, and M.Zweng, 2012: Arctic Regional Climatology, Regional Climatology Team, NOAA/NODC. Accessed 18 November 2013. [Available online at www.nodc.noaa.gov/OC5/regional_climate/arctic.]

Carmack, E., McLaughlin, F., Yamamoto-Kawai, M., Itoh, M., Shimada, K., Krishfield, R., Proshutinsky, A., 2008. Freshwater Storage in the Northern Ocean and the Special Role of the Beaufort Gyre, in: Dickson, R.R., Meincke, J., Rhines, P. (Eds.), Arctic–Subarctic Ocean Fluxes. Springer Netherlands, Dordrecht, pp. 145–169. https://doi.org/10.1007/978-1-4020-6774-7_8

Castellani, G., Losch, M., Ungermann, M., Gerdes, R., 2018. Sea-ice drag as a function of deformation and ice cover: Effects on simulated sea ice and ocean circulation in the Arctic. Ocean Modelling 128, 48–66. https://doi.org/10.1016/j.ocemod.2018.06.002

Childers, V.A., Brozena, J.M., 2005. Long-range aircraft as an Arctic Oceanographic platform. Deep Sea Research Part I: Oceanographic Research Papers 52, 2366–2375. https://doi.org/10.1016/j.dsr.2005.07.004

Cole, S.T., Timmermans, M.-L., Toole, J.M., Krishfield, R.A., Thwaites, F.T., 2014. Ekman Veering, Internal Waves, and Turbulence Observed under Arctic Sea Ice. Journal of Physical Oceanography 44, 1306–1328. https://doi.org/10.1175/JPO-D-12-0191.1

Cole, S.T., Toole, J.M., Lele, R., Timmermans, M.-L., Gallaher, S.G., Stanton, T.P., Shaw, W.J., Hwang, B., Maksym, T., Wilkinson, J.P., Ortiz, M., Graber, H., Rainville, L., Petty, A.A., Farrell, S.L., Richter-Menge, J.A., Haas, C., Deming, J.W., Thomson, J., 2017. Ice and ocean velocity in the Arctic marginal ice zone: Ice roughness and momentum transfer. Elem Sci Anth 5. https://doi.org/10.1525/elementa.241

Comiso, J.C., Parkinson, C.L., Gersten, R., Stock, L., 2008. Accelerated decline in the Arctic sea ice cover. Geophysical Research Letters 35. https://doi.org/10.1029/2007GL031972

Dee, D.P., Uppala, S.M., Simmons, A.J., Berrisford, P., Poli, P., Kobayashi, S., Andrae, U., Balmaseda, M.A., Balsamo, G., Bauer, P., Bechtold, P., Beljaars, A.C.M., van de Berg, L., Bidlot, J., Bormann, N., Delsol, C., Dragani, R., Fuentes, M., Geer, A.J., Haimberger, L., Healy, S.B., Hersbach, H., Hólm, E.V., Isaksen, L., Kållberg, P., Köhler, M., Matricardi, M., McNally, A.P., Monge-Sanz, B.M., Morcrette, J.-J., Park, B.-K., Peubey, C., de Rosnay, P., Tavolato, C., Thépaut, J.-N., Vitart, F., 2011. The ERA-Interim reanalysis: configuration and performance of the data assimilation system. Quarterly Journal of the Royal Meteorological Society 137, 553–597. https://doi.org/10.1002/qj.828

Dewey, S., Morison, J., Kwok, R., Dickinson, S., Morison, D., Andersen, R., 2018. Arctic Ice-Ocean Coupling and Gyre Equilibration Observed With Remote Sensing. Geophysical Research Letters 45, 1499–1508. https://doi.org/10.1002/2017GL076229

Dewey, S.R., Morison, J.H., Zhang, J., 2017. An Edge-Referenced Surface Fresh Layer in the Beaufort Sea Seasonal Ice Zone. Journal of Physical Oceanography 47, 1125–1144. https://doi.org/10.1175/JPO-D-16-0158.1

Drobot, S., Stroeve, J., Maslanik, J., Emery, W., Fowler, C., Kay, J., 2008. Evolution of the 2007–2008 Arctic sea ice cover and prospects for a new record in 2008. Geophysical Research Letters 35. https://doi.org/10.1029/2008GL035316

ECMWF, I., 2018. Documentation CY45R1. *Part II: Data Assimilation, ECMWF*.

Efron, B., 1979. Bootstrap Methods: Another Look at the Jackknife. The Annals of Statistics 7, 1–26. https://doi.org/10.1214/aos/1176344552

Fer, I., Peterson, A.K., Randelhoff, A., Meyer, A., 2017. One-dimensional evolution of the upper water column in the Atlantic sector of the Arctic Ocean in winter: ARCTIC MIXED LAYER IN WINTER. Journal of Geophysical Research: Oceans 122, 1665–1682. https://doi.org/10.1002/2016JC012431

Giles, K.A., Laxon, S.W., Ridout, A.L., Wingham, D.J., Bacon, S., 2012. Western Arctic Ocean freshwater storage increased by wind-driven spin-up of the Beaufort Gyre. Nature Geoscience 5, 194–197. https://doi.org/10.1038/ngeo1379

Guthrie, J.D., Morison, J.H., Fer, I., 2013. Revisiting internal waves and mixing in the Arctic Ocean: MIXING IN THE ARCTIC OCEAN. Journal of Geophysical Research: Oceans 118, 3966–3977. https://doi.org/10.1002/jgrc.20294

Hansell, D.A., 2004. Degradation of Terrigenous Dissolved Organic Carbon in the Western Arctic Ocean. Science 304, 858–861. https://doi.org/10.1126/science.1096175

Hayes, D.R., Morison, J., 2008. Ice-ocean turbulent exchange in the Arctic summer measured by an autonomous underwater vehicle. Limnology and Oceanography 53, 2287–2308. https://doi.org/10.4319/lo.2008.53.5_part_2.2287

Hibler, W.D., 1979. A Dynamic Thermodynamic Sea Ice Model. Journal of Physical Oceanography 9, 815–846. https://doi.org/10.1175/1520-0485(1979)009<0815:ADTSIM>2.0.CO;2

Hyatt, J., 2006: Wind, sea ice, inertial oscillations and upper ocean mixing in Marguerite Bay, western Antarctic Peninsula: Observations and modeling. Ph.D. thesis, Joint Program in Oceanography/Applied Ocean Science and Engineering, Massachusetts Institute of Technology and Woods Hole Oceanographic Institution, 168 pp.

Jackson, J.M., Carmack, E.C., McLaughlin, F.A., Allen, S.E., Ingram, R.G., 2010. Identification, characterization, and change of the near-surface temperature maximum in the Canada Basin, 1993–2008. Journal of Geophysical Research 115. https://doi.org/10.1029/2009JC005265

Jahn, A., Holland, M.M., 2013. Implications of Arctic sea ice changes for North Atlantic deep convection and the meridional overturning circulation in CCSM4-CMIP5 simulations: MOC IMPACTS OF ARCTIC CHANGES. Geophysical Research Letters 40, 1206–1211. https://doi.org/10.1002/grl.50183

Jerlov, N. G., 1976: *Marine Optics*. Elsevier, 230 pp.

Johnson, G.C., Schmidtko, S., Lyman, J.M., 2012. Relative contributions of temperature and salinity to seasonal mixed layer density changes and horizontal density gradients: GLOBAL SEASONAL MIXED LAYER T AND S ROLES. Journal of Geophysical Research: Oceans 117, n/a-n/a. https://doi.org/10.1029/2011JC007651

Kaleschke, L., Lüpkes, C., Vihma, T., Haarpaintner, J., Bochert, A., Hartmann, J., Heygster, G., 2001. SSM/I Sea Ice Remote Sensing for Mesoscale Ocean-Atmosphere Interaction Analysis. Canadian Journal of Remote Sensing 27, 526–537. https://doi.org/10.1080/07038992.2001.10854892

Kalnay, E., Kanamitsu, M., Kistler, R., Collins, W., Deaven, D., Gandin, L., Iredell, M., Saha, S., White, G., Woollen, J., Zhu, Y., Leetmaa, A., Reynolds, R., Chelliah, M., Ebisuzaki, W., Higgins, W., Janowiak, J., Mo, K.C., Ropelewski, C., Wang, J., Jenne, R., Joseph, D., 1996. The NCEP/NCAR 40-Year Reanalysis Project. Bulletin of the American

Meteorological Society 77, 437–471. https://doi.org/10.1175/1520-0477(1996)077<0437:TNYRP>2.0.CO;2

Koenigk, T., Mikolajewicz, U., Haak, H., Jungclaus, J., 2007. Arctic freshwater export in the 20th and 21st centuries: ARCTIC FRESHWATER EXPORT FROM 1900 TO 2100. Journal of Geophysical Research: Biogeosciences 112, n/a-n/a. https://doi.org/10.1029/2006JG000274

Krishfield, R.A., Proshutinsky, A., Tateyama, K., Williams, W.J., Carmack, E.C., McLaughlin, F.A., Timmermans, M.-L., 2014. Deterioration of perennial sea ice in the Beaufort Gyre from 2003 to 2012 and its impact on the oceanic freshwater cycle: SEA ICE IN THE BG FROM 2003 TO 2012. Journal of Geophysical Research: Oceans 119, 1271–1305. https://doi.org/10.1002/2013JC008999

Kwok, R., 2018. Arctic sea ice thickness, volume, and multiyear ice coverage: losses and coupled variability (1958–2018). Environmental Research Letters 13, 105005. https://doi.org/10.1088/1748-9326/aae3ec

Kwok, R., Cunningham, G.F., 2015. Variability of Arctic sea ice thickness and volume from CryoSat-2. Philosophical Transactions of the Royal Society A: Mathematical, Physical and Engineering Sciences 373, 20140157. https://doi.org/10.1098/rsta.2014.0157

Kwok, R., & Morison, J. (2017). Recent changes in Arctic sea ice and ocean circulation. *US CLIVAR Variations (Summer 2017)*, **15**(3), 1–6.

Kwok, R., Morison, J., 2016. Sea surface height and dynamic topography of the ice-covered oceans from CryoSat-2: 2011–2014. Journal of Geophysical Research: Oceans 121, 674–692. https://doi.org/10.1002/2015JC011357

Kwok, R., Morison, J., 2011. Dynamic topography of the ice-covered Arctic Ocean from ICESat: DYNAMIC TOPOGRAPHY OF ARCTIC OCEAN. Geophysical Research Letters 38, n/a-n/a. https://doi.org/10.1029/2010GL046063

Kwok, R., Spreen, G., Pang, S., 2013. Arctic sea ice circulation and drift speed: Decadal trends and ocean currents: ARCTIC SEA ICE MOTION. Journal of Geophysical Research: Oceans 118, 2408–2425. https://doi.org/10.1002/jgrc.20191

Leppäranta, M., 2005. The drift of sea ice, Springer-Praxis books in geophysical sciences. Springer ; Praxis, Berlin ; New York : Chichester, UK.

Leppäranta, M., Omstedt, A., 1990. Dynamic coupling of sea ice and water for an ice field with free boundaries. Tellus A: Dynamic Meteorology and Oceanography 42, 482–495. https://doi.org/10.3402/tellusa.v42i4.11892

Lindsay, R., Schweiger, A., 2015. Arctic sea ice thickness loss determined using subsurface, aircraft, and satellite observations. The Cryosphere 9, 269–283. https://doi.org/10.5194/tc-9-269-2015

Lindsay, R., Wensnahan, M., Schweiger, A., Zhang, J., 2014. Evaluation of Seven Different Atmospheric Reanalysis Products in the Arctic*. Journal of Climate 27, 2588–2606. https://doi.org/10.1175/JCLI-D-13-00014.1

Liu, Z., Schweiger, A., Lindsay, R., 2015. Observations and Modeling of Atmospheric Profiles in the Arctic Seasonal Ice Zone. Monthly Weather Review 143, 39–53. https://doi.org/10.1175/MWR-D-14-00118.1

Lu, P., Li, Z., Cheng, B., Leppäranta, M., 2011. A parameterization of the ice-ocean drag coefficient. Journal of Geophysical Research 116. https://doi.org/10.1029/2010JC006878

M. Tschudi/Univ Of CO, 2016. Polar Pathfinder Daily 25 km EASE-Grid Sea Ice Motion Vectors, Version 3. https://doi.org/10.5067/O57VAIT2AYYY

Ma, B., Steele, M., Lee, C.M., 2017. Ekman circulation in the Arctic Ocean: Beyond the Beaufort Gyre: EKMAN CIRCULATION IN THE ARCTIC OCEAN. Journal of Geophysical Research: Oceans 122, 3358–3374. https://doi.org/10.1002/2016JC012624

Manucharyan, G.E., Spall, M.A., 2016. Wind-driven freshwater buildup and release in the Beaufort Gyre constrained by mesoscale eddies: EDDY CONSTRAINED BEAUFORT GYRE. Geophysical Research Letters 43, 273–282. https://doi.org/10.1002/2015GL065957

Manucharyan, G.E., Spall, M.A., Thompson, A.F., 2016. A Theory of the Wind-Driven Beaufort Gyre Variability. Journal of Physical Oceanography 46, 3263–3278. https://doi.org/10.1175/JPO-D-16-0091.1

Martin, T., Steele, M., Zhang, J., 2014. Seasonality and long-term trend of Arctic Ocean surface stress in a model. Journal of Geophysical Research: Oceans 119, 1723–1738. https://doi.org/10.1002/2013JC009425

Martin, T., Tsamados, M., Schroeder, D., Feltham, D.L., 2016. The impact of variable sea ice roughness on changes in Arctic Ocean surface stress: A model study: ARCTIC OCEAN SURFACE STRESS. Journal of Geophysical Research: Oceans 121, 1931–1952. https://doi.org/10.1002/2015JC011186

Maslanik, J., Stroeve, J., Fowler, C., Emery, W., 2011. Distribution and trends in Arctic sea ice age through spring 2011: TRENDS IN ARCTIC SEA ICE AGE. Geophysical Research Letters 38, n/a-n/a. https://doi.org/10.1029/2011GL047735

Maykut, G.A., McPhee, M.G., 1995. Solar heating of the Arctic mixed layer. Journal of Geophysical Research 100, 24691. https://doi.org/10.1029/95JC02554

McAdoo, D.C., Farrell, S.L., Laxon, S., Ridout, A., Zwally, H.J., Yi, D., 2013. Gravity of the Arctic Ocean from satellite data with validations using airborne gravimetry: Oceanographic implications: ARCTIC OCEAN GRAVITY FROM SATELLITE DATA. Journal of Geophysical Research: Oceans 118, 917–930. https://doi.org/10.1002/jgrc.20080

McPhee, M., 2008. Air-Ice-Ocean Interaction. Springer New York, New York, NY. https://doi.org/10.1007/978-0-387-78335-2

McPhee, M.G., 2013. Intensification of Geostrophic Currents in the Canada Basin, Arctic Ocean. Journal of Climate 26, 3130–3138. https://doi.org/10.1175/JCLI-D-12-00289.1

McPhee, M.G., 2012. Advances in understanding ice–ocean stress during and since AIDJEX. Cold Regions Science and Technology 76–77, 24–36. https://doi.org/10.1016/j.coldregions.2011.05.001

McPhee, M.G., Proshutinsky, A., Morison, J.H., Steele, M., Alkire, M.B., 2009. Rapid change in freshwater content of the Arctic Ocean. Geophysical Research Letters 36. https://doi.org/10.1029/2009GL037525

McPhee, M. G. (1982). Sea ice drag laws and simple boundary layer concepts, including application to rapid melting.

McPhee, M. G. (1980). An analysis of pack ice drift in summer. In R. Pritchard (Ed.), *Sea ice processes and models* (pp. 62–75). Seattle: University of Washington Press.

McPhee, M.G., 1979. The Effect of the Oceanic Boundary Layer on the Mean Drift of Pack Ice: Application of a Simple Model. Journal of Physical Oceanography 9, 388–400. https://doi.org/10.1175/1520-0485(1979)009<0388:TEOTOB>2.0.CO;2

Meneghello, G., Marshall, J., Cole, S.T., Timmermans, M.-L., 2017. Observational Inferences of Lateral Eddy Diffusivity in the Halocline of the Beaufort Gyre: EDDY DIFFUSIVITY IN THE BEAUFORT GYRE. Geophysical Research Letters 44, 12,331-12,338. https://doi.org/10.1002/2017GL075126

Meneghello, G., Marshall, J., Timmermans, M.-L., Scott, J., 2018. Observations of Seasonal Upwelling and Downwelling in the Beaufort Sea Mediated by Sea Ice. Journal of Physical Oceanography 48, 795–805. https://doi.org/10.1175/JPO-D-17-0188.1

Morison, J., Kwok, R., Peralta-Ferriz, C., Alkire, M., Rigor, I., Andersen, R., Steele, M., 2012. Changing Arctic Ocean freshwater pathways. Nature 481, 66–70. https://doi.org/10.1038/nature10705

Nansen, F. (1902). The oceanography of the North Polar Basin, *Rep*., 1–427 pp.

Nguyen, A.T., Menemenlis, D., Kwok, R., 2009. Improved modeling of the Arctic halocline with a subgrid-scale brine rejection parameterization. Journal of Geophysical Research 114. https://doi.org/10.1029/2008JC005121

Ogi, M., Wallace, J.M., 2007. Summer minimum Arctic sea ice extent and the associated summer atmospheric circulation. Geophysical Research Letters 34. https://doi.org/10.1029/2007GL029897

Parkinson, C.L., Comiso, J.C., 2013. On the 2012 record low Arctic sea ice cover: Combined impact of preconditioning and an August storm: 2012 RECORD LOW ARCTIC SEA ICE COVER. Geophysical Research Letters 40, 1356–1361. https://doi.org/10.1002/grl.50349

Pavlis, N., Kenyon, S., Factor, J., Holmes, S., 2008. Earth gravitational model 2008, in: SEG Technical Program Expanded Abstracts 2008. Presented at the SEG Technical Program Expanded Abstracts 2008, Society of Exploration Geophysicists, pp. 761–763. https://doi.org/10.1190/1.3063757

Pawlowicz, R., Beardsley, B., Lentz, S., 2002. Classical tidal harmonic analysis including error estimates in MATLAB using T_TIDE. Computers & Geosciences 28, 929–937. https://doi.org/10.1016/S0098-3004(02)00013-4

Peng, G., Meier, W.N., 2018. Temporal and regional variability of Arctic sea-ice coverage from satellite data. Annals of Glaciology 59, 191–200. https://doi.org/10.1017/aog.2017.32

Peralta-Ferriz, C., Morison, J.H., Wallace, J.M., Bonin, J.A., Zhang, J., 2014. Arctic Ocean Circulation Patterns Revealed by GRACE. Journal of Climate 27, 1445–1468. https://doi.org/10.1175/JCLI-D-13-00013.1

Peralta-Ferriz, C., Morison, J.H., Wallace, J.M., Zhang, J., 2011. A basin-coherent mode of sub-monthly variability in Arctic Ocean bottom pressure: SUB-MONTHLY ARCTIC OCEAN MODE. Geophysical Research Letters 38, n/a-n/a. https://doi.org/10.1029/2011GL048142

Peralta-Ferriz, C., Woodgate, R.A., 2015. Seasonal and interannual variability of pan-Arctic surface mixed layer properties from 1979 to 2012 from hydrographic data, and the dominance of stratification for multiyear mixed layer depth shoaling. Progress in Oceanography 134, 19–53. https://doi.org/10.1016/j.pocean.2014.12.005

Perovich, D.K., Richter-Menge, J.A., Jones, K.F., Light, B., Elder, B.C., Polashenski, C., Laroche, D., Markus, T., Lindsay, R., 2011. Arctic sea-ice melt in 2008 and the role of solar heating. Annals of Glaciology 52, 355–359. https://doi.org/10.3189/172756411795931714

Petty, A.A., Hutchings, J.K., Richter-Menge, J.A., Tschudi, M.A., 2016. Sea ice circulation around the Beaufort Gyre: The changing role of wind forcing and the sea ice state. Journal of Geophysical Research: Oceans 121, 3278–3296. https://doi.org/10.1002/2015JC010903

Petty, A.A., Tsamados, M.C., Kurtz, N.T., 2017. Atmospheric form drag coefficients over Arctic sea ice using remotely sensed ice topography data, spring 2009-2015: ATMOSPHERIC DRAG OVER ARCTIC SEA ICE. Journal of Geophysical Research: Earth Surface 122, 1472–1490. https://doi.org/10.1002/2017JF004209

Polar Science Center, University of Washington Applied Physics Lab (2018). International Arctic Buoy Programme, IABP dataset D. Retrieved from http://iabp.apl.washington.edu/data.html, accessed online 21 June 2019.

Price, J.F., Weller, R.A., Pinkel, R., 1986. Diurnal cycling: Observations and models of the upper ocean response to diurnal heating, cooling, and wind mixing. Journal of Geophysical Research 91, 8411. https://doi.org/10.1029/JC091iC07p08411

Proshutinsky, A., Bourke, R.H., McLaughlin, F.A., 2002. The role of the Beaufort Gyre in Arctic climate variability: Seasonal to decadal climate scales: BEAUFORT GYRE. Geophysical Research Letters 29, 15-1-15–4. https://doi.org/10.1029/2002GL015847

Proshutinsky, A., Krishfield, R., Timmermans, M.-L., Toole, J., Carmack, E., McLaughlin, F., Williams, W.J., Zimmermann, S., Itoh, M., Shimada, K., 2009. Beaufort Gyre freshwater reservoir: State and variability from observations. Journal of Geophysical Research 114. https://doi.org/10.1029/2008JC005104

Proshutinsky, A.Y., Johnson, M.A., 1997. Two circulation regimes of the wind-driven Arctic Ocean. Journal of Geophysical Research: Oceans 102, 12493–12514. https://doi.org/10.1029/97JC00738

Rabe, B., Karcher, M., Kauker, F., Schauer, U., Toole, J.M., Krishfield, R.A., Pisarev, S., Kikuchi, T., Su, J., 2014. Arctic Ocean basin liquid freshwater storage trend 1992-2012. Geophysical Research Letters 41, 961–968. https://doi.org/10.1002/2013GL058121

Rabe, B., Karcher, M., Schauer, U., Toole, J.M., Krishfield, R.A., Pisarev, S., Kauker, F., Gerdes, R., Kikuchi, T., 2011. An assessment of Arctic Ocean freshwater content changes from the 1990s to the 2006–2008 period. Deep Sea Research Part I: Oceanographic Research Papers 58, 173–185. https://doi.org/10.1016/j.dsr.2010.12.002

Rampal, P., Weiss, J., Marsan, D., 2009. Positive trend in the mean speed and deformation rate of Arctic sea ice, 1979–2007. Journal of Geophysical Research 114. https://doi.org/10.1029/2008JC005066

Randelhoff, A., Sundfjord, A., Renner, A.H.H., 2014. Effects of a Shallow Pycnocline and Surface Meltwater on Sea Ice–Ocean Drag and Turbulent Heat Flux. Journal of Physical Oceanography 44, 2176–2190. https://doi.org/10.1175/JPO-D-13-0231.1

Richter-Menge, J.A., Elder, B., Claffey, K., Overland, J. and Salo, S., 2002a, December. In situ sea ice stresses in the western Arctic during the winter of 2001–2002. In *Proceedings of the*

16th IAHR International Symposium on Ice (Vol. 2, pp. 423-430). Dunedin, New Zealand: Univ. of Otago.

Rigor, I.G., Wallace, J.M., Colony, R.L., 2002. Response of Sea Ice to the Arctic Oscillation. Journal of Climate 15, 2648–2663. https://doi.org/10.1175/1520-0442(2002)015<2648:ROSITT>2.0.CO;2

Rosel, A., Kaleschke, L., 2012. Influence of melt ponds on microwave sensors' sea ice concentration retrieval algorithms, in: 2012 IEEE International Geoscience and Remote Sensing Symposium. Presented at the IGARSS 2012 - 2012 IEEE International Geoscience and Remote Sensing Symposium, IEEE, Munich, Germany, pp. 3261–3264. https://doi.org/10.1109/IGARSS.2012.6350608

Roy, F., Chevallier, M., Smith, G.C., Dupont, F., Garric, G., Lemieux, J.-F., Lu, Y., Davidson, F., 2015. Arctic sea ice and freshwater sensitivity to the treatment of the atmosphere-ice-ocean surface layer: THE ARCTIC AIR-ICE-OCEAN SURFACE LAYER. Journal of Geophysical Research: Oceans 120, 4392–4417. https://doi.org/10.1002/2014JC010677

Schwegmann, S., Haas, C., Fowler, C., Gerdes, R., 2011. A comparison of satellite-derived sea-ice motion with drifting-buoy data in the Weddell Sea, Antarctica. Annals of Glaciology 52, 103–110. https://doi.org/10.3189/172756411795931813

Schweiger, A., Lindsay, R., Zhang, J., Steele, M., Stern, H., Kwok, R., 2011. Uncertainty in modeled Arctic sea ice volume. Journal of Geophysical Research 116. https://doi.org/10.1029/2011JC007084

Seidov, D., Antonov, J.I., Arzayus, K.M., Baranova, O.K., Biddle, M., Boyer, T.P., Johnson, D.R., Mishonov, A.V., Paver, C., Zweng, M.M., 2015. Oceanography north of 60°N from World Ocean Database. Progress in Oceanography 132, 153–173. https://doi.org/10.1016/j.pocean.2014.02.003

Serreze, M.C., Barrett, A.P., Slater, A.G., Woodgate, R.A., Aagaard, K., Lammers, R.B., Steele, M., Moritz, R., Meredith, M., Lee, C.M., 2006. The large-scale freshwater cycle of the Arctic. Journal of Geophysical Research 111. https://doi.org/10.1029/2005JC003424

Sévellec, F., Fedorov, A.V., Liu, W., 2017. Arctic sea-ice decline weakens the Atlantic Meridional Overturning Circulation. Nature Climate Change 7, 604–610. https://doi.org/10.1038/nclimate3353

Shaw, W.J., Stanton, T.P., McPhee, M.G., Kikuchi, T., 2008. Estimates of surface roughness length in heterogeneous under-ice boundary layers. Journal of Geophysical Research 113. https://doi.org/10.1029/2007JC004550

Shimada, K., Kamoshida, T., Itoh, M., Nishino, S., Carmack, E., McLaughlin, F., Zimmermann, S., Proshutinsky, A., 2006. Pacific Ocean inflow: Influence on catastrophic reduction of sea

ice cover in the Arctic Ocean. Geophysical Research Letters 33. https://doi.org/10.1029/2005GL025624

Spreen, G., Kwok, R., Menemenlis, D., 2011. Trends in Arctic sea ice drift and role of wind forcing: 1992-2009: TRENDS IN ARCTIC SEA ICE DRIFT AND WIND. Geophysical Research Letters 38, n/a-n/a. https://doi.org/10.1029/2011GL048970

Steele, M., Ermold, W., 2015. Loitering of the retreating sea ice edge in the Arctic Seas: LOITERING OF THE RETREATING SEA ICE EDGE. Journal of Geophysical Research: Oceans 120, 7699–7721. https://doi.org/10.1002/2015JC011182

Steele, M., Morison, J.H., Untersteiner, N., 1989. The partition of air-ice-ocean momentum exchange as a function of ice concentration, floe size, and draft. Journal of Geophysical Research 94, 12739. https://doi.org/10.1029/JC094iC09p12739

Steele, M., 2004. Circulation of summer Pacific halocline water in the Arctic Ocean. Journal of Geophysical Research 109. https://doi.org/10.1029/2003JC002009

Steele, M., Ermold, W., Zhang, J., 2011. Modeling the formation and fate of the near-surface temperature maximum in the Canadian Basin of the Arctic Ocean. Journal of Geophysical Research 116. https://doi.org/10.1029/2010JC006803

Steele, M., Morley, R., Ermold, W., 2001. PHC: A Global Ocean Hydrography with a High-Quality Arctic Ocean. Journal of Climate 14, 2079–2087. https://doi.org/10.1175/1520-0442(2001)014<2079:PAGOHW>2.0.CO;2

Steele, M., Zhang, J., Ermold, W., 2010. Mechanisms of summertime upper Arctic Ocean warming and the effect on sea ice melt. Journal of Geophysical Research 115. https://doi.org/10.1029/2009JC005849

Stern, H.L., Schweiger, A.J., Stark, M., Zhang, J., Steele, M., Hwang, B., 2018. Seasonal evolution of the sea-ice floe size distribution in the Beaufort and Chukchi seas. Elem Sci Anth 6, 48. https://doi.org/10.1525/elementa.305

Strong, C., Rigor, I.G., 2013. Arctic marginal ice zone trending wider in summer and narrower in winter: MARGINAL ICE ZONE TRENDS. Geophysical Research Letters 40, 4864–4868. https://doi.org/10.1002/grl.50928

Sumata, H., Kwok, R., Gerdes, R., Kauker, F., Karcher, M., 2015. Uncertainty of Arctic summer ice drift assessed by high-resolution SAR data: UNCERTAINTY OF ARCTIC SUMMER ICE DRIFT. Journal of Geophysical Research: Oceans 120, 5285–5301. https://doi.org/10.1002/2015JC010810

Sumata, H., Lavergne, T., Girard-Ardhuin, F., Kimura, N., Tschudi, M.A., Kauker, F., Karcher, M., Gerdes, R., 2014. An intercomparison of Arctic ice drift products to deduce uncertainty

estimates. Journal of Geophysical Research: Oceans 119, 4887–4921. https://doi.org/10.1002/2013JC009724

Szanyi, S., Lukovich, J.V., Barber, D.G., Haller, G., 2016. Persistent artifacts in the NSIDC ice motion data set and their implications for analysis: PERSISTENT ARTIFACTS IN NSIDC ICE DRIFT. Geophysical Research Letters 43, 10,800-10,807. https://doi.org/10.1002/2016GL069799

Thompson, D.W.J., Wallace, J.M., 1998. The Arctic oscillation signature in the wintertime geopotential height and temperature fields. Geophysical Research Letters 25, 1297–1300. https://doi.org/10.1029/98GL00950

Thorndike, A.S., Colony, R., 1982. Sea ice motion in response to geostrophic winds. Journal of Geophysical Research 87, 5845. https://doi.org/10.1029/JC087iC08p05845

Timmermans, M.-L., Proshutinsky, A., Golubeva, E., Jackson, J.M., Krishfield, R., McCall, M., Platov, G., Toole, J., Williams, W., Kikuchi, T., Nishino, S., 2014. Mechanisms of Pacific Summer Water variability in the Arctic's Central Canada Basin. Journal of Geophysical Research: Oceans 119, 7523–7548. https://doi.org/10.1002/2014JC010273

Timokhov, L., and F. Tanis, Eds., 1997: Environmental Working Group Joint U.S.-Russian Atlas of the Arctic Ocean, version 1. National Snow and Ice Data Center, CD-ROM, doi:https://doi.org/10.7265/N5H12ZX4.

Toole, J.M., Timmermans, M.-L., Perovich, D.K., Krishfield, R.A., Proshutinsky, A., Richter-Menge, J.A., 2010. Influences of the ocean surface mixed layer and thermohaline stratification on Arctic Sea ice in the central Canada Basin. Journal of Geophysical Research 115. https://doi.org/10.1029/2009JC005660

Tsamados, M., Feltham, D.L., Schroeder, D., Flocco, D., Farrell, S.L., Kurtz, N., Laxon, S.W., Bacon, S., 2014. Impact of Variable Atmospheric and Oceanic Form Drag on Simulations of Arctic Sea Ice*. Journal of Physical Oceanography 44, 1329–1353. https://doi.org/10.1175/JPO-D-13-0215.1

Untersteiner, N., 1988. On the ice and heat balance in Fram Strait. Journal of Geophysical Research 93, 527. https://doi.org/10.1029/JC093iC01p00527

Vinogradova, N.T., Ponte, R.M., Stammer, D., 2007. Relation between sea level and bottom pressure and the vertical dependence of oceanic variability. Geophysical Research Letters 34. https://doi.org/10.1029/2006GL028588

Welch, P., 1967. The use of fast Fourier transform for the estimation of power spectra: A method based on time averaging over short, modified periodograms. IEEE Transactions on Audio and Electroacoustics 15, 70–73. https://doi.org/10.1109/TAU.1967.1161901

Woodgate, R.A., Aagaard, K., Weingartner, T.J., 2006. Interannual changes in the Bering Strait fluxes of volume, heat and freshwater between 1991 and 2004. Geophysical Research Letters 33. https://doi.org/10.1029/2006GL026931

Woods Hole Oceanographic Institution(2017). Beaufort Gyre exploration project: BG freshwater content (FWC) reaches absolute maximum in 2015. Retrieved from http://www.whoi.edu/page.do?pid=153276, accessed online 10 October 2017

Woods Hole Oceanographic Institution (2010). Arctic Ocean Model Intercomparison Project: Ocean-Ice Exchange. Retrieved from https://www.whoi.edu/page.do?pid=40751, accessed online 21 June 2019.

Yang, J., 2009. Seasonal and interannual variability of downwelling in the Beaufort Sea. Journal of Geophysical Research 114. https://doi.org/10.1029/2008JC005084

Zhang, J., Schweiger, A., Steele, M., Stern, H., 2015. Sea ice floe size distribution in the marginal ice zone: Theory and numerical experiments: Modeling floe size distribution. Journal of Geophysical Research: Oceans 120, 3484–3498. https://doi.org/10.1002/2015JC010770

Zhang, J., Steele, M., Runciman, K., Dewey, S., Morison, J., Lee, C., Rainville, L., Cole, S., Krishfield, R., Timmermans, M.-L., Toole, J., 2016a. The Beaufort Gyre intensification and stabilization: A model-observation synthesis: BEAUFORT GYRE STABILIZATION. Journal of Geophysical Research: Oceans 121, 7933–7952. https://doi.org/10.1002/2016JC012196

Zhang, J., Stern, H., Hwang, B., Schweiger, A., Steele, M., Stark, M., Graber, H.C., 2016b. Modeling the seasonal evolution of the Arctic sea ice floe size distribution. Elementa: Science of the Anthropocene 4, 000126. https://doi.org/10.12952/journal.elementa.000126

Zhang, J., Lindsay, R., Schweiger, A., Rigor, I., 2012. Recent changes in the dynamic properties of declining Arctic sea ice: A model study. Geophysical Research Letters 39. https://doi.org/10.1029/2012GL053545

Zhang, J., Lindsay, R., Steele, M., Schweiger, A., 2008a. What drove the dramatic retreat of arctic sea ice during summer 2007? Geophysical Research Letters 35. https://doi.org/10.1029/2008GL034005

Zhang, J., Steele, M., Lindsay, R., Schweiger, A., Morison, J., 2008b. Ensemble 1-Year predictions of Arctic sea ice for the spring and summer of 2008. Geophysical Research Letters 35. https://doi.org/10.1029/2008GL033244

Zhang, J., Hibler, W.D., 1997. On an efficient numerical method for modeling sea ice dynamics. Journal of Geophysical Research: Oceans 102, 8691–8702. https://doi.org/10.1029/96JC03744

Zhong, W., Steele, M., Zhang, J., Zhao, J., 2018. Greater Role of Geostrophic Currents in Ekman Dynamics in the Western Arctic Ocean as a Mechanism for Beaufort Gyre Stabilization: EKMAN DYNAMICS IN WESTERN ARCTIC OCEAN. Journal of Geophysical Research: Oceans 123, 149–165. https://doi.org/10.1002/2017JC013282